

This dissertation aims to ascertain how electronic structure of rutile and anatase TiO_2 , which is considered the model system in transition metal oxides, changes when the material contains even subtle amount of dopants (H, Fe and Cd) and point defects. Consequently, the $^{111\text{m}}\text{Cd}/\text{Cd}$ time-differential γ - γ perturbed angular correlation technique, along with Mössbauer spectroscopy and tracer diffusion studies have been applied and mostly complemented with the theoretical studies and standard techniques. Furthermore, the author presents a newly developed emission Mössbauer set-up (eMIL), which has been developed and constructed during the current study.

DEFECT COMPLEXES INTERPLAY AND ITS INFLUENCE ON THE HYPERFINE STRUCTURE OF HYDROGENATED TiO_2

Von:

Dmitry V. Zyabkin

Ilmenau

2020



Technische Universität Ilmenau,
Werkstoffe der Elektrotechnik
Fakultät für Elektrotechnik und Informationstechnik

Dissertation
zur Erlangung des akademischen Grades
Doktoringenieur
(Dr.-Ing.)

Defect Complexes Interplay and its Influence on the Hyperfine Structure of Hydrogenated TiO_2

Von:
Dmitry V. Zyabkin
geboren am 7.06.1990
in Belgorod, Russland

Ilmenau 2020

DIE GUTACHTER:

- 1.Gutachter: Prof. Peter Schaaf (TU Ilmenau)
- 2.Gutachter: Prof. Stefan Krischok (TU Ilmenau)
- 3.Gutachter: Prof. Miroslav Mašláň (Palacký University)

TAG DER EINREICHUNG

7.April 2020

TAG DER WISSENSCHAFTLICHEN AUSSPRACHE

30.Juli 2020

Abstract

Determination of factors, that govern the kinetics of photocatalytic processes and the knowledge of their roles in transition metal oxides is a critical component to consider when devising efficient materials. Previous studies have shown that point defects, such as substitutional atoms, interstitials and vacancies account remarkably for the electronic structure and chemical properties, that influence the performance of these material in various applications. The expectation that a fundamental understanding of such defects will benefit to elucidate the influence that they have on the system's functionality is the driving force for pursuing experimental and theoretical research on doped and reduced materials. This dissertation aims to ascertain how electronic structure of rutile and anatase TiO_2 , which is considered *the* model system in transition metal oxides, changes when the material contains even subtle amount of dopants (H, Fe and Cd) and point defects. Consequently, time-differential $\gamma - \gamma$ perturbed angular correlation technique, along with Mössbauer spectroscopy and tracer diffusion studies have been applied and mostly complemented with theoretical studies and standard techniques. Furthermore, the author presents a newly developed emission Mössbauer set-up (eMIL), which has been developed and constructed during the current study.

Obtained results demonstrate that dopant behaviour is not straight-forward. In monocrystalline rutile, Cd resides not only at the cationic site, but also at impurity-vacancy configurations near the probe. The probe in both environments seem to withstand high temperature annealing/measurements, although associated with alterations in fractions ratio. During emission Mössbauer studies, thin films of anatase show the temperature dependent behaviour throughout the whole temperature range. This results in two annealing stages caused by the vacancy movements and their interaction with Ti interstitials. Substitutional Fe^{3+} , at Ti sites showing spin-lattice relaxation transforms upon hydrogenation, implying that hydrogen behaves as a shallow donor. eMS experiments performed in a temperature range of 300 - 700 K reveal that vacancies and their agglomerations may govern the hydrogen motion. Further perturbed angular correlation studies at the temperature when the hydrogen motion starts, show that depending on the hydrogenation degree the dopant (hydrogen) acts differently and could form a unique coupling with Cd. Hydrogenation for prolonged times demonstrates that doping/reduction is followed by the recovery processes.

The current work clearly indicates that experimental techniques based on hyperfine interactions can unravel a wealth of information about the nature and behaviour of defects in transition metal oxides, that may be readily evaluated and complemented with detailed density functional theory calculations.

Kurzfassung

Die Bestimmung von Faktoren, welche die Kinetik von photokatalytischen Prozessen beeinflussen und das Nachvollziehen von deren Funktion in Übergangsmetalloxiden, ist das Hauptthema beim Design von effizienten Materialien. Vorhergehende Studien haben gezeigt, dass Punktdefekte wie zum Beispiel Substitutionsatome, Zwischengitteratome und Leerstellen einen wesentlichen Beitrag zur Bandstruktur und zu den chemischen Eigenschaften eines Materials beitragen. Die Veränderung dieser Eigenschaften beeinflusst die Performance von Materialien in gewissen Anwendungsbereichen stark. Die Erwartung, dass ein fundamentales Verständnis von solchen Gitterdefekten positiv zur Aufklärung von deren Wirkung auf die Eigenschaften eines Materials beiträgt, ist die treibende Kraft hinter theoretischer und praktischer Forschung an dotierten und reduzierten Materialien. Das Ziel dieser Dissertation ist die Veränderung der elektronischen Struktur von Rutil und Anatas TiO_2 , welche die Modellsysteme von Übergangsmetalloxiden darstellen, unter der Beeinflussung von niedrigen Dotierungen mit Wasserstoff, Eisen und Cadmium sowie den Einfluss von Punktdefekten, zu untersuchen. Hierfür wurden Untersuchungen mit der Gestörte $\gamma - \gamma$ -Winkelkorrelation (englisch: time-differential perturbed angular correlation oder PAC) Methode, gemeinsam mit Mössbauer Spektroskopie und Tracer Diffusionsexperimenten durchgeführt, welche durch theoretische Studien und Untersuchungen mit Standardmethoden ergänzt wurden. Des weiteren präsentiert der Autor einen neuen Versuchsaufbau zur Durchführung von Emissions-Mössbauer Messungen (eMIL), welches während dieser Arbeit entwickelt und konstruiert wurde.

Die beobachteten Ergebnisse zeigen, dass das Dotandenverhalten nicht leicht voraussehbar ist und das Cd als Dotand in monokristallinem Rutil nicht nur am Kationenplatz sitzt, sondern dass Anteile davon auch andere Umgebungen, die von Leerstellenkonfigurationen beeinflusst werden, besetzen. Beide entdeckten Probenumgebungen scheinen hohen Temperaturen zu widerstehen, allerdings sind Änderungen im Anteilverhalten sichtbar. Bei Emissions-Mössbauer Messungen zeigen dünne Schichten von Anastase ein temperaturabhängiges Verhalten im gesamten Messbereich. Dies hat zur Folge, dass zwei Anlass Stufen entstehen, welche durch Leerstellenbewegung und deren Interaktion mit Ti Zwischengitteratomen hervorgerufen werden. Die Oxidationsstufe Fe^{3+} , welche eine Spin-Gitter-Relaxation zeigt, ändert sich durch Hydrierung. Dies impliziert, dass Wasserstoff ein sogenannter flacher Donator ist. Experimente in einem bestimmten Temperaturbereich zeigen, dass Leerstellen und Leerstellenansammlungen die Wasserstoffbewegung beeinflussen. Weitere PAC Experimente an den Temperaturwerten, an denen die Wasserstoffbewegung startet, zeigen eine Abhängigkeit des Verhaltens des Dotanden (Wasserstoff), zum Beispiel eine Kopplung mit Cd, von der Hydrierungsstärke. Längere Hydrierungsdauern zeigen, dass nach Dotierung bzw. Reduktionsprozessen Erholungseffekte folgen können.

Die vorliegende Arbeit zeigt deutlich, dass die Methoden der Hyperfeinwechselwirkungen Informationen über die Natur und das Verhalten von Defekten in Übergangsmetalloxiden bereitstellen können. Diese Ergebnisse können einfach evaluiert und mit detaillierten Dichtefunktionaltheoriesimulationen verglichen werden.

Acknowledgements

Over the course of my PhD years, I had a great opportunity of being involved into research activities with different people, in different countries and under different conditions. In all those situations I have been surrounded by true professionals who helped me one way or another in the progress of my work and to whom I will always save room in my heart. Alas, I can only name several (honestly, there is just too many to name), therefore a tremendous "thank you" to all those who know who they are. First of all, I would like to thank the organisations involved in my work, because without them, among other things I would not have a place to indulge and perform my research: Technical University of Ilmenau (TU Ilmenau) and the European Organization for Nuclear Research (CERN). Second of all, I am sincerely grateful to numerous people who have assisted me over the course of last years, for whom I want to leave a personal word of acknowledgement:

I am sincerely grateful and always indebted to my supervisor, Peter Schaaf, who welcomed me in his group, believed in me and provided me with the scientific liberty.

To Ulrich Vetter, for the opportunity to work and learn countless important things; for the opportunity to design and build exotic equipment, for supporting and cheering me up during not so easy times and my first beam time.

To Juliana Schell, who has always been helping me in countless ways, supporting my opportunistic and adventurous ideas and the constant enlivening. I will be always indebted.

To people I had honour to meet during the beam-times, from both PAC and eMS collaborations. Those days (or rather nights) of shifts, brought me plenty of emotions, useful knowledge and results. I am deeply grateful to J. G. M. Correia, who has helped me on numerous occasions and for very fruitful and useful discussions we held about physics, engineering, PAC, FFT and life in general. Besides, I would like to thank H.P. Gunnlaugsson and all the other great people involved in ISOLDE/CERN collaborations.

Additionally, I want to express my gratitude to several members of FG WET, who showed to be good co-workers but above all some of them turned out to be true friends. Andreas Herz, Manuel Oliva and Hongmei Wang I am going to miss the table tennis tournaments we held. Additional commendation belongs to Sergii Skoblikov, who was a whole workshop for me.

Ultimately, I thank my kith and kin and especially my parents, for their unwavering support throughout my scientific career, particularly when I was burning the candle at both ends.

Eidesstattliche Versicherung

Hiermit versichere ich an Eides statt, dass ich die vorliegende Arbeit selbstständig und ohne fremde Hilfe angefertigt und mich anderer als der im beigefügten Verzeichnis angegebenen Hilfsmittel nicht bedient habe. Alle Stellen, die wörtlich oder sinngemäß aus Veröffentlichungen entnommen wurden, sind als solche kenntlich gemacht. Ich versichere weiterhin, dass ich die Arbeit vorher nicht in einem anderen Prüfungsverfahren eingereicht habe und die eingereichte schriftliche Fassung der auf dem elektronischen Speichermedium entspricht. Ich bin mit einer Einstellung in den Bestand der Bibliothek des Fachbereiches einverstanden.

Hereby, I declare that the work in this dissertation was carried out in accordance with the requirements of the University's Regulations and that it has not been submitted for any other academic award. The work is the candidate's own work. Where certain information has been taken from the other sources is indicated as such. Any views expressed in the dissertation are those of the author. The submitted dissertation corresponds to the copy on the attached compact disc. I concur with the appearance of this work in the department library collection.

SIGNED: DATE:

Contents

Abstract	ii
Kurzfassung	iii
List of Figures	x
List of Tables	xiv
List of Abbreviations	xv
Objectives and structure of the Thesis	xvii
1 Introduction	1
1.1 Titanium Dioxide	1
1.2 Defects and Imperfections	3
1.2.1 Native Defects	3
1.2.2 Intentionally Induced Defects	4
1.2.3 Hydrogenation	5
1.3 Hydrogen Behaviour in Titania	5
2 Theory Behind Hyperfine Interactions	7
2.1 Hyperfine Interactions	7
2.2 Perturbed Angular Correlations	13
2.2.1 Angular Correlations	13
2.2.1.1 PAC-data Collection and Analysis	16
2.2.1.2 Temperature Dependence of the EFG	18
2.3 Mössbauer Spectroscopy	19
2.3.1 Mössbauer Effect & Recoil Free-fraction	19
2.3.2 Mössbauer Spectra Collection and Evaluation	19
3 Materials and Experiments Details	21
3.1 Sample Preparation	21
3.1.1 Charge Density Modelling with <i>Ab-initio</i> Calculations	22
3.2 Beam Production and Nuclear Solid-State Methods	23
3.2.1 TDPAC Spectroscopy at ISOLDE/CERN	24
3.2.2 Radiotracer Diffusion	27
3.2.3 Mössbauer Spectroscopy	28

3.3	eMS at ISOLDE/CERN	30
3.4	Sample Implantation	31
4	Local Probe Studies on Defect Dynamics in Titania	35
4.1	Hyperfine Interactions and Diffusion at Cd in Rutile Single Crystals . . .	35
4.1.1	Overview	36
4.1.2	Experimental	38
4.1.3	Results and Discussion	39
4.1.3.1	Annealing of the Local Environment	39
4.1.3.2	Cd-tracer Diffusion	42
4.1.3.3	<i>Ab-initio</i> Studies of the Electronic Structure	44
4.1.4	Conclusions	46
4.2	Defect Behaviour and Thermal Stability in Hydrogenated Anatase	47
4.2.1	Overview	47
4.2.2	Experimental Section	48
4.2.2.1	Sample Preparation	48
4.2.2.2	Sample Characterisation	49
4.2.3	Results and Discussion	49
4.2.3.1	General Characterisation	49
4.2.3.2	Emission Mössbauer Spectroscopy	52
4.2.3.3	<i>Ab-initio</i> Calculations	59
4.2.4	Conclusions	63
4.3	Cd-H Pairs in Rutile	64
4.3.1	Overview	64
4.3.2	Experimental	65
4.3.3	Results and Discussion	66
4.3.3.1	Stability of Cd-H	66
4.3.4	Conclusions	71
4.4	Influence of prolonged Hydrogenation on Titania	72
4.4.1	Overview	72
4.4.2	Experimental	73
4.4.3	Results and Discussion	73
4.4.3.1	Stepwise Hydrogen Reduction	73
4.4.4	Conclusions	76
5	eMIL - Emission Mössbauer System from Ilmenau	79
5.1	Design Overview	80
5.2	Hardware Set-up	80
5.2.1	Chamber Unit	82
5.2.2	Electronic Rack	84
5.2.3	Pumping Unit	86
5.2.4	Software	87
5.3	Future Updates	89
6	Conclusions and Perspectives	91
	List of own Publications	95

CONTENTS

ix

Appendix A

97

Bibliography

109

List of Figures

1.1	Crystal structures of TiO_2 polymorphs: (a) rutile; (b) anatase. Gray spheres represent Ti atoms, red are O atoms and the blue octahedra represent TiO_6 blocks.	2
2.1	Influence of the isomer shift on the nuclear energy levels.	8
2.2	Approximate ranges of isomer shifts for ^{57}Fe in various compounds. The ranges are given relative to $\alpha\text{-Fe}$ at room temperature. S stands for the spin quantum number.	9
2.3	The electric quadrupole interaction, which is visualised by the precession of the quadrupole moment vector about the field gradient, splits the degenerate $I = 3/2$ level into two substates with $m_I = \pm 3/2, \pm 1/2$. The current interaction gives rise to two transition lines with even intensity, which are separated by E_Q	11
2.4	The effect of magnetic splitting on the nuclear levels with no quadrupole splitting. The magnitude of splitting is proportional to the total magnetic field at the nucleus.	12
2.5	A $\gamma\text{-}\gamma$ nuclear cascade.	14
3.1	The ISOLDE hall. By courtesy of CERN.	25
3.2	Photography of a digital 6-Detector $\gamma - \gamma$ PAC spectrometer. Additional furnace can be mounted in the centre of the detectors. By courtesy of M. Nagl.	26
3.3	SRIM implantation profiles for rutile ($^{111m}\text{Cd}/\text{Cd}$, implanted at 30 keV) and anatase ($^{57}\text{Mn}/\text{Fe}$, implanted at 40 keV). Anatase is implanted at the incidence angle of 30°	27
3.4	Diffusion chamber installed at ISOLDE. By courtesy of D. Gaertner.	28
3.5	CEMS detector.	29
3.6	Deexcitation scheme of the ^{57}Fe absorber following resonant absorption of an incident γ -ray.	30
3.7	Photography of the current eMS experimental set-up at ISOLDE/CERN. Samples are mounted on various lids, so different experimental conditions can be created. Spectra are recorded using an avalanche parallel plate detector, which is filled with acetone vapours.	31
3.8	Decay schemes for ^{57}Mn and ^{57}Co nuclei, both decay into ^{57}Fe	32
3.9	Decay scheme for ^{111m}Cd nucleus. Intermediate PAC probe state has energy $E = 245.4$ keV and probes the local environment during the life time of the intermediate state of 84.5 ns.	32

4.1	Rutile lattice with incorporated Cd isotope at the cationic site. Grey spheres are Ti ions, while red represent O anions	36
4.2	XRD pattern of pristine samples prior to studies.	38
4.3	Perturbation functions for TiO ₂ samples implanted with ^{111m} Cd/Cd probe and measured at indicated temperatures. The red solid line represents experimental fitting.	39
4.4	Hyperfine parameters of TiO ₂ samples implanted with ^{111m} Cd/Cd probe and measured at indicated temperatures, accompanied by results of similar studies performed on bulk samples of rutile. For the convenience of following the trends data point were fitted with the polynomial regression function. The data from the references is shown for a good comparability, and belongs to the left axis (F.I). EFGs from references were recalculated utilising the last reported <i>Q</i> of Cd, based on the same first-principle calculations.	41
4.5	Penetration profile for Cd-diffusion measured at 873 K (blue circles). The red solid line corresponds to the fits by Eq.(4.1), and (4.2) and <i>x</i> is the penetration depth.	43
4.6	Two different Cd:Ti + V _o configurations in the 2 × 2 × 3 rutile supercell. Here (a) stands for V _o apical and (b) represents V _o equatorial. Titanium and oxygen atoms are denoted as grey and red spheres, respectively, while green ones show cadmium.	45
4.7	(a) XRD patterns and (b) UV-vis absorption spectra of as-prepared TiO ₂ and after annealing (pristine), the samples hydrogenated at RT TiO ₂ :H-RT and the sample hydrogenated at 573 K TiO ₂ :H-573 K.	50
4.8	XPS core spectra for Ti 2p (a-c) and O 1s (d-f) of TiO ₂ films before (a,d) and after hydrogenation treatments performed at room (b,e) and 573 K temperature (c,f).	51
4.9	(a-e) ⁵⁷ Fe emission Mössbauer spectra obtained at the temperatures indicated after implantation of ⁵⁷ Mn into pristine anatase TiO ₂ . (f) Magnified view of the spectra showing the effect of the magnetic splitting.	53
4.10	Temperature dependence of hyperfine parameters of Fe ²⁺ (D0). (a) Average isomer shift. The solid line shows the second-order Doppler shift. (b) Average quadrupole splitting. The solid line shows the linear trend above 373 K. (c) Area fractions of the spectral components of the spectra in Figure 4.9. (d) Relative standard deviation of the quadrupole splitting distribution function. The dashed line shows the average above 373 K.	54
4.11	⁵⁷ Fe emission Mössbauer spectra obtained at the temperatures indicated after implantation of ⁵⁷ Mn into TiO ₂ :H-RT.	55
4.12	Temperature dependence of hyperfine parameters of Fe ²⁺ (D1) for TiO ₂ :H-RT. (a) Average isomer shift. The solid line is a comparison to the SOD shift. (b) Average quadrupole splitting. (c) Area fractions of the spectral components of the spectra in Figure 4.11. (d) Relative standard deviation of the quadrupole splitting distribution function.	56
4.13	⁵⁷ Fe emission Mössbauer spectra obtained at the temperatures indicated after implantation of ⁵⁷ Mn into TiO ₂ :H-573.	57

4.14	Temperature dependence of hyperfine parameters of Fe^{2+} (D2) for $\text{TiO}_2\text{:H-573}$. (a) Average isomer shift. The solid line is a fit to the SOD shift. (b) Average quadrupole splitting. (c) Area fractions of the spectral components of the spectra in Figure 4.13. (d) Relative standard deviation of the quadrupole splitting distribution function.	58
4.15	Possible TiO_2 configurations reconstructed using <i>ab-initio</i> calculations: (a) Fe:Ti ; (b) Fe:Ti+V_o equatorial; (c) Fe:Ti+V_o equatorial nnn.; (d) Fe:Ti+OH\#1 ; (e) Fe:Ti+OH\#2	60
4.16	Densities of states for (a) Fe:Ti , (b) $\text{Fe:Ti+1}\bar{e}$, (c) Fe:Ti+OH\#1 m. , (d) Fe:Ti+OH\#2 , (e) Fe:Ti+V_o apical, (f) Fe:Ti+V_o equatorial.	62
4.17	PAC spectra as a function of hydrogenation temperature with the corresponding Fourier transforms. Solid lines are the least-squares fit of the appropriate theoretical function to the experimental data.	66
4.18	XRD patterns of hydrogenated rutile (a) and (b) the magnified (110) peak demonstrating a gradual shift.	69
4.19	Two different $\text{Cd:Ti + V}_o\text{+H}$ configurations in the $2 \times 2 \times 3$ rutile supercell. Here (a) stands for the case where V_o apical configuration is filled with hydrogen, while (b) represents V_o equatorial with placed hydrogen. Titanium and oxygen atoms are denoted as grey and red spheres, respectively, while pink and blue ones are cadmium and hydrogen.	71
4.20	^{57}Fe CEMS spectra with the simultaneous routine: (a) pristine, (b-f) hydrogenated at 573 K, (g) hydrogenated at 663 K and (h) annealed at 813 K. . . .	74
4.21	Area fractions obtained after a simultaneous fitting routine for the 573 K hydrogenated sample. There are two stages. The first stage (orange) demonstrates that the pristine sample is mainly characterised by Fe^{3+} which then starts to transform into Fe^{2+} during hydrogenation. While the second stage demonstrates a steady growth/recovery of Fe^{3+} . Blue area highlights the sample treated at 663 K. At this stage Fe^{2+} and Fe^{3+} behaviour resembles one seen after 30 of treatment. The white area represents the same sample annealed in air for 4 hours at 813 K and shows a vanishing of $\alpha\text{-Fe}$ and growth of Fe^{3+} . Points are connected with lines to highlight the dynamics.	76
5.1	Schematic diagram of the implantation chamber and the electronics generally used in for eMS.	81
5.2	Picture of the implantation chamber with the PPAC detector mounted on the transducer. The chamber is plugged to the pumping unit via a soft bellow, the last is used in order to minimise harmful vibrations originating from the pumps.	82
5.3	Illustration of the sample holder. There are four 1 inch (2.54 cm) button heaters mounted on ceramic substrates on separate beds (cells). Position of each sample can be adjusted by clamps, while the clamps are placed in a special way in order to minimise heat transfer to the other button heaters. Additional position is provided to a permanent $\alpha\text{-Fe}$ foil, for the calibration reasons. Thermocouples are plugged in through the connecting stems of heaters (underneath).	83
5.4	Schematic of the Y and Z drives control via Arduino Uno Rev3 and two CNC single routers TB6560.	84
5.5	Photo of the developed electronic rack. The flight case includes a NIM crate with data acquisition modules, computer, oscilloscope, bias.	85

5.6	Circuit diagrams of eMIL's vacuum systems. The used symbols were picked in accordance with DIN ISO 1219 and DIN 28401, as appropriate.	86
5.7	Quartz window, for light exposure experiments located next to the beam (through the GLM chamber) on the left and the Beryllium window on the right. . . .	87
5.8	eMIL's spectra viewer window, with statistical information.	88

List of Tables

1.1	Properties of rutile and anatase, TiO ₂	2
4.1	^{111m} Cd:TiO ₂ fitting parameters featuring two fractions. Here, ω_0 is given in Mrad·s ⁻¹ , δ and percentage are in % while V_{zz} numbers are presented in (10 ²¹ V·m ⁻²).	40
4.2	Comparison of calculated hyperfine parameters with current experimental data of TiO ₂ rutile. Current scenarios are: Cd at the Ti site, 1, 2 additional electrons; and V_{oap} . ap. and $V_{o eq}$. eq. are apical and equatorial oxygen vacancies, respectively. Me-O d_1 Me-O d_2 are the distances after relaxation given in Å, between Me and four and two oxygen neighbours, respectively. Results from other publications are shown for the comparison. Experimental data from the current work taken at RT. In d_1 for V_o eq. an average distance (of 3) is used. V_{zz} numbers are presented in (10 ²¹ V·m ⁻²).	44
4.3	Calculations obtained for TiO ₂ anatase. Here d_{AV} is the mean length of Fe-O bonds (Å). V_{zz} is the largest component (given in 10 ²¹ V·m ⁻²) and η is the asymmetry parameter of the EFG tensor. ΔE_Q and η are given in mm/s. U3 or U5 eV reflect when a charge is added to d -orbitals of Ti/Fe. Experimental data is for Fe ²⁺ component taken at RT. δ_A is the isomer shift, based on the empirical model by Gunnlaugsson <i>et al.</i> . Mark \diamond is added for a 3 × 3 × 1 SC. Equatorial and apical V_o - eq. and ap.; nnn stands for a next-nearest neighbour and m stands for a metastable state.	61
4.4	^{111m} Cd/Cd fitting parameters featuring main EFGs fractions. ω_0 is given in Mrad·s ⁻¹ , δ and perc. are in % while V_{zz} numbers are presented in (10 ²¹ V·m ⁻²). EFG of the same origin are marked with colours.	67
4.5	Derived hyperfine parameters for the hydrogenated spectra series. Here δ and ΔE_Q are given in mm/s, while B_{hf} is in T. Coloured cells correspond to hydrogenated states. Where error values are >0.01 is marked as such.	75

List of Abbreviations

MS	Mössbauer Spectroscopy
PAC	Perturbed Angular Correlation Spectroscopy
SOD	Second-order Doppler Shift
IS	Isomer Shift
EFG	Electric Field Gradient
QS	Quadrupole Splitting
ISOLDE	Isotope mass Separator On-Line facility
GIXRD	Grazing Incidence X-ray Diffraction
DFT	Density Functional Theory
LDA	Local-Density Approximation
GGA	Generalised Gradient Approximation
PBE	Perdew-Burke-Ernzerhof parametrisation of the GGA
PAW	Projector Augmented-Wave method
CEMS	Conversion Electron Mössbauer Spectroscopy
eMS	Emission Mössbauer Spectroscopy
GGA-WC	Generalised Gradient Approximation by Wu and Cohen
eMIL	Emission Mössbauer Spectrometer from Ilmenau
V_o	Oxygen Vacancy
$V_{o,ap.}$	Apical Oxygen Vacancy
$V_{o,eq.}$	Equatorial Oxygen Vacancy
V_{Ti}	Titanium Vacancy
Ti_I	Titanium Interstitial
H^+	Hydrogen Donor
H^-	Hydrogen Acceptor
H^0	Hydrogen Neutral

Colophon

This dissertation was conducted over the period from March 2017 to March 2020 at Werkstoffe der Elektrotechnik group, led by P. Schaaf. The current work was funded by Bundesministerium für Bildung und Forschung (BMBF) project 05K16SI1 and 05K16PGA. Additional funding was obtained from the European Union's Horizon 2020 research and innovation programme under grant agreement no. 654002 (ENSAR2). The author is grateful to CERN/ISOLDE for support of the experiment IS653. Obtained results are embodied in the current document. This document was typeset using the $\text{Xe}_{\text{L}}\text{TeX}$ typesetting system created by the Non-Roman Script Initiative and the memoir class created by Peter Wilson. The body text is set 11pt with Adobe Caslon Pro. Other fonts include `Envy Code R`, `Calibri` and `Optima Regular`. The template was initially developed by Federico Maggi and Vel, with further numerous modifications done by Dmitry Zyabkin.

SPONSORED BY THE



Federal Ministry
of Education
and Research



Objectives and structure of the Thesis

Materials based on TiO_2 are promising candidates for numerous applications. But the fact remains that, the coupling among various defects and their stability, as well as the lack of comprehensive theory is yet to be devised, understood and summed up.

The present dissertation addresses the production of such materials, structure modification (defects alteration, doping) and usage of advanced local techniques to study how crystal imperfections behave near the probes. There is a handful of methods which can bring new transparency on the electronic and defect structure in TiO_2 . These methods allow us to study the probe element local environment using hyperfine nuclear interactions, which are quite affected by the local defects. Studies require a fine quantity of foreign atoms to be included in desired materials, commonly via diffusion or ion implantation. The latter allows to control exactly the depth and concentration of isotopes. In the current study $^{57}\text{Mn}/\text{Fe}$ and $^{111\text{m}}\text{Cd}/\text{Cd}$ were implanted (at ISOLDE/CERN) and employed as probes for emission Mössbauer and Perturbed angular correlation spectroscopy, respectively. Both nuclear methods bear complementary characteristics to each other, whereas providing extreme sensitivity to the changes in magnetic and local atomic structures over a temperature range. Besides, these investigations are extended by supplementary studies.

Moreover, additional objectives were set to develop, construct and deliver a new versatile emission Mössbauer spectrometer to ISOLDE/CERN. Successful realisation of these aims is going to overcome the short comings of the old Mössbauer set-up as well as provide more reliable and precise working experience.

The current work consists of 6 chapters, starting with the introduction and theory about methods and hyperfine interactions, then moving on to materials and experimental details. Subsequent sections will discuss the obtained results and the newly developed spectrometer. Finally, the dissertation ends with conclusions and the future outlook. A brief summary of chapters is given as follows:

- **Chapter I** provides the reader with essential basics of the structure and physical properties of TiO_2 . The chapter includes an overview of defects and their influence on electronic structure, raises questions and doubts about charge states and behaviour of those defects and how their adjustment could beneficially affect optical absorption.
- **Chapter II** familiarises the reader with hyperfine interactions and methods which allow to probe them.
- **Chapter III** presents an overview of how the samples were made, treated and measured later on. This includes experimental details on the beam production at ISOLDE/CERN and applied methods of nuclear solid-state physics.

- **Chapter IV** contains experimental data. It is divided into 4 parts, where 2 parts consider hydrogen doping, its structural influence and stability. While the other two deal with continuous hydrogen plasma reduction and impact of V_o on hyperfine properties and diffusion in TiO_2 .
- **Chapter V** presents/discusses the newly built emission Mössbauer spectrometer set-up. At this point, the design and construction part is covered in details.
- **Chapter VI** includes conclusions and outlook, summarises results and provides possible ways to expand knowledge about TiO_2 imperfections further. The chapter is followed by a list with the author's scientific publications, which have been published over the course of the PhD study.

Introduction

1

Metal oxides, originally regarded as insulators, are currently proving to be important semiconductors. The minima of conduction band in those semiconductors are rather low, on the absolute energy scale (i.e., they possess high electron affinity). The latter is related to the noteworthy properties of TiO_2 , which are of big use in dye-sensitised solar cells [1], photocatalytic hydrogen production [2], the reduction of global atmospheric pollution [3], water purification [4] and CO_2 reduction [5]. Furthermore, it has been theoretically predicted that transition metal doped non-magnetic metal oxides could exhibit ferromagnetic behaviour at room temperature and beyond (due to carrier-mediated magnetic interactions) [6]. The above-mentioned properties, combined with thermal and chemical stability, make TiO_2 an interesting candidate for the multiple applications. The optical and electrical properties of the TiO_2 -based materials, however, are subject to big influence of intrinsic and extrinsic defects. Therefore, substantial effort has been devoted to improving its photocatalytic activity by adding and altering crystal imperfections. Owing to rather complicated crystal structures, it has been fairly difficult to perform reasonable theoretical simulations explaining the origin of possible changes observed from experimental data.

1.1 Titanium Dioxide

Titanium dioxide (titania, TiO_2) has three main phases: anatase and rutile (tetragonal) and brookite (orthorhombic); and numerous minor phases such as TiO_2 -B ($C2/m$), TiO_2 -R ($Pbnm$), TiO_2 -H ($I4/m$), TiO_2 -II ($Pbcn$) and TiO_2 -III (P_2/C) [7, 8]. Amongst all three main phases, rutile is the most stable and common form. As only anatase and rutile are manufactured on a large scale and play a significant role in the applications, the current study is going to be limited to them. Selected properties are shown in Table 1.1.

Both structures are tetragonal and slightly distorted, consisting of Ti ions surrounded by 6 oxygen anions. In addition, it should be noted that in both structures the two bonds between Ti and O atoms (at the apices of the octahedron) are a bit longer. Anatase, shows a deviation from a 90° bond angle. In rutile (shown in Figure 1.1a), octahedral corners are shared along $\langle 110 \rangle$ direction and are stacked by their long axis changing by 90° . With

Table 1.1: Properties of rutile and anatase, TiO_2 .

Feature:	Rutile:	Anatase:
Bandgap (eV)	3.05	3.2
Density (g/cm^3)	4.23	3.78
Space group and class	$D_{4h}^{14} - P4_2/mnm$	$D_{4h}^{19} - I4_1/amd$
Unit cell (\AA)	a=b=4.594 c=2.959	a=b=3.733 c=9.370
Atomic radius (nm)	O = 0.066 (covalent); Ti = 0.146 (metallic)	
Ionic radius (nm)	$\text{Ti}^{+4} = 0.064$ and $\text{O}^{-2} = 0.14$	
Melting point (K)	2116	
Crystal system	Tetragonal	

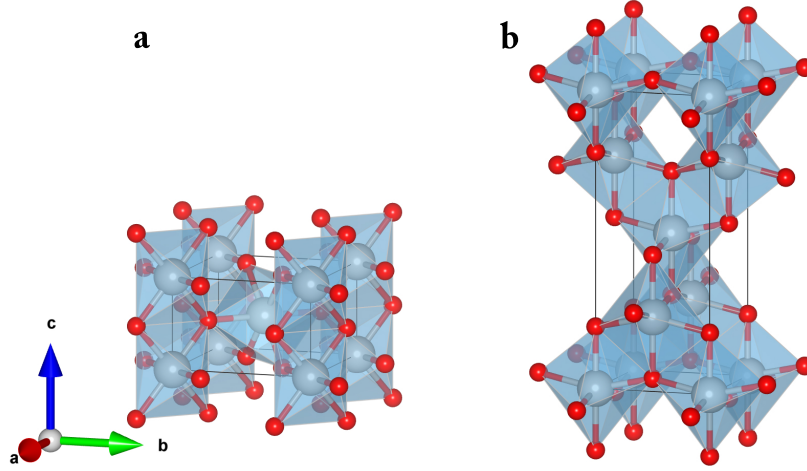


FIGURE 1.1: Crystal structures of TiO_2 polymorphs: (a) rutile; (b) anatase. Gray spheres represent Ti atoms, red are O atoms and the blue octahedra represent TiO_6 blocks.

regards to anatase, these octahedra form (001) planes (see Figure 1.1b). Planes connect with the plane of octahedra which is located below. The stacking of the octahedra results in three-fold coordinated oxygen atoms [9].

As it is clearly seen in Table 1.1 both polymorphs have a large electronic bandgap of 3-3.2 eV. This fact imposes severe limitations on the optical absorption and limits it only to certain amount of UV light [10]. Even with UV light, photocatalytic activity is not so simple and depends strongly on the amount of holes and electrons at the surface participating in reactions. In this case, a quantum of light (energy is bigger than the bandgap) gets absorbed, and in the conduction band an excited electron appears, while a hole appears in the valence band of TiO_2 . These excited carriers could diffuse to the surface within a certain period of time. A ratio between the time and amount of excited carriers determines the fraction,

which is going to take part in the photocatalysis. Nevertheless, a certain amount of these carriers may swiftly recombine, and thus vanish. The quantity of these generated carriers at the surface depends directly on the amount of absorbed light. Therefore, it has become a logical consequence to intensify the optical absorption, and thus increase performance of TiO₂-based materials. As it is well-known that optical and electronic properties in solids depend highly on the structure, phases and defects. Hence, by adjusting these features it becomes possible to tailor electronic and optical properties. There have been plenty of reports on the successful absorption boosting with metal doping [11, 12], anion doping [13, 14] and self doping [15, 16]. However, often during the bandgap reduction, the dopants can start acting as carrier scattering centres and traps, therefore decreasing chances for carriers to reach the surface.

1.2 Defects and Imperfections

1.2.1 Native Defects

Regardless of the fact, that TiO₂ has been studied for several decades there are numerous questions that need answering. Most of them are related to the inner defects, which are commonly present (native defects) depending on the growth conditions. They can be featured in various forms with multiple charge states, and remarkably influence the photocatalytic performance. Point defects include oxygen vacancies (V_o), titanium vacancies (V_{Ti}), interstitial titanium (Ti_I), doping-induced interstitials and substitutional atoms. Occasionally, one may find planar and volume defects. The charge balance in the lattice is mainly maintained by V_o , in order to compensate for cations of valence smaller than Ti^{4+} , several oxygen sites remain to be vacant. As each oxygen is surrounded by three Ti atoms in the lattice (distance among is 1.94 - 1.99 Å), then as a result a formation of V_o creates three cations next to it in the pyramidal coordination. It is a widely held view that the origin of dilute magnetic semiconductors lies in V_o [17].

It is generally believed that V_o and Ti_I are responsible for n -type conductivity seen in stoichiometric samples [18, 19]. Once the system receives additional electrons they can localise at Ti-3d orbitals, promoting Ti^{3+} ions. This causes a relaxation of the surrounding lattice (typically ~ 0.1 Å). The new configuration, made of an electron coupled to the relaxation of the surrounding lattice is known as a small polaron. When the temperature rises, this polaron starts hopping to neighbouring sites [20]. In the case where structural deformation spreads over several lattice sites the configuration is called a large polaron [21].

It has commonly been assumed that the influence of defects differs in these two polymorphs. For instance, doping anatase with Nb gives rise to a shallow state, changing the material into a transparent conductive oxide (at high concentrations), while rutile with the same amount of Nb remains as insulator (due to a Nb-induced deep level in the bandgap) [22, 23]. This behaviour could be explained in terms of rutile's tendency to trap electrons at the cation lattice [24]. This trapping gives rise to polaronic, deep states (neighbourhood of the dopant). Oxygen vacancy (V_o) undergoes the same route, and normally loses its 2 electrons, even in oxidised samples for such trap states [25]. On the contrary, in the bulk anatase, there are no such trapping sites and Nb provides an effective mass theory like donor state. Identically, V_o in the bulk anatase keeps its two electrons [26]. As a result in anatase, V_o contribute significantly to an electron excess of the lattice. However, charge distribution at the anatase's surface resembles charge distribution in rutile, where electrons go to the surface traps at a

sixfold coordinated (6c) site with much more deeper ionisation energy than in the bulk [26]. Based on the aforementioned features, one may conclude that in rutile, electron excess can localise at any lattice Ti ion, forming a small polaron. In contrast, in anatase electrons are in a free-carrier state [20].

It is worth mentioning, that tiny electron polarons may form at some anatase surfaces, whilst this may not be the case at some rutile surfaces [26, 27]. This could suggest that the existence of polaron states relies on the local geometrical constraints. Moreover, several vacancies could interact with each other, and lead to the shallower defect states. If they are shallower, their donors' activation energy is lower, which enviably leads to a spike of conductivity. The forces of attraction among these V_o likely arise from the polaronic effects. These effects may stir the electron excess, in order to decrease the Coulomb repulsion [28]. When the amount of V_o rises it may lead to a clustering of such defects and forthwith TiO_2 becomes metallic. In the case when vacancies have long-range order, one may have the crystallographic shear bands formation, which could eventually lead to Magnéli phases (Ti_nO_{2n-1}) [29–31]. These phases have metallic conductivity, which can be employed in fuel cells as electrode materials [32]. Since the majority of studies have focused on the surface of TiO_2 it is yet to be fully understood whether annealing under oxygen-rich/poor atmosphere actually affects the materials as a whole or just affects the sub surface layers [19].

Another intrinsic defect is hydrogen, which is known for being a common impurity in oxides with a strong impact on properties of such materials. As it happens, hydrogen may act fairly differently from one system to another. For instance, interstitial hydrogen forms -OH bonds in both ZnO and TiO_2 , the formation is different though. In the case of ZnO, hydrogen can break a bond and use two pathways to form -OH structures (more stable bond-centred position and anti-bonding position) [33]. While in the case of TiO_2 the 3-fold coordinated oxygen forms a dative bond and leaves the lattice structure undisturbed [34]. As hydrogen's behaviour is quite uncertain and tangled it is going to be reviewed fully in Section 1.3.

1.2.2 Intentionally Induced Defects

As mentioned above the defects can open a broad, yet perplexing pathway, leading to improved properties. While volume defects always cause the unpleasant outcomes and lower performance, linear and planar defects are in fact defects which might potentially be of use. However, considerate attention has to be paid to the point defects. Amongst the wide spread TiO_2 polymorphs, rutile needs the highest formation energy for a V_o to appear (rutile 5.82 eV > anatase 5.58 eV > brookite 5.52 eV) [35]. There are differences in formation tendency as well. The stablest anatase surface (101) seemingly does not have that pronounced of an ability to favour V_o (unlike surface (110) in rutile) [36].

As it is well-known a V_o is formed, once an oxygen atom gets knocked out from the lattice. There is a plethora of methods which have been reported on making metal oxides defective. Performing annealing in an inert atmosphere is most used. Another way is via exposing samples to UV irradiation, which could induce vacancies formation. However, in this case an additional reducing agent is needed, since irradiation energy often falls short (energy has be $\geq 6-7$ eV) [35]. Mechanical grinding TiO_2 with $NaBH_4$ and adding subsequent annealing in Ar has similar impact. Electron irradiation can also induce vacancies, which are primarily localised on the surface [37].

Assuredly, ion implantation is one of the straight-forward ways used to create Ti_I and V_o . The method is often used in order to dope materials with other elements as well as for local probe studies [38, 39]. Dopants could substitute Ti or O atoms and/or become an interstitial defect. Furthermore, dopants could introduce new impurity levels and decrease the bandgap. Although, these are dependent on several factors and could affect properties both ways (may serve centres for carriers recombination).

1.2.3 Hydrogenation

There are several ways in which one may dope TiO_2 with hydrogen. These include: annealing in H_2 atmosphere, implantation and hydrogen plasma treatment [40–43]. Perhaps, the most easily performed method is heat treatment in H_2 atmosphere. Annealing provides relatively homogeneous concentration with quantities being quite close to the equilibrium. For this reason one cannot introduce more hydrogen above the sample's solubility limit. It is therefore possible to extend concentration by carrying out annealing at elevated temperatures and high pressure, causing some additional damage to the lattice. In 2011, Chen *et al.* have applied annealing in hydrogen atmosphere on pristine powders of TiO_2 [40]. They observed a solid increase of light absorption in the whole visible range and called the obtained materials — black titania. The latter is related to both hydrogen doping and simultaneous creation of V_o .

Ion implantation with hydrogen allows for achieving a relatively high quantity of dopant. By varying ion energy, dose and time one could precisely control depth and desired amount. However, the latter causes significant lattice damage and could require annealing in order to remove damage, unfortunately losing the majority of implanted hydrogen.

Similarly, one could treat samples in hydrogen plasma. This action results in high concentrations of dopant even at low temperatures. However, the used parameters requires one to be careful and attentive to plasma properties, otherwise the surface could undergo substantial damage. The vital parameters here are the hydrogen flux and the energy of the ions, both are sensitive to gas pressure. As an example, exposing TiO_2 to hydrogen plasma made it possible to significantly improve absorption of TiO_2 , even in comparison to the original black TiO_2 [44]. The obtained structure was classified as a core/shell structure. In this case hydrogen behaviour is very similar to what Ag or Pt loading in TiO_2 looks like (high light absorption and low recombination). Plasma treatment highly affected the upper-layers, converting Ti^{4+} ($3d^0$) into Ti^{3+} ($3d^1$) by adding hydrogen dopant and V_o . In this case, the structure could feature titanium sub-oxides (Ti_2O_3 and Magnéli phases) and break the lattice symmetry only in certain unit cells. However, there have been several studies where the received results did not show any Ti^{2+} ions and V_o presence, but solely Ti-OH and Ti-H formation. Particularly, -OH and -H formation took place at relatively high temperatures and intensity [45–47].

1.3 Hydrogen Behaviour in Titania

In general, a hydrogen impurity shows amphoteric behaviour in the majority of semiconductors. Hence, in materials demonstrating the p -type conductivity it behaves as a donor, while n -type semiconductors make it act as an acceptor. Peculiarly, in ZnO, SnO_2 and TiO_2 systems it tends to feature the donor behaviour. The reason so far remains elusive. Calculations in metal oxides are fairly challenging, because of underestimation of the band gap and

spurious electron self-interaction in the standard semi-local implementations (polaronic effects) [24]. There have been theoretical calculations on possible hydrogen behaviour and forms it could take in TiO_2 . Most of the calculations suggest the following: that hydrogen is a shallow donor in rutile [48, 49], can be present in several forms and occupy various lattice sites depending on its charge: H^+ , H^- and H^0 . On the contrary, if calculations take into account the polaron formation (see Section 1.2.1) within the supercell, it may add deep donor levels to the bandgap [24, 50]. It is important to point out that it has been considered that H^0 acts as a shallow donor as well.

Experimental studies found that hydrogen was indeed showing markers belonging to shallow states at the edge of the conduction band [48, 51] as well as had several forms [52]. Positively charged (H^+) atoms tend to settle in regions with high density of electrons and vice versa for H^- . The feature is governed by Coulomb potential, and happens to an isolated hydrogen across all semiconductors [53]. Unfortunately, this cannot be applied to a neutral hydrogen H^0 . Taking into account that H^0 escapes the potential's influence, one may assume it has higher energy than those H^+ and H^- forms. Moreover, H^0 is metastable so as it may decrease its energy when another H^0 interacts with it (e.g., $2\text{H}^0 \rightarrow \text{H}^+ + \text{H}^-$).

Besides uncertainties about hydrogen forms in TiO_2 , there are questions regarding its diffusion and thermal stability. As a shallow donor, hydrogen ionises to H^+ with a delocalised electron in the conduction band, and thus a H^+ establishes a strong bond to an O atom. When hydrogen acts as a deep impurity it may form several longer (weak) bonds to some oxygen anions and become a metastable interstitial (H_i^\bullet) [51, 54]. When samples are neither doped nor reduced it is likely that $-\text{OH}$ formation will take place (lowest formation energy for all Fermi levels and oxygen chemical potentials) and become a predominant state [55]. Theoretical investigation suggests that there could be a deep state H^0 , located in the oxygen vacancy with two sturdy bonds to Ti atoms [50].

Hydrogen could interact with itself and form H_2 molecules. Dissociation of these bonds is directly governed by the system energy. Usually, H^+ movement includes: 1) breaking the bonds 2) reorientation of $-\text{OH}$ [56] and in order to break the bonds high temperature has to be achieved. The movement is anisotropic, and preferably it gets transferred along the c -axis, where the energy barrier is smaller, rather than through channels in $a - b$ plane [57]. This H_2 form may also get trapped at the interstitial site, V_o formations, interstitial impurities [58, 59]. Presently, there is no reliable information available regarding the stability of the interstitial hydrogen and its charge, how it interacts with the lattice and V_o , how it transforms into $-\text{OH}$ [60].

In this chapter, a brief theoretical overview of the employed methods that allow to probe the local environment in solids is presented. Both used techniques, *Mössbauer Spectroscopy* (MS) and *Perturbed Angular Correlation Spectroscopy* (PAC), bear the complementary character, measure the nuclear hyperfine interactions with the material charge distribution in the probe's nuclear neighbourhood and are based on the usage of radioactive probes. In the case of PAC studies, the parameter governing the magnitude of the observable effect is the temperature independent angular correlation coefficient A_{kk} , while for MS studies there is Debye-Waller factor. Since the lattice parameter is temperature dependent, it becomes more complicated to perform MS studies at high temperatures. None the worse, this dependence allows one to study dynamic effects, which is not feasible for PAC studies. Furthermore, MS is able additionally to determine isomer shift. However, the spectra can become remarkably complex due to the variety of possible interactions, which could hinder their interpretation in a unique way. It is difficult to detect the presence of non-resonant probe atoms when one deal with MS, while in the case of PAC those atoms decrease the observed correlation coefficient A_{kk} , thus can be extricated effortlessly. Regardless, MS cannot replace PAC and vice versa due to the factors depending on different isotopes as well as direct (MS) and indirect nature (PAC) of the local examination. Both these aspects are going to be covered in more details in this chapter, with additional references provided where in-depth knowledge is required. Nonetheless, the quantum-mechanical formalism is not covered here in full, as one can find additional references elsewhere [61, 62].

2.1 Hyperfine Interactions

The interaction of the charge distribution of atomic nuclei with the electromagnetic fields created by the external charge distribution, due to the atomic shell electrons and all the additional charges from where the nuclei are embedded, are called the (nuclear) hyperfine interactions. Because of these interactions the nuclear and atomic levels become perturbed, split or shifted. The interactions are well described by the Hamiltonian in terms of a multipole expansion, where both the charge distributions of the nucleus and of the external

charges will be decomposed on multipole series of so-called momenta:

$$\hat{H} = \hat{H}_{IS} + \hat{H}_Q + \hat{H}_M + \dots, \quad (2.1)$$

where \hat{H}_{IS} stands for the electric monopole, \hat{H}_M the magnetic dipole and \hat{H}_Q for the electric quadrupole interactions. Each Hamiltonian of the equation (2.1) can be expressed as the product of a nuclear moment and the corresponding term of the electromagnetic field. Therefore, a survey of these hyperfine interactions yields information on both the solid-state surroundings and the nuclear moments.

Particularly, \hat{H}_{IS} demonstrates the electrostatic Coulomb interaction between the nuclear charge (spread over a finite volume) and electrons inside the nuclear region. Since the nuclear volumes are different at each excitation state, the electrostatic shifts are also different for each nuclear state. One could see in Figure 2.1, that nuclear levels of the ground and excited states are shifted. As in various chemical environments of different materials the configuration of the electron shell differs, thus chemical surroundings in various materials can be distinguished by the energy shifts of the nuclear levels. This isomer shift is expressed as follows:

$$\Delta E_{IS} = \frac{2\pi}{3} z S'(z) e \Delta\rho(0) (\langle r^2 \rangle_e - \langle r^2 \rangle_g). \quad (2.2)$$

Here, $\langle r^2 \rangle_e$ and $\langle r^2 \rangle_g$ are the mean squares of the charge radii of the excited state and the ground state, $\Delta\rho(0) = e(|\psi_r(0)| - |\psi_s(0)|)$ represents the difference between the s electron charge densities at the nuclei in the reference (or absorber) and the source, e is the elementary charge, $S'(z)$ is the relativistic factor (employed for heavy elements, until iron) where z stands for the number of protons.

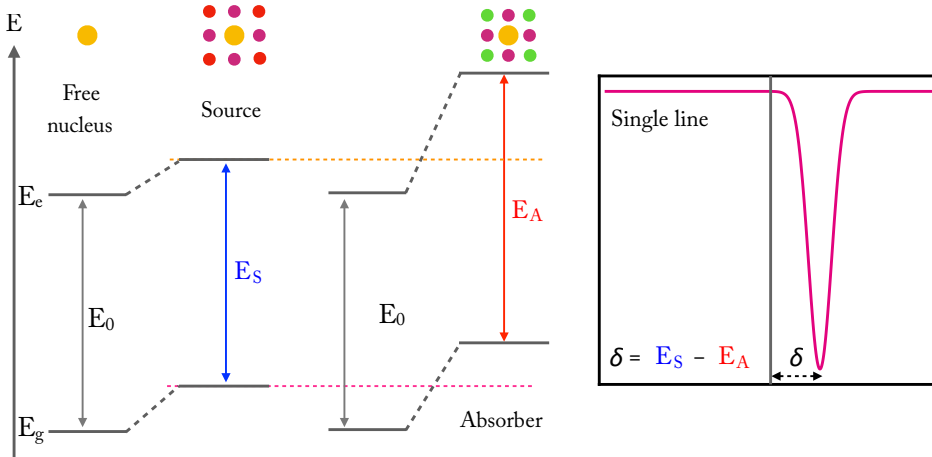


FIGURE 2.1: Influence of the isomer shift on the nuclear energy levels.

Equation (2.2) evidently shows that the isomer shift is in essence a measure of difference of s electron densities at the nuclei in the reference and source. It is important to point out that there are two main factors which determine the electron density at the nuclear site. The first factor is due to the inner s electrons of the Mössbauer atom, while the second is

from the valence electrons of the outer shell and electrons of ligands. Surely, the first is not sensitive enough to the changes in the local chemical environment thus often it is taken as a constant. The second factor is more developed and consists of two contributions: 1) changes in the s electrons of the valence shell, affecting $\rho(0)$ — a direct interaction; 2) changes in the shielding of the s electrons (when p , d and f electrons increase or decrease) — an indirect interaction.

The *Isomer Shift* (IS) demonstrates that any change in bonding, coordination number, spin, electronegativity of a ligand or oxidation state influences the s -electron density, hence providing opportunities to characterise chemical and magnetic properties of a material [62]. Figure 2.2 illustrates a schematic guideline of isomer shifts for various oxidations states (and spins) with their velocity ranges [62]. As one may notice, under certain circumstances ($\delta = 0.4$ mm/s) it is not possible to distinguish an exact oxidation/spin state on a basis of velocity range alone. In order to overcome this drawback one may need to know the natural valence state of Fe in the studied lattice, quadrupole and magnetic hyperfine interactions which might hint on possible configurations.

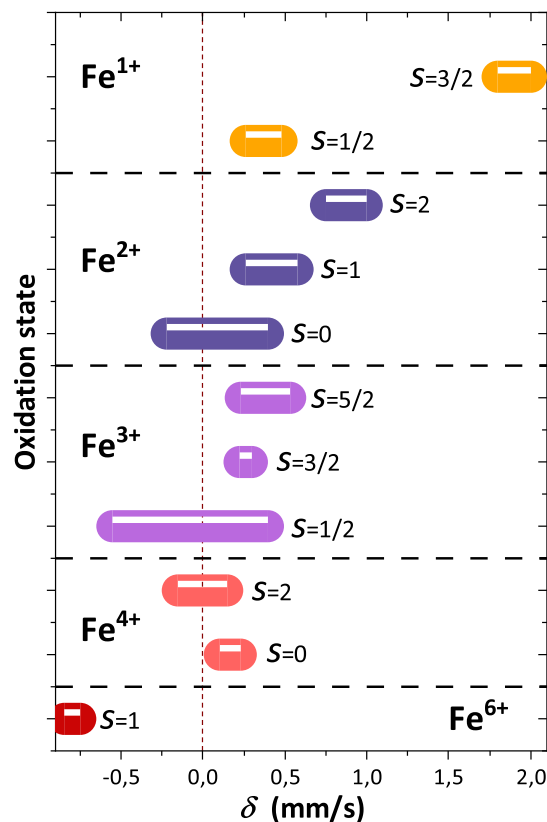


FIGURE 2.2: Approximate ranges of isomer shifts for ^{57}Fe in various compounds. The ranges are given relative to $\alpha\text{-Fe}$ at room temperature. S stands for the spin quantum number.

During Mössbauer experiments, when the source and absorber have a different electronic environment, it results in a shift of the necessary Doppler velocity to attain the ab-

sorption resonance as shown in Figure 2.1 [63]. The single absorption or emission line is commonly called singlet.

However, starting from certain temperatures there is a thermal motion (lattice vibrations) causing a temperature dependent shift, which is attributed to the atomic mean-square velocity of the nuclei $\langle v^2 \rangle$. Let us assume that the source and the reference are at different temperatures T_s and T_r . This impacts the experimental isomer shift by adding the so-called *Second-order Doppler Shift* (SOD) δ_{SOD} and the observed shift of the whole spectrum is called the centre shift:

$$\delta E = \delta E_0 + \delta_{SOD} = \delta E_0 + \frac{\langle v^2 \rangle_{T_s}}{2c} - \frac{\langle v^2 \rangle_{T_r}}{2c}; \quad (2.3)$$

$$\delta_{SOD} = \frac{-E_\gamma \langle v^2 \rangle}{2c^2}. \quad (2.4)$$

Probing temperature dependences of SOD, one can obtain insight of the Debye temperature.

The next term of equation (2.1) represents the energy contribution of the electric quadrupole interaction \hat{H}_Q . This contribution can be experimentally detected by both PAC and MS methods, when a nuclear probe state with an angular quantum number $I > 1/2$ is used (applicable for both isotopes $^{57}\text{Mn}/\text{Fe}$ and $^{111m}\text{Cd}/\text{Cd}$ used in this work), since in this case it has non-spherical charge distribution and $Q \neq 0$. If the last condition is fulfilled, it can interact with the non-homogeneous electric charge distribution at the nucleus. The deviation from a spherical symmetry of the external charge distribution is described by the *Electric Field Gradient* (EFG) and is a 3×3 second-order tensor of second derivatives of the electric potential in a Cartesian coordinate system [62]:

$$V_{ij} = \frac{\partial^2 V}{\partial x_i \partial x_j}, \quad \text{where } (i, j = x, y, z). \quad (2.5)$$

As it is possible to determine a coordinate system in a way where one has $V_{ij} = 0$ for a condition $i \neq j$ and $V_{xx} + V_{yy} + V_{zz} = 0$ (the tensor is traceless) then the EFG becomes characterised by only two principal components (for its traceless character): 1) largest eigenvalue V_{zz} (since the impact of V_{xx} and V_{yy} can be neglected); 2) its axial asymmetry parameter as η :

$$\eta = \frac{V_{xx} - V_{yy}}{V_{zz}} \quad \text{for which } 0 \leq \eta \leq 1. \quad (2.6)$$

Here, η provides information on the deviation of the EFG from the axially symmetric state in the lattice ($\eta = 0$).

For scenarios where a nucleus site is characterised by a threefold axis of symmetry, one obtains a symmetric EFG $V_{xx} = V_{yy}$ and therefore $\eta = 0$. The electric quadrupole interaction splits the $2I+1$ -fold degenerate energy level of a nuclear state into substates $|I, \pm m_I \rangle$. For instance for ^{57}Fe one has $I_e = 3/2$ and $Q \neq 0$, however in the ground state $I_g = 1/2$, which results in no splitting since $Q = 0$, and also becomes a twofold degenerate level. The latter can be lifted by the magnetic perturbation [62]. Therefore, the energy of sub-levels is calculated by:

$$E_Q = \frac{eQV_{zz}}{4I(2I-1)} [3m_I^2 - I(I+1)] \sqrt{1 + \frac{\eta^2}{3}}, \quad (2.7)$$

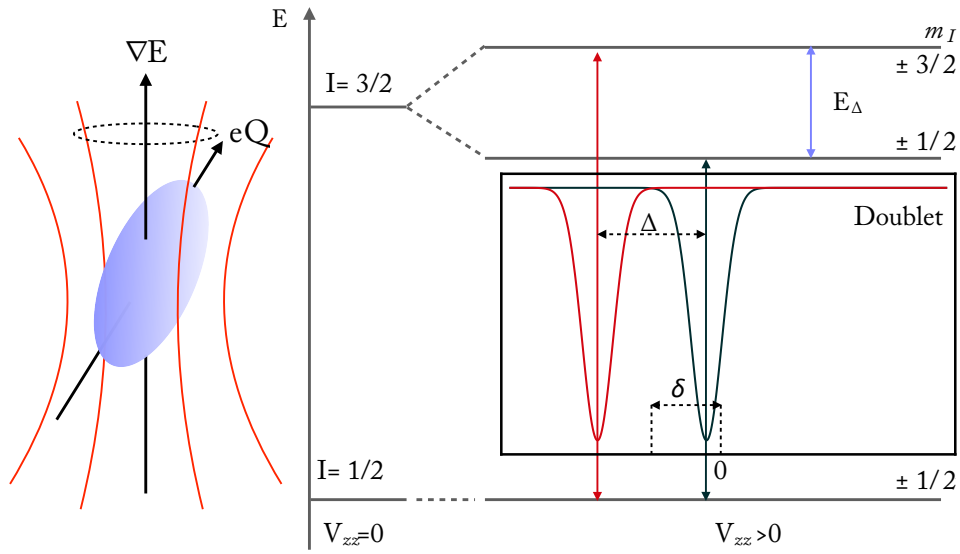


FIGURE 2.3: The electric quadrupole interaction, which is visualised by the precession of the quadrupole moment vector about the field gradient, splits the degenerate $I = 3/2$ level into two substates with $m_I = \pm 3/2, \pm 1/2$. The current interaction gives rise to two transition lines with even intensity, which are separated by E_Q .

where m_I stands for the magnetic quantum number of the sub-level, Q is the electric quadrupole moment of the nucleus and e is the elementary charge. On the one hand, when $\eta = 0$ one has the difference in energies expressed:

$$\Delta E_Q = (E_m - E_{m'}) = \frac{3eQV_{zz}}{4I(2I-1)} |m^2 - m'^2| = 3|m^2 - m'^2| \hbar \omega_Q, \quad (2.8)$$

where ω_Q is the quadrupole frequency of the interaction and the quantity is always an integer. ω_Q does not depend on the magnetic quantum number of the sub-levels. The latter defined as:

$$\omega_Q = \frac{eQV_{zz}}{4I(2I-1)\hbar}, \quad \omega_0 = k\omega_Q, \quad (2.9)$$

here I is the nuclear spin of $5/2$ (for ^{111m}Cd) and k is 3 (or 6) for integer (half-integer) spin when the asymmetry parameter is equal to zero. Instead of ω_0 , which is spin dependent, the quadrupole coupling constant ν_Q is usually employed [64], where:

$$\nu_Q = \frac{eQV_{zz}}{h}. \quad (2.10)$$

The energy gap between split sub-levels, is called the *Quadrupole Splitting* (QS) On the other hand, if $\eta \neq 0$ then the dealing becomes more sophisticated and the sub-levels are given by superposition of m_I -states. In this case the intensity of the transition can fluctuate in accordance with the superposition law and η . Regardless the nuclear states, which have half-integer spin are never fully split by pure quadrupole interaction, and pairs of

m_I -states (Kramer's doublets) remain doubly degenerate for any η value [62, 65]. Generally, the EFG V_{zz} has two contributions. First contribution is originating from the charges on neighbouring ions around the probe in non-cubic symmetry, commonly known as the lattice contribution. Second one, arises from the valence electron anisotropic distribution of the probe and called valence electron contribution. Figure 2.3 shows a typical case of a Mössbauer spectrum with a quadrupole doublet component (or simply doublet) [63].

The next term in the equation (2.1) is the magnetic hyperfine interaction \hat{H}_M . The interaction results in a nuclear splitting of the nuclear state with spin quantum number $I > 0$ into $2I + 1$, resembling how it happens when one uses methods of optical spectroscopy (so-called Zeeman splitting). Here, the interaction takes place between the nuclear magnetic dipole moment μ and the magnetic field at the nucleus. Diagonalisation of \hat{H}_M gives the eigenvalues for sub-levels:

$$E_m = -g_N \mu_N m_I |\mathbf{B}_{eff}|, \quad (2.11)$$

where g_N stands for the Landé factor, $\mu_I = \frac{e\hbar}{2mp_c} \approx 5.051 \cdot 10^{-27} J/T$ is the nuclear magnetron, m_I stands for magnetic quantum numbers of a certain level with a spin I and $|\mathbf{B}_{eff}|$ is an effecting magnetic field at the nucleus.

Figure 2.4 shows the effect of the interaction where $I = 3/2$ and $1/2$ spin states are split into four and two substates [63]. The allowed transition between sublevels follow the selection rules $\Delta m = 0, \pm 1$ and $\Delta I = 1$ and allows 6 possible transitions. Therefore, it results in a spectrum split into 6 lines, which is also known as a sextet pattern. Relative intensities of the absorption peaks depend on the direction of the hyperfine magnetic field, with respect to the direction of the incident photons ($\vec{\gamma}$). However, in polycrystalline powdered samples, the hyperfine field is randomly oriented in respect to $\vec{\gamma}$, resulting in a relationship among the peaks of 3:2:1:1:2:3.

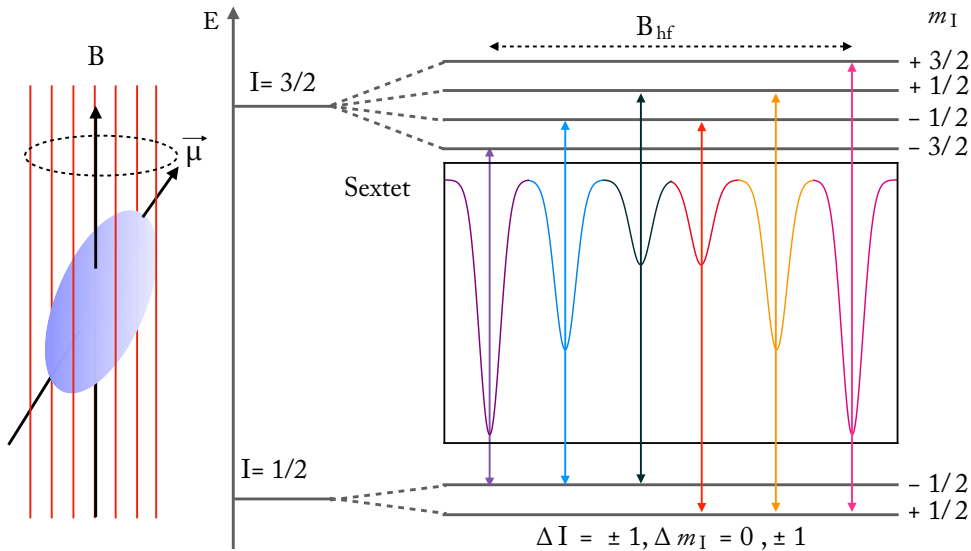


FIGURE 2.4: The effect of magnetic splitting on the nuclear levels with no quadrupole splitting. The magnitude of splitting is proportional to the total magnetic field at the nucleus.

As the magnetic splitting is a vector sum of two contributions (constant nuclear term and a variable term influenced by the electronic structure) it is usually called the effective field \mathbf{B}_{eff} :

$$\mathbf{B}_{eff} = \mathbf{B}_{loc} + \mathbf{B}_{hf}, \quad \text{where} \quad \mathbf{B}_{hf} = \mathbf{B}_{core} + \mathbf{B}_{orb} + \mathbf{B}_{dip} + \mathbf{B}_{trhf}, \quad (2.12)$$

here \mathbf{B}_{hf} stands for a sum of fields from both indirect and direct interactions of the electronic system with the nucleus, \mathbf{B}_{core} is Fermi contact interaction and bears the main contribution, \mathbf{B}_{orb} is the orbital magnetic term, \mathbf{B}_{dip} is the dipolar term and \mathbf{B}_{trhf} is a transferred hyperfine field. The last term is due to the interaction between the spin of the nucleus and the spin of magnetic ions surrounding the nucleus. The dipolar term originates from a direct interaction of spins from nucleus and valence electrons. \mathbf{B}_{orb} exists because of the interaction of the magnetic moment of the nucleus with the total orbital angular momentum of electrons in the open shells. \mathbf{B}_{core} arises from the the spin polarization of core electrons. \mathbf{B}_{loc} is determined by external conditions (such as external applied magnetic field \mathbf{B}_{ext}) and provided by a vector sum $\mathbf{B}_{loc} = \mathbf{B}_{ext} + D\mathbf{M}$ where D is the demagnetisation factor and \mathbf{M} magnetisation).

Before discovery of the Mössbauer effect it was impossible to measure the magnetic hyperfine interaction for both excited and ground states simultaneously. PAC spectroscopy, however, can capture, although only for the excited state [62, 65].

2.2 Perturbed Angular Correlations

Perturbed angular correlations or simply PAC (TDPAC for Time-Differential, which is used in the current work) spectroscopy is widely used experimental technique to study hyperfine interactions in solids, liquids and soft matter. The method is well applied for studying of electric quadrupole and magnetic dipole interactions and consequently used to investigate various features such as: defects (types, orientations, annealing behaviour), magnetism (spin dynamics, exchange interactions, stability of magnetic moments), phase-transformation, formation of precipitates [66]. Most noticeable advantages of the method include things such as temperature independence (unlike it happens in the case of MS, where one is limited by Debye-Waller factor) and the needed amount of atoms is extremely diluted 10^{11} . Since the theoretical foundations of PAC is fairly complex solely a brief description will be given. More detailed insight can be found elsewhere [61].

2.2.1 Angular Correlations

Method of perturbed angular correlations is based on the consecutive emission of a cascade consisting of $\gamma_1-\gamma_2$ (or $e-\gamma$, $e-\beta$) rays. Thanks to the angular momentum conservation, I , there is a correlation between two emission directions k_1 and k_2 . As all spins are randomly distributed throughout space and the radiation is isotropic, therefore one may need to create special conditions to obtain anisotropic γ angular distribution. In order obtain this anisotropic distribution, $2I + 1$ degenerate m sub-levels cannot be simply equally populated, thus the state when emission occurs has to be either polarised or aligned. The nuclei are considered to be polarised when the density of states $\rho(m)$ is dependent on m , while $\rho(m) \neq \rho(-m)$. This aligned state is achieved, when the density of states depends only on

their absolute values $\rho(m) = \rho(-m) \neq \rho(m')$ [67]. Generally speaking, there are two ways how to orientate nuclei. One way is to apply a strong magnetic field or decrease temperature significantly. Another way (case of angular correlations) is to pick only those nuclei, whose spins happen to lie in a preferred direction.

Let us review a situation where a nucleus in an initial state $|I_i, \pi_i, m_i\rangle$ decays via a γ_1 - γ_2 cascade (see Figure 2.5) where the spin is spontaneously oriented or randomly distributed (i.e., occupation of the different m_i states is homogeneous) [68].

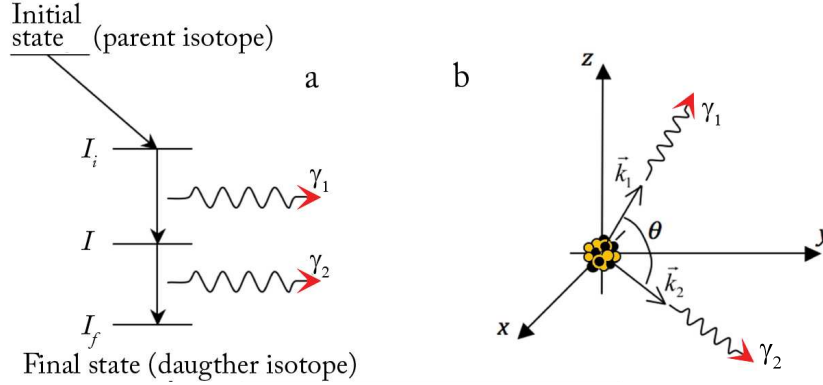


FIGURE 2.5: A γ - γ nuclear cascade.

The observation of γ_1 in a fixed direction \mathbf{k}_1 (can be picked as the Z-axis) determines a group of nuclei in the intermediate state whose magnetic sub-levels m are no longer equally populated. This is a consequence of the angular momentum conservation ($\mathbf{I}_i = \mathbf{I} + \mathbf{L}$, where \mathbf{I}_i and \mathbf{I} are angular momentum of initial and intermediate states and \mathbf{L} stands for the photon angular momentum) and angular distribution of the electromagnetic radiation, with respect to its angular momentum \mathbf{L} . Thanks to the alignment of the intermediate state the emission pattern of γ_2 is anisotropic and demonstrates an angular correlation with respect to the observation direction of the γ_1 . There is a probability $W(\theta)$ of finding γ_2 in a certain direction, \mathbf{k}_2 at angle θ with respect to \mathbf{k}_1 and in coincidence with γ_1 can be expressed as follows:

$$W(\mathbf{k}_1, \mathbf{k}_2) = W(\theta) = \sum_{k=0}^{k=k_{max}} A_k(\gamma_1) A_k(\gamma_2) P_k(\cos(\theta)), \quad (2.13)$$

where due to the parity conservation of the electromagnetic radiation, the sum runs over for the even values of k . In this case, k_{max} is governed by the smallest of $2I$, where $L_1 + L'_1$ and $L_2 + L'_2$ where $L'_{x,x}$ stand for multipolarities of transitions. Anisotropy terms $A_k(\gamma_1)$ and $A_k(\gamma_2)$ characterise the deviation of the coincidence probability from the isotropic case where $W(\theta) = 1$. At this point $A_k(\gamma_1)$ is dependent only on the first transition, whilst $A_k(\gamma_2)$ only on second. In other words, they rely on the correspondent angular momentum of the involved levels and on the type and multipolarity of emitted radiation. The last components are the Legendre polynomials P_k , which are describing the spatial angular distributions of the emitted particles. Experimentally, this can be done by placing two detectors where one is fixed and the other is not (the probability of emission of two successive gamma rays depends on a cascade of their relative emission angle). Equation (2.13) is only applicable when a nucleus is free from any extra nuclear fields.

When a nucleus is under influence of the extra-nuclear fields, due to the external charges density and polarisation distributions, e.g., in solid, it results in an interaction between them and the nuclear quadrupole and/or magnetic dipole moment of a nucleus. When it happens, the angular correlation function becomes time dependent or perturbed. The interaction of EFG and the nuclear quadrupole moment results in the energy splitting of the nuclear magnetic sublevels. In the middle of a γ_1 - γ_2 cascade emission, when a nucleus is at the intermediate state it is exposed to a hyperfine interaction that modifies the occupation of different magnetic sublevels ($m - m'$ transitions) and eventually, the emission probability of γ_2 in a certain direction turns time dependent.

Since in the current approximation we no longer consider the free atom, the perturbation has to be added into the angular correlation, therefore equation (2.13) has to be extended accordingly to the changes in the occupation of the sublevel during γ_1 - γ_2 elapsed time. Therefore, within the density matrix formalism, the density operator $\hat{\rho}(\mathbf{k}_1)$ describes the nuclear system after the emission of the first radiation ($t = 0$) changes in accordance with the the Liouville-von Neumann equation:

$$\frac{d\hat{\rho}(\mathbf{k}_1, t)}{dt} = -\frac{i}{\hbar}[\hat{H}, \hat{\rho}(\mathbf{k}_1, t)], \quad (2.14)$$

where \hat{H} stands for the extranuclear fields (if any is present). For a static \hat{H} , the density operator $\hat{\rho}(\mathbf{k}_1)$ is expressed as:

$$\hat{\rho}(\mathbf{k}_1, t) = \hat{\Lambda}(t)\hat{\rho}(\mathbf{k}_1)\hat{\Lambda}^\dagger(t) \quad (2.15)$$

here, a time-evolution operator $\hat{\Lambda}(t)$ describes how the perturbation affects the intermediate state can be describe as follows:

$$\hat{\Lambda}(t) = e^{-\frac{i}{\hbar}\hat{H}t}. \quad (2.16)$$

Then the derived angular correlation function $W(\mathbf{k}_1, \mathbf{k}_2, t)$ becomes after the determination of matrix elements [67]:

$$W(\mathbf{k}_1, \mathbf{k}_2, t) = \sum_{k_1, k_2, N_1, N_2} A_k(\gamma_1)A_k(\gamma_2)G_{k_1 k_2}^{N_1 N_2} \frac{Y_{k_1}^{N_1}(\theta_1, \phi_1)Y_{k_2}^{N_2}(\theta_2, \phi_2)}{\sqrt{(2k_1 + 1)(2k_2 + 1)}}, \quad (2.17)$$

where $Y_{k_i}^{N_i}$ are spherical harmonics with angles θ_i, ϕ_i of spherical coordinates for the emission directions \mathbf{k} , and $G_{k_1 k_2}^{N_1 N_2}$ is known as the perturbation function and describes the effects of external perturbation on the probe. The perturbation function is expressed as:

$$G_{k_1 k_2}^{N_1 N_2} = \sum_{m_a m_b} (-1)^{2I+m_a+m_b} \sqrt{(2k_1 + 1)(2k_2 + 1)} \langle m_b | \hat{\Lambda}(t) | m_a \rangle \cdot \langle m'_b | \hat{\Lambda}(t) | m'_a \rangle^* \begin{pmatrix} I & I & k_1 \\ m'_a & -m_a & N_1 \end{pmatrix} \begin{pmatrix} I & I & k_2 \\ m'_b & -m_b & N_2 \end{pmatrix}, \quad (2.18)$$

in this case $m_{a,b}$ are the quantum numbers of the intermediate state.

As the perturbed angular correlation function depends heavily on the crystalline nature of the sample, the function becomes fairly simplified when one has a polycrystalline sample.

Since, the angular correlation function in this case is obtained by averaging is averaged the angular correlation over all possible orientations of EFG and only the relative angle between two field direction matters. Furthermore, if the interaction hamiltonian is diagonal and static (for example, case of axially symmetric quadrupole interactions) evolution operator in the matrix can be set specifically that reduces the angular correlation function to [61]:

$$W(\theta, t) = \sum_{k=0}^{k=k_{max}} A_k(\gamma_1)A_k(\gamma_2)G_{kk}(t)P_k(\cos(\theta)). \quad (2.19)$$

Using ΔE_Q from equation (2.8) the perturbation factor shown in (2.6) for the case of static axial symmetric electric quadrupole interaction in a polycrystalline sample becomes:

$$G_{kk}(t) = \sum_{n=0}^{n_{max}} s_{kn} \cos(n\omega_0 t), \quad (2.20)$$

where frequency (or perturbation) amplitudes are S_{kn} , $n = |m^2 - m'^2|/2$ for I half-integer and $n = |m^2 - m'^2|$ for I integer, as the transition frequencies are normalised to the spin of an intermediate state. The current explanation of the quadrupole interaction in a polycrystalline sample is only applicable when $\eta = 0$. However, in the case of electric field gradient without axial symmetry ($\eta > 0$) the Hamiltonian of the interaction has to be further diagonalised for each η because the angular momentum operators mediate transitions between different m states. Regardless, whether one has a polycrystalline or single crystalline sample when $\eta > 0$ the frequencies ω_{0n} are not affected, however amplitudes are S_{2n} . The Hamiltonian of the interaction is also now no longer applicable because the angles, which γ_1 and γ_2 form with the direction of the V_{zz} component, have to be taken into account, and $W(\theta, t)$ has to be calculated separately for each detector arrangement.

2.2.1.1 PAC-data Collection and Analysis

In order to find the perturbation factor $G_{kk}(t)$, which includes all information on the hyperfine fields, one needs to experimentally measure the coincidences N , as a function of time between the emission of two rays at a set detector angle. An experimental PAC spectrometer usually consists of 4 or 6 detectors, which are geometrically aligned among each other with 90° , 180° or θ_i . During a measurement if a γ -ray with a pre-set energy is detected then a clock starts. Later on, after a certain time another γ -ray reaches on of the other detectors. In case when the second γ -ray possesses the expected energy the clock stops, and the event is saved in the array of coincidences.

Once the twelve (or thirty) time spectra are collected for all possible combinations of the four (six) detectors, then after the background subtraction, correction and normalisation of statistics of all coincidence rate, from detector pairs at 90° , 180° with different efficiencies, $N(\theta, t)$ it becomes possible to calculate the PAC time spectrum $R(t)$ given as follows [69]:

$$R_{exp}(t) = 2 \frac{N(180^\circ, t) - N(90^\circ, t)}{N(180^\circ, t) + 2N(90^\circ, t)}. \quad (2.21)$$

For a polycrystalline sample one has $R(t) \approx A_{22} \cdot G(t)$ [67], significantly simplified previous equation.

The first steps in experimental data analysis start from a theoretical fit. The method relies on the reconstruction of a theoretical function, $R_{fit}(t)$. Here, the perturbation function in

Equation (2.20) calculated considering the full hamiltonian for the nuclear quadrupole (in this case) hyperfine interaction.

It is worth to mention, that frequently in PAC results the hyperfine field of the nuclear interaction is different for all probes. Therefore, one can measure only a distribution of frequencies near a certain average value. Such behaviour could stem from small differences in the local environment due to the lattice defects, inhomogeneity of neighbours' atoms near the probes. Due to these hyperfine field distributions, there is an attenuation of the time spectra [70]. When there is a fine density of such defects, these distributions can be described by Lorentzian or Gaussian function in the frequency domain. For the Gaussian hyperfine fields distribution, the attenuation function can be presented as:

$$D_{gauss}(F_{fwhm}, t) = e^{-\frac{F_{fwhm}^2}{16ln2}t^2}, \quad (2.22)$$

where the standard deviation σ of the attenuation function is $\sigma = F_{fwhm}/\sqrt{8ln2}$ and F_{fwhm} is the distribution full width at half maximum. In the literature, one normally shows a fraction of the fundamental frequency $\delta = \sigma/\omega_0$.

In case of the Lorentzian hyperfine field distribution, one has attenuation expressed as:

$$D_{lorentz}(F_{fwhm}, t) = e^{-\frac{F_{fwhm}}{2}t}, \quad (2.23)$$

here σ is defined as $\sigma = F_{fwhm}/2$.

Another source of attenuation (damping) is due to the finite time resolution of a particular PAC set-up τ_s . This matters when $\omega_n\tau_s > 2\pi$ and a correction to the s_{kn} is necessary. This correction is considered by multiplying each term of $G_{kk}(t)$ by a function of the observed frequencies $P(F'_{fwhm}, \omega_n)$. Time resolution then is also assumed to follow the Gaussian distribution:

$$P(F'_{fwhm}, \omega_n) = e^{-\frac{F'_{fwhm}{}^2}{16ln2}\omega_n^2} = e^{-\frac{1}{2}\tau_s^2\omega_n^2} \quad (2.24)$$

Furthermore, possible distributions of the EFG are considered multiplying $G_{kk}(t)$ by the distribution of Fourier transformation $D(F_{fwhm}, t)$ ¹:

$$G'_{kk}(t) = \sum_n s_{kn} \cos(\omega_n t) D(F_{fwhm}, t) P(F'_{fwhm}, \omega_n). \quad (2.25)$$

After this, corresponding angular functions W'^t are calculated for various θ (90°, 180°):

$$R_{fit}(t) = 2 \frac{W'(180^\circ, t) - W'(90^\circ, t)}{W'(180^\circ, t) + 2W'(90^\circ, t)}. \quad (2.26)$$

As generally the distinct fractions of probes are subjected to certain electric field gradient then one may have the fit function expressed as follows:

$$W'(\theta, t) = \sum_i f_i W'_i(\theta, t), \quad (2.27)$$

here f_i (when $\sum f_i = 1$) stands for the relative intensity of each perturbed angular correlation function $W'_i(\theta, t)$.

¹Depends on the type of a hyperfine field distribution (Lorentzian or Gaussian)

Software, which calculates the eigenvalues and eigenstates of the hamiltonian used for evaluation of spectra in the current dissertation are NIGHTMARE and GFIT. Both programmes are based on NNFIT [71, 72].

2.2.1.2 Temperature Dependence of the EFG

Influence of the temperature on the trends of the electric field gradient in solids has been significantly studied. Obtained results show that there exist certain trends, amongst which a decline of V_{zz} with temperature rising is without doubt the most common, although there are reports when it happens vice versa [73]. It is assumed that there are several contributions to the V_{zz} temperature dependence and their significance is mainly dependent on the particular system under the scope, hence no generalised theory exist.

First important enlightening on the matter was brought by H.Bayer [74] and later on generalised [75, 76], where it was suggested that electric field gradient was proportional to the lattice contribution, and all changes of V_{zz} were originating from both the lattice parameter thermal expansion and phonons. Accordingly, for the case of ionic crystal influence of the thermal expansion on EFG can be expressed as follows:

$$\frac{1}{V_{zz}} \left(\frac{\partial V_{zz}}{\partial T} \right)_P = \frac{1}{V_{zz}} \left(\frac{\partial V_{zz}}{\partial V} \right) \left(\frac{\partial V}{\partial T} \right)_P = -\frac{1}{V_{zz}} \left(\frac{\partial V}{\partial T} \right)_P, \quad (2.28)$$

where $V_{zz} \propto V^{-1}$, for inter-atomic distances influence V_{zz} as $1/r^3$. Based on that, with a temperature decrease, V_{zz} is going to grow (positive thermal expansion). Regardless, thermal extension is not much of influence in solids near 300 K and is not often responsible for changes in V_{zz} [77]. At high elevated temperatures though, it can be used to explain changes happening to V_{zz} [78, 79].

Phonons' contribution, on the other hand, causes time-dependent fluctuation of the electric field with higher frequencies than such of the quadrupole frequency (in order of 10^4 higher), thus averaging the EFG of measurements. If one takes into account harmonic vibrations around the atom's equilibrium positions and to equal the mean energy of the standard harmonic oscillator to the mean energy of the Planck's oscillator (if $\hbar\omega/k_B T \ll 1$) it is possible to come up with an equation for $\langle V_{zz} \rangle$:

$$\langle V_{zz} \rangle = V_{zz}^{eq} \left(1 - \frac{3k_B T}{2\Theta\omega^2} \right), \quad (2.29)$$

where V_{zz}^{eq} is the EFG principal component when no fluctuations, ω is the angular frequency of the normal mode, Θ is inertia moment of a rotation mode and k_B is the Boltzmann constant. In this case, one may expect a linear increase of the EFG with a temperature decrease (when $k_B T \gg \hbar\omega$). The aforementioned theory by H. Bayer [74] serves quite well for a temperature dependence in ionic lattices, falling short for the metals. Generally speaking, it can be evaluated in a way that the electronic fluid was not included. In metals, the electronic contribution to the EFG temperature dependence is very important for electrons mediate the effect of lattice vibrations on the EFG. Experimentally, a dependence for non-cubic metals has been proposed, however it received no theoretical explanation [80]. As the current work does not include any experiments performed on metals, hypothesis on the EFG behaviour in metals can be found elsewhere [81].

Regarding the metal oxides, several of them, including TiO_2 rutile tend to show a peculiar behaviour in terms of the EFG [82, 83]. However, in most of the cases with an increase in temperature, a metal oxide shows a decrease of the EFG principal component [84, 85].

2.3 Mössbauer Spectroscopy

The phenomenon of the recoilless emission and the recoilless resonant absorption of γ -rays by the nucleus is known as the Mössbauer effect [86]. Utilisation of this effect made it possible to probe the local environment of certain atoms (probes) in various solids. Results are obtained in form of three hyperfine interactions, namely: the electric monopole, electric quadrupole and magnetic dipole interactions. Based on these parameters one can get the atomic scale information on the electronic, magnetic structure, geometry of studied materials [62, 87]

2.3.1 Mössbauer Effect & Recoil Free-fraction

In case when a γ -ray is emitted from a free excited nucleus with mass M , which is at rest before the emission, a recoil is bestowed to the nucleus what causes a movement of the nucleus in the opposite direction of the emission. As a consequence the carried energy by the γ -ray equals to the transition energy E_0 minus the energy of the recoil E_R . The caused recoil creates a displacement of the emission line from the position of E_0 by amount of energy taken by recoil. Therefore it prevents subsequent resonant absorption of the γ -ray. However, if the excited nucleus is located within a solid matrix, the recoil is transferred through a linear momentum to the solid as a whole, leading to negligible recoil losses. Due to much higher mass of the solid in comparison to a free nucleus it results in a possible recoilless emission of the γ -photon. If there is no energy losses for the transition from the excited to the ground state it makes possible the resonant emission and absorption by another not free nucleus of the same kind. Sometimes, the nucleus can get de-excited to the ground state by emission of fluorescent photons or conversion electrons.

The recoil-free fraction of en emitted γ -quanta f can be expressed as follows [62]:

$$f = \exp\left(-\frac{E_\gamma^2}{\hbar^2 c^2} \langle x^2 \rangle\right), \quad (2.30)$$

here $\langle x^2 \rangle$ stands for the mean square vibrational amplitude of the emitter in the direction of radiation. Higher the temperature is, higher the mean displacement of $\langle x^2 \rangle$ becomes, inevitably decreasing the recoil-free fraction. Evaluation of $\langle x^2 \rangle$ requires a model, describing the vibrational spectrum (usually the Debye model is employed). Due to a bit stronger interactions of Fe^{3+} with ligands the Debye temperature is higher, than it happens to be with Fe^{2+} (when sites are close to be the same). A substitutional ^{57}Fe bears higher Debye temperature (in contrast to interstitial) since it is firmer bounded to the lattice, the feature is widely used to say whether one deals with ^{57}Fe being at the interstitial or substitutional environment.

2.3.2 Mössbauer Spectra Collection and Evaluation

Regardless of Mössbauer experiment type or arrangement, spectra are recorded by measuring total amount of counts during an experiment as a function of the relative velocity

between the absorber and source. If the absorber and source move toward each other then the velocity is positive. If there is a defined relative velocity of the source and reference v , then the out-coming γ -quantum is going to have energy defined as follows:

$$\Delta E = E_0 \frac{v}{c} \cos\theta, \quad (2.31)$$

where θ is a small angle between the γ -ray direction and the relative velocity and c is speed of light, assuming $E_\gamma \approx E_0$ is the transition energy at rest. Thanks to the Doppler effect an emitted γ -quanta bear altered energy. For ^{57}Fe Mössbauer spectroscopy a change in the velocity v for 1 mm s^{-1} equals to $\Delta E \sim 4.81 \times 10^{-8} \text{ eV}$. The high spectral resolution originates from the half-life of the Mössbauer isotope (for ^{57}Fe , $\Gamma_{fwhm} = 4.69 \times 10^{-9} \text{ eV}$).

The simplest way to describe the intensity profile $I(E)_n$ as a function of energy can be done by Lorentzian profile Γ_{fwhm} excluding the recoil as [62]:

$$I(E) \propto \frac{\Gamma_{fwhm}/2\pi}{(E - E_0)^2 + (\Gamma_{fwhm}/2)^2}. \quad (2.32)$$

An experimentally obtained spectrum's Γ_{fwhm} is generally twice as wide as the natural line-width $\approx 0.194 \text{ mm/s}$ for the emission line overlaps the absorption line. It is not feasible under normal circumstances to observe such a narrow line due to imperfections in the experimental set-ups and inhomogeneity of Fe probes etc.

In the current work all Mössbauer spectra were analysed with a spreadsheet-based software VINDA [88], which is based on Visual Basic for Application framework. The tool allows to fit simultaneously several spectra where every spectrum is a separate spreadsheet. The best fit value is achieved with minimising of χ^2 :

$$\chi^2 = \sum_{i=1}^N \left(\frac{d_i - m_i}{\sigma_i} \right)^2, \quad (2.33)$$

where N is the quantity of channels, d_i and m_i are the experimental and model values and $\sigma_i = \sqrt{d_i}$ is the standard deviation. Additional data was obtained on a simultaneous routine in HAPPY SLOTH environment [89].

The current chapter provides a brief description of the synthesis methods employed for the samples production. This is followed by an overview of the experimental techniques of nuclear solid state methods, which have been used to characterise samples during this work. Additionally, a state of the emission Mössbauer spectroscopy at *Isotope mass Separator On-Line facility (ISOLDE)*, CERN, prior the developments described in Chapter 5 is shown. As the majority of the local probe methods are based on the use of radioactive isotopes, the radioactive beam production is presented along with the implantation routine of isotopes used in this study is explained. As most of the experimental results are complemented with *ab-initio* calculations a brief description is also provided.

3.1 Sample Preparation

Samples used in this work were obtained from two sources. Thin films on Si substrates, which were used during the current studies were produced at Chair Materials for Electrical Engineering and Electronics, Institute of Materials Science and Engineering, Institute of Micro and Nanotechnologies MacroNano, TU Ilmenau, Germany. On the other hand, monocrystalline samples of rutile used in PAC studies were purchased from Goodfellow. Used thin films of TiO_2 were deposited onto Si and quartz substrates by means of radio frequency sputtering (LA 440S by VON ARDENNE) utilising a ceramic TiO_2 target (99.9% FHR Anlagenbau, Germany). During the process, the sputtering power was kept at 200-210 W and the Ar flux was fixed at 80 sccm. The thickness of thin films was controlled to be in order of 100 and 150-500 nm (for anatase and rutile, respectively) with an ellipsometer (Sentech SE 801) and the crystal structure was determined by virtue of *Grazing Incidence X-ray Diffraction (GIXRD)*. Prior to hydrogenation, the samples were generally annealed at 773 K (813 K) (or 1173 K for rutile) for 3-4 hours to ensure their crystallisation. Thereafter, the samples were treated in a chamber for plasma-enhanced hydrogenation treatment, where an inductively coupled plasma instrument (Plasma Lab 100 ICP-CVD, Oxford Instruments) was employed. It is worth mentioning that before hydrogenation, so-called preconditioning procedure was applied. During the preconditioning 500 nm of SiO_2 is deposited on the chamber walls with pressure of 38.5 sccm for N_2 , 11.5 sccm for N_2O

and 5 sccm for SiH₄ at 500 W.

Treatment in hydrogen plasma was performed for 30 minutes within a range of temperatures, starting from RT and going up to 663 K. The ICP power was varied between 2 and 3 kW, the chamber pressure at 3.5 Pa, and the H₂ flow rate was kept at 50 sccm.

3.1.1 Charge Density Modelling with *Ab-initio* Calculations

Presently, the most used way of solving the quantum-mechanical problem in solids is *Density Functional Theory* (DFT) based calculations, where one varies the electronic density. The last can be achieved on a basis of Hohenberg-Kohn theorems, which reflect that the electronic density used in the universal functional minimises an expression applied for the total energy in the case when the electronic density is comparable to the ground-state electronic density, and it corresponds uniquely to the ground-state wave function [90]. Applicable way to determine the electronic density is to solve the Kohn-Sham equations [91]:

$$\left(-\frac{\hbar^2}{2m}\nabla^2 + V_s(\mathbf{r})\right)\phi_i(\mathbf{r}) = \epsilon_i\phi_i(\mathbf{r}), \quad (3.1)$$

here V_s stands for the effective potential of solving a single particle problem:

$$V_s = V_{ext} + \int \frac{n(\mathbf{r}')}{|\mathbf{r} - \mathbf{r}'|} d\mathbf{r}' + V_{xc}(n(\mathbf{r})), \quad (3.2)$$

V_{ext} is the external potential which also features the nuclei due to using of the Born-Oppenheimer approximation. V_{xc} is the exchange-correlation potential and represents all the many-body effects which can not be precisely calculated with the current method. Starting with an initial density, the potential V_s is constructed to find the orbitals ϕ_i , which are further used to determine a new density via:

$$n(\mathbf{r}) = \sum_i^N |\phi_i|^2 \quad (3.3)$$

In order to converge the density, one has to iterate the procedure. Presuming complete knowledge of all the functionals used in the equations, it precisely corresponds to the ground-state density of the many-body system. Nevertheless, when it comes to practice V_{xc} , the exchange-correlation potential remains undetermined, thus one needs to approximate it. Basic class of this approximation is *Local-Density Approximation* (LDA). LDA depends solely on the values of the electronic density at each point in space, where V_{xc} corresponds to the exchange-correlation potential of an electron gas with the homogeneous density which equals to the local density at that point. LDA approximation is often used, however since it approximates the energy of the true density by the energy of a local constant density it turns out to be meagre in scenarios where the density undergoes rapid changes.

An enhancement could be made by considering the gradient of the electron density, the so-called *Generalised Gradient Approximation* (GGA). In the case of GGA generalisation, it is imposing certain conditions which gradients are to follow. Both LDA and GGA can be generalised to take spin into consideration, although both cannot describe well strongly-correlated-systems. One can find workarounds by using hybrid functionals.

Nowadays, there are numerous implementations to solve the Kohn-Sham equations. Nonetheless, the major differences are expressed in various ways to describe ϕ_i with/out conveying the pseudopotentials. In the current dissertation several methods have been applied.

Theoretical *Perdew-Burke-Ernzerhof* parametrisation of the GGA (PBE) functional has been employed with the linearised augmented plane wave + local orbitals method (L)/APW+lo in WIEN2K environment [92], the *Projector Augmented-Wave method* (PAW) and in several cases additionally DFT+U was used to treat the strong on-site Coulomb interaction of localised electrons in the VASP code [93].

A representation of a wave function in WIEN2K is based on the augmented plane wave (APW) method. It assumes that the unit cell is divided in 2 regions: spheres at the atomic nuclear proposition (muffin tin) and the remnants as interstitial space. Descriptions of the Kohn-Sham functions in both are different. In muffin tin spheres, atomic-like functions are employed in a way $\sum_{lm} A_{lm}^K u_l(r', \epsilon) Y_{lm}(\hat{r}')$, where $Y_{lm}(\hat{r}')$ stands for spherical harmonics for orbital quantum number l and magnetic quantum number m , $u_l(r', \epsilon)$ is the solution of the radial Schödinger equation in a spherical potential for energy ϵ where coefficients A_{lm}^K are chosen in order to match functions at the sphere boundary with the plane waves. In the interstitial space, plane waves are used ($e^{iG \cdot r}$), where G is a vector in the reciprocal lattice. The (L)/APW+lo method employs linearisation energies and local orbitals to improve the accuracy and efficiency of the calculation in WIEN2K. Additional details can be found elsewhere [94]. The second environment used in the current work is VASP, with implantation of PAW [95]. The method uses no approximation of pseudopotentials, whilst the full wave-functions are also used.

As over the course of the current work various dopants have been introduced (Cd, Fe, H and various configurations of oxygen vacancies), conditions have been also varied. In the case of Ti:Fe doped with hydrogen, the *ab-initio* calculations have been based on the PAW method, which is based on $3 \times 3 \times 3$ k -points grids implemented in VASP environment. In the current calculation we made use of the PBE exchange-correlation functional to calculate the electric field gradients (mainly in VASP) as well as the isomer shifts (in WIEN2K). It is important to mention that the nuclear matter has very large stiffness, hence remains practically unperturbed by the electronic shells of the atom and its surrounding. Based on that, it is possible to approximate that the nuclear charge distribution is a homogeneously charged sphere, besides and one can presume that the electron density stays constant within such a sphere. Taking this into account one can come to the isomer shift expressed as follows:

$$\Delta E_{IS} = \alpha(\rho_a(0) - \rho_b(0)), \quad (3.4)$$

where $\rho_a(0)$ and $\rho_b(0)$ are electron charge densities at the nuclear site for the absorber and source, respectively and α is calibration constant $-0.21\alpha_0^{-3} \text{ mm s}^{-1}$ (where α_0 is Bohr ratio) [96]. Quadrupole splitting is calculated with equation (2.7).

Additional effort on predicting possible isomer shifts, besides the DFT calculations, was based on an empirical model for determination of Mössbauer isomer-shifts in ionic and covalent binary compounds. The model predicts room temperature isomer-shift values for Fe^{2+} in metal oxides. The empirical model relies mainly on the nearest-neighbour distances and Pauling electronegativity ($\Delta\chi_P < 2$) [97].

3.2 Beam Production and Nuclear Solid-State Methods

In this section information on the two methods is going to be provided, with high attention devoted to MS, as well as insight on a tracer diffusion experiments, including blueprints of the facility where the radioactive beams are produced.

Nowadays both PAC and MS experiments can be easily performed on a basis of a regular laboratory with only one remark — experiments are performed with the long-lived isotopes. For that one may only need a radioactive source, which commonly are ^{57}Co , $^{119\text{m}}\text{Sn}$ in Rh matrix for MS experiments, or $^{111}\text{InCl}_3$, which can be electrochemically deposited on samples of interest for PAC ($^{57}\text{CoCl}_3$ for MS experiments). However, that imposes several limitations such as: limited amount (or too high, depending on the aim) of isotopes, which are possible to introduce into samples, sometimes no nuclear reaction with appropriate cross section exists for the production. Therefore, on the basis of aforementioned information it is desirable to perform experiments in centralised facilities, regularly achieving production and *in-situ* delivery of a large panoply of short-lived isotopes/elements of interest. In this particular case, experiments have been carried out at ISOLDE (Isotope Separator On-Line-DEvice) facility, as part of PAC and Mössbauer collaborations at ISOLDE/CERN [98–100].

The blueprint of ISOLDE facility is demonstrated in Figure 3.1. The radioactive beam is produced when protons of high energy bombard a fixed target. The procedure commences with the protons production, which are later accelerated up to 50 MeV in a linear accelerator. Consecutively, the protons are introduced into the Proton Synchrotron Booster, which has four superimposed rings with radius of 25 m where the protons undergo acceleration up to 1.4 GeV. Afterwards, radioactive ions are produced utilising 1.4 GeV proton-induced nuclear spallation fragmentation and fission reactions in a UC_2 (MS experiments) or (molten Sn) target. During proton irradiation the target is kept approximately at 2300 K (depends on numerous factors including desired isotopes, age and so forth), for the facilitation of the new radioactive nuclei diffusion towards the target's surface. These radioactive elements are later ionised by one of the numerous ion sources (lasers are used for MS, while for PAC implantations VADIS or MK5 are engaged), then are accelerated by the extraction electrode to 30 - 60 kV and mass separated by the separator magnets. At ISOLDE there are two separator magnets: General Purpose Separator (GPS) and High Resolution Separator. The GPS separator allows the simultaneous extraction of three mass separated beams in two low mass (GLM) and high mass (GHM) beamlines and preferentially used by solid-state physics, biological and medical applications. Hence, once mass separated the ions are implanted into the material of interest [101, 102] at GLM beamline (where the collections for PAC measurements take place along with Mössbauer measurements). The lasers are used due to their element-specific selectivity and together with the isobar-specific selectivity of the separation magnet it becomes possible to suppress significant quantities of contaminants [103].

Figure 3.1 shows a picture of the experimental hall. GLM beamline location, where the newly developed eMIL spectrometer is going to be installed is highlighted.

3.2.1 TDPAC Spectroscopy at ISOLDE/CERN

Time Differential Perturbed Angular Correlations spectroscopy (generally and shortly designated as PAC) is one of most appealing and productive experimental methods for microscopic studies of solids. It deserves its special place due to several reasons: no Debye-Waller (while it takes place in Nuclear Magnetic Resonance and MS), no applied magnetic field is needed (unlike in Nuclear Magnetic Resonance), slightly more sensitive than MS, needs even diluter amount of radioactive probes. A detailed review on a contemporary PAC spectrometer can be found elsewhere [104, 105].

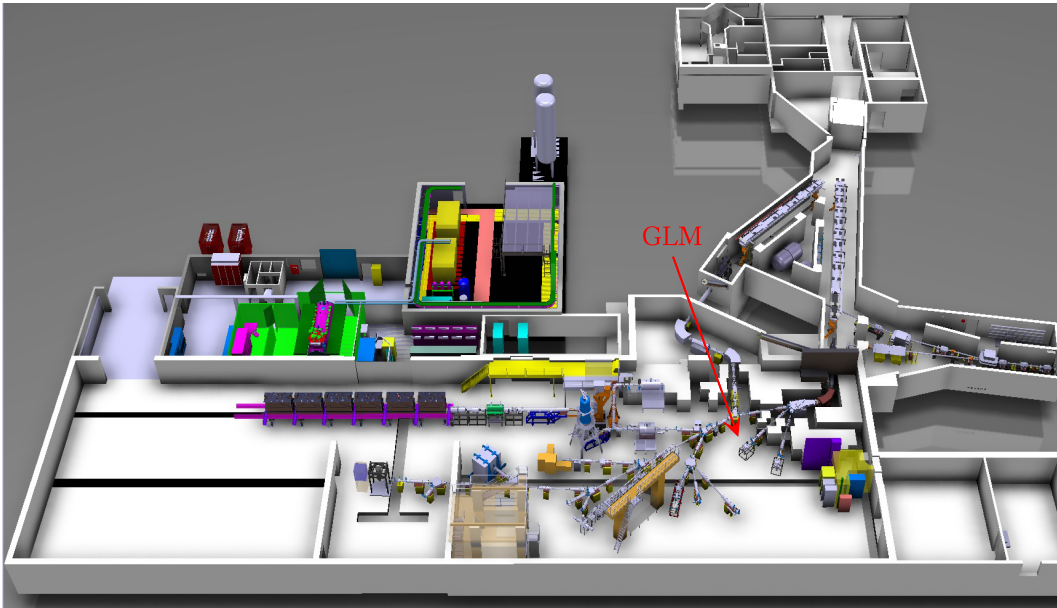


FIGURE 3.1: The ISOLDE hall. By courtesy of CERN.

In the current study the PAC measurements were performed utilising both analogues and digital slow-fast set-up equipped four/six detectors PAC spectrometers equipped with BaF_2 (with time-resolution 650 ps) and $\text{LaBr}_3:\text{Ce}$ (220 ps) scintillators, disposed in the 90° and 180° geometry [61]. Although, description of only an analogue det-up is going to be provided. Information about digital set-ups can be found elsewhere [106]. In a few words, a PAC spectrometer collects a time-dependent histogram of events where a photon γ_1 enters a scintillator and in a following time (t) later a second photon γ_2 enters another detector. Based on that, the positive signal originating from each detector, it becomes preamplified and is forwarded to an amplifier. Once a fraction of the signal is integrated, it is instantly sent to a single-channel analyser, which is pre-set to certain energies of expected $\gamma_1 - \gamma_2$. The single-channel analyser creates a positive gate signal ones a γ with selected energy (amplitude) comes. Additionally, single-channel analyser determines a combination of two detectors where γ came. In parallel to the positive signal, the negative signal is transformed into the constant fraction units to supply time indicators for start/halt signals. Then events are checked for coincidences. The coincidences coming from the single-channel analyser bearing data on energies (including start/halt signals) and data from the constant fraction (with exact timings when γ comes). Quality of determination of coincidences depends on comparisons of timestamps determined at different computers thus a common external clock is used. If these coincidences take place or when data overlaps, then one has new start/halt signals which now feature information upon their provenance from $\gamma_1\gamma_2$. In final steps these signals are forwarded to a time-amplitude converter, to create an analogue signal with amplitude proportional to the time difference between the arrival of the start and halt signals when data is digitised and sent to a multichannel analyser to record the histogram of counts/versus time, of each detector pair. Data stored in the multi-channel analyser is consequently sent to a computer. In the case when a four detectors PAC set-

up is used for collections one has 8 spectra coming from the 90° mounted detectors and 4 from 180° , this results in twelve spectra. As a result information on provenance, expressed as counts/versus time is obtained. A contemporary digital spectrometer [106] based on 6 LaBr₃:Ce scintillators is shown in Figure 3.2.



FIGURE 3.2: Photography of a digital 6-Detector $\gamma - \gamma$ PAC spectrometer. Additional furnace can be mounted in the centre of the detectors. By courtesy of M. Nagl.

Since the main idea of the current study was to collect information on the defect structure, performing experiments within temperature ranges as well as under various atmospheres (O_2 , H_2 , vacuum) were necessities. PAC technique was applied to study the EFG at an atomic level, specifically at the Ti sites. Most of elevated-temperatures studies were done in the 6 detectors arrangement. For the fulfilment of needs, a small tubular resistive furnace was used from room temperature up to 873 K. A typical scenario was based on several stages. Starting, one may need to implant an isotope of interest (at GLM) into a desired sample, with doses in order of 10^{11} at.cm⁻². The latter being followed by a rapid annealing, to reduce the damage caused by the implantation, this commonly includes 10 minutes of annealing (873 K, 15 minutes in the current case of TiO₂). The third stage was the process of measurements. PAC measurements were performed only for rutile TiO₂, Several attempts were applied to measure anatase, however the width of the frequency distribution was relatively large and it was not possible to improve it to the rutile's extend. As for ^{111m}Cd the flat response of the perturbation function and also the fast Fourier transformations without any lines indicated that there was no perturbation of ¹¹¹Cd in anatase.

The implantation profiles for the samples of interest can be determined by virtue of Stopping and Range of Ions in Matter (SRIM) software [107]. The values obtained for Cd implanted into rutile are in order of 15 nm while the straggling does not exceed 5 nm for implantations at 30 keV. Anatase being less-dense (3.9 versus 4.23 g/cm³) has been however studied at 40 keV, with the implantation range of 22-23 nm and straggle of 10 nm (Figure 3.3).

Raw data (R(t)) were additionally put through a compression method in R-studio (can

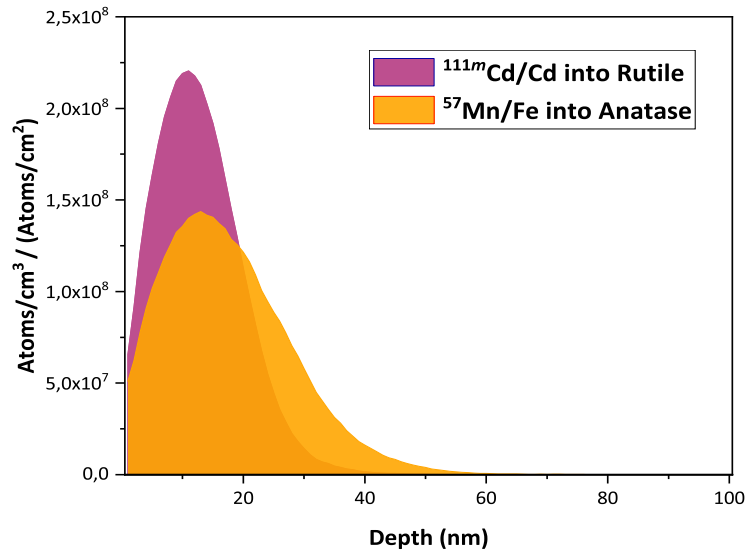


FIGURE 3.3: SRIM implantation profiles for rutile ($^{111m}\text{Cd}/\text{Cd}$, implanted at 30 keV) and anatase ($^{57}\text{Mn}/\text{Fe}$, implanted at 40 keV). Anatase is implanted at the incidence angle of 30° .

also be done by INTERLUDE software), in order to minimise amplitudes:

$$y_j \equiv y_{2k} = \frac{1}{4}(f_{k-1} + 2f_k + f_{k+1}), \quad j = 0, \dots, \quad N/2. \quad (3.5)$$

The method inevitably smooths and does not cause the phase shift [108]. So we might assume, for instance, $f_{-1} = f_0$ for the calculation of y_0 , this is also applied to the end of the data set.

3.2.2 Radiotracer Diffusion

Tracer diffusion is a method for direct studying self- and solute diffusion in solids. The macroscopic diffusion of one element that is available as a radioisotope featuring a suitable half-life is investigated with the radiotracer technique while keeping the sample chemistry pristine. Depending purely on the sectioning method a broad range of diffusion coefficients D can be covered by this approach. Based on facilities provided by ISOLDE, in the current study an ion-beam sputtering set-up called Online Diffusion Chamber (ODC) has been in use. ODC is a perfect tool for investigation of diffusion in both bulk and thin films and can determine diffusion coefficients with rates below 10 - 15 m^2/s . A schematic photography of ODC is shown in Figure 3.4.

Diffusion studies were based on the same implantation routine, which was applied to the ^{111m}Cd PAC studies. Approximately 4×10^{11} atoms of that ^{111m}Cd isotope were implanted. To be sure that nothing had an impact on the measurements the samples were annealed under the same conditions as the other samples with subsequent studies using an on-line diffusion chamber [109, 110]. Later on, the penetration profile was experimentally determined by virtue of ion beam sputtering using an Ar-ion beam. In order to measure

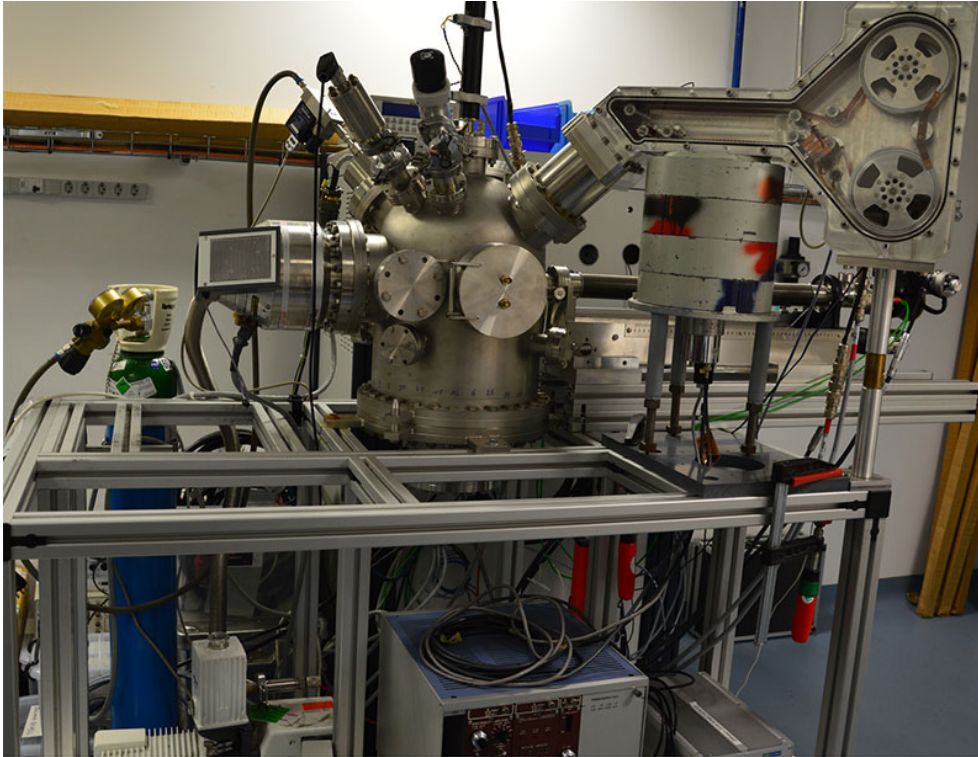


FIGURE 3.4: Diffusion chamber installed at ISOLDE. By courtesy of D. Gaertner.

the activity of each section an available NaJ γ -detector with a 16 K multi-channel analyser was employed to observe the 245 keV peak. The relative radioactivity of the Cd isotope was carefully determined by the background subtraction, including the Compton scatter, and the half-life correction. The penetration depth can be estimated by the mass difference of the sample before and after the whole experiment using a microbalance, and assuming a constant sputtering rate. During sputtering the beam current was recorded and proved to be constant within $\pm 5\%$.

3.2.3 Mössbauer Spectroscopy

Utilisation of the Mössbauer effect has made it possible to study the slightest changes in the energy levels of an atomic nucleus in response to its environment. Based on that, the method evolved into several miscellaneous approaches where all is based on the same phenomena but experiments differ, depending on the materials under investigation. In the current study, *Conversion Electron Mössbauer Spectroscopy* (CEMS) and *Emission Mössbauer Spectroscopy* (eMS) were used and described in details, while eMS is paid most attention and described in the separate section.

Amongst all MS variations CEMS is the most used technique. The approach originates from the end of the 60s, when it was demonstrated that emitted conversion electrons, following the nuclear resonant absorption, in the Mössbauer absorber could be used for characterisation of surface layers. As those emitted electrons have energies in order of several keV, thus their penetration depth is shallow and lies approximately within 60 nm. The spectra are

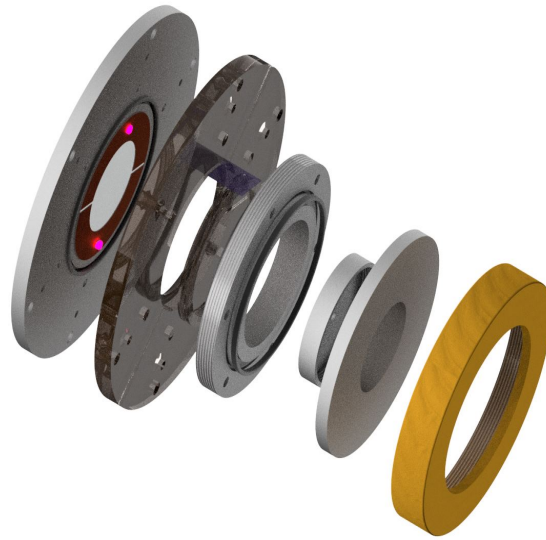


FIGURE 3.5: CEMS detector.

commonly collected with the integral technique (no energy resolution) and mainly based on use of flow type proportional counters. These counters are known for having high countrate. Incident radiation used in CEMS interacts with the absorber via several ways: 1) Compton and photoelectric effects 2) resonant absorption. After successful resonant absorption, the process resonant emission begins in the absorber and is carried out via emission of either a γ photon or an electron of the internal conversion. When the second scenario is ongoing, it leaves a hole in an inner shell (energy excess is compensated by an X-ray or Auger electron emission). Hence, there are 2 types of emitted electrons: first are from the de-excitations by the beam (Auger and internal conversion electrons), and secondary by the conventional interactions of photons emitted after resonant absorption [111]. One important thing to consider is called the radiation conversion coefficient, $\alpha = N_e/N_\gamma$, where N_e and N_γ stand for quantity of electrons and photons, respectively emitted from the absorber in a certain time. Moreover, each core level has its own distinct probability to take part in the internal conversion process. The biggest probability belongs to the K electrons (7.3 keV), although L (13.6 keV) and M (14.3 keV) core levels can have their contributions as well (see Figure 3.6) [112]. An electronic schematic description for MS set-ups is provided in section 3.3 having the only differences in detectors used.

In the current study, CEMS measurements were carried out with a standard ^{57}Co source in Rh matrix. Thin films of TiO_2 were treated with hydrogen plasma, and then changes taking place in the upper-surface layers were followed. Additionally, experiments performed with UV-light on TiO_2 took place, for that a special version of a CEMS detector had been constructed and shown in Figure 3.5. As one can see a common design was extended by placing a cooling Cu-based plate with soldered 365 and 355 nm LED diodes on it.

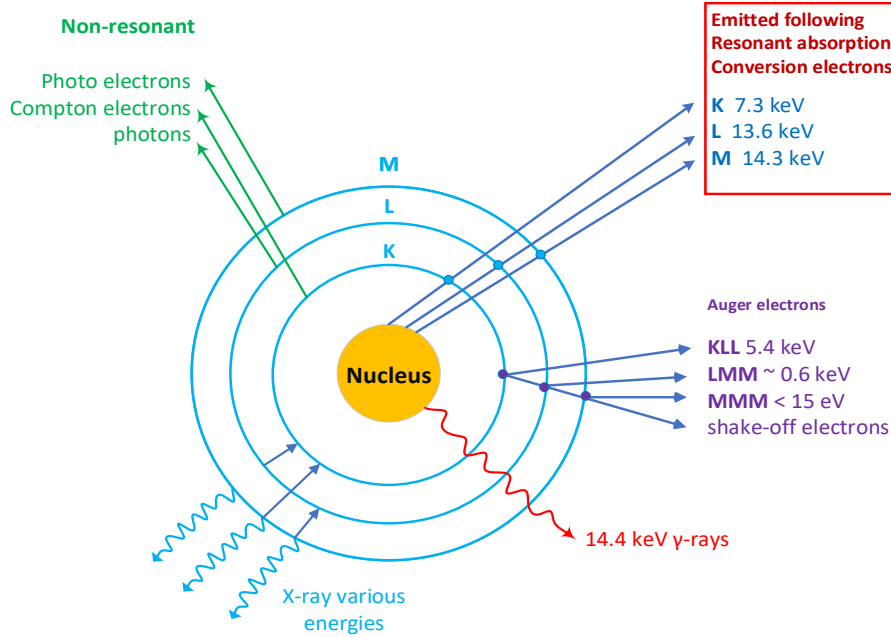


FIGURE 3.6: Deexcitation scheme of the ^{57}Fe absorber following resonant absorption of an incident γ -ray.

3.3 eMS at ISOLDE/CERN

Most of Mössbauer experiments were performed at ISOLDE/CERN in the eMS arrangement [100]. Used implantation chamber is operated in high vacuum conditions (down to 10^{-6} mbar) and is connected to the GLM beamline (see Figure 3.1). The chamber makes use of various sample holders, however in the current work a sample holder with 4 positions is employed for experiments under elevated temperatures (up to 750 K) allowing a serial measurements without the need of breaking the vacuum. At the initial stage a beam optimisation and calibration are done. For the first task, one needs to shoot the $^{39}\text{K}^*$ beam through an empty sample holder at a Faraday cup, in order to adjust the beams alignment and current. The alignment is performed when one has to compare the transmission between two points: prior the eMS chamber and in it.

Afterwards, the set-up is connected to the pumps and the beam-line vacuum line with soft bellows (to get rid from vibrations). At this stage the eMS chamber is connected to the GLM beam-line and stays this way until the end of a beamtime. In order to preserve the radioactive target one has to keep an eye on the vacuum's stability, since the chamber is continuously being opened and closed while a beamtime is ongoing. A picture of the implantation set-up is shown in Figure 3.7.

Due to a special experimental design all implantation routines are done at an incident angle of $\theta_i = 30^\circ$ and samples are measured at $\theta_m = 60^\circ$ in relation to the sample's surface normal \hat{n} . A Mössbauer drive with constant acceleration is located in front of the chamber at 90° relative to the beam direction. A Beryllium window is placed on chamber flange in between the chamber and the drive in order to remove electrons with high energy created

during β^- decay. The Be window does not impede and γ -rays can go through.

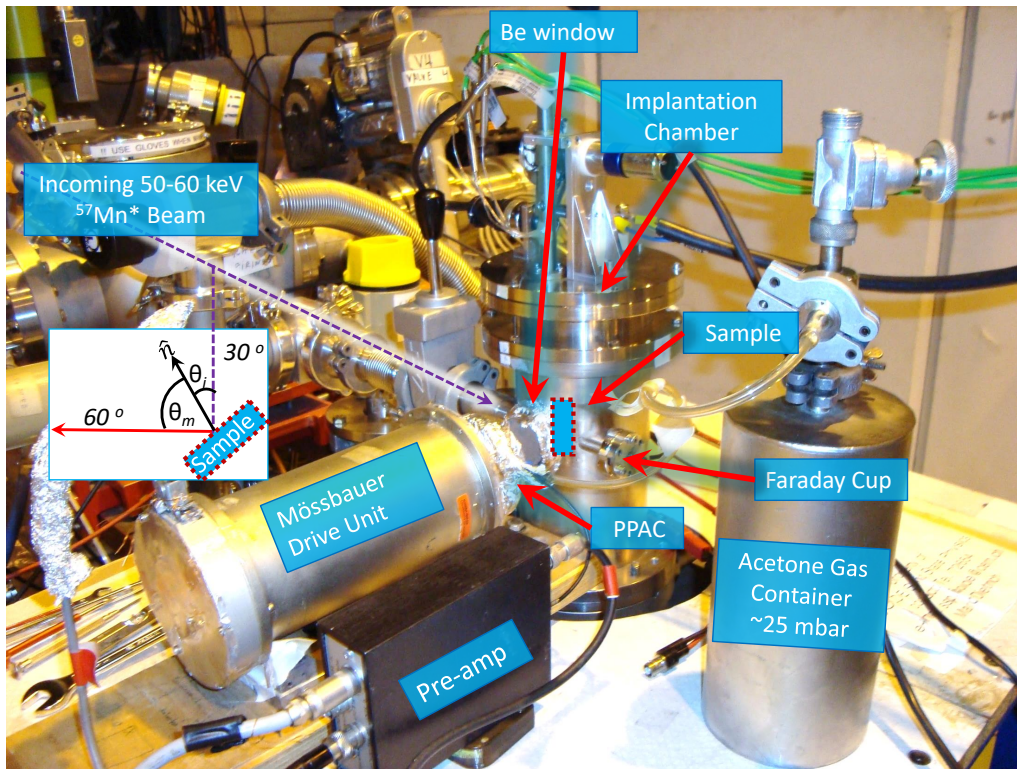


FIGURE 3.7: Photography of the current eMS experimental set-up at ISOLDE/CERN. Samples are mounted on various lids, so different experimental conditions can be created. Spectra are recorded using an avalanche parallel plate detector, which is filled with acetone vapours.

3.4 Sample Implantation

In order to carry out studies by means of PAC or eMS one needs to introduce required isotopes into the lattice of materials under study. Once they are introduced, they act as probes. Generally speaking, there are four ways to make it: 1) chemical deposition or evaporation with following heat treatment of a desired isotope; 2) doping during synthesis 3) via ion implantation and 4) activating in a neutron flux at a reactor. For PAC experiments ^{111m}Cd isotopes were used. Implantation of Cd took place at ISOLDE. The decay scheme of the ^{111m}Cd is shown in Figure 3.9 [104]. The isotope is not commercially available and can be produced only at accelerator facilities.

Cd probe decays with a half-life of 48.5 minutes via an isomeric transition emitting consecutively γ photons with 150.8 and 245.4 keV cascade (spin: $5/2^+$) into the ground state of ^{111}Cd . The nuclear quadrupole moment of the intermediate nuclear state relevant for the hyperfine interaction is $Q = 0.76(2)$ b [113]. Regarding the magnetic moment it is $0.766\mu_N$ and sufficient enough to provide sensitivity for magnetic fields. Intermediate

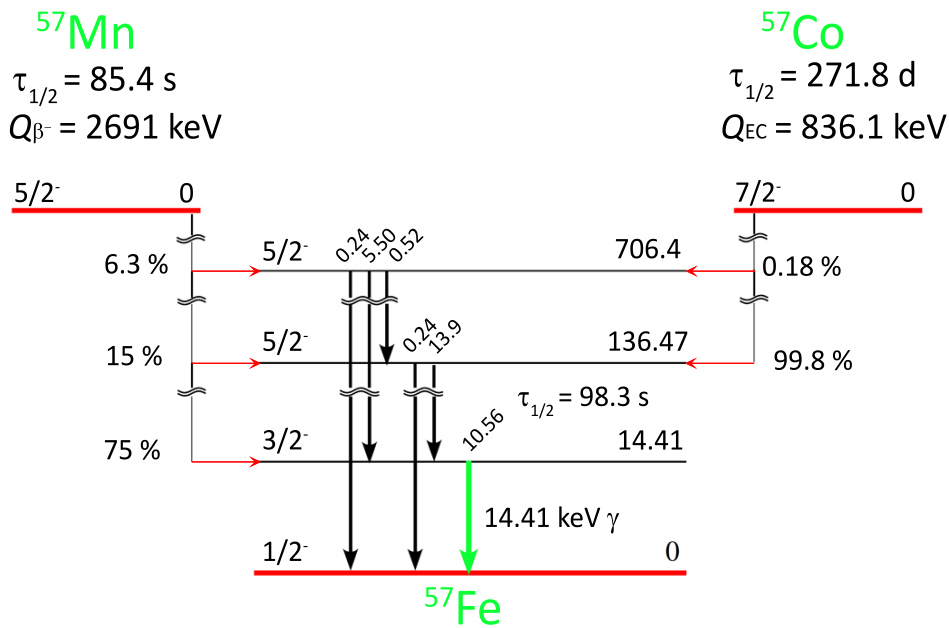


FIGURE 3.8: Decay schemes for ^{57}Mn and ^{57}Co nuclei, both decay into ^{57}Fe .

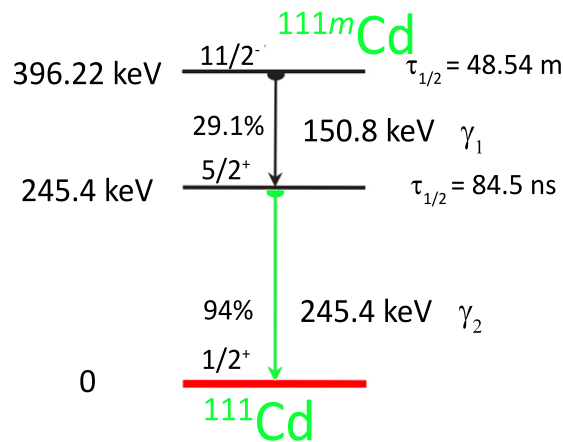


FIGURE 3.9: Decay scheme for ^{111m}Cd nucleus. Intermediate PAC probe state has energy $E = 245.4 \text{ keV}$ and probes the local environment during the life time of the intermediate state of 84.5 ns.

level half-life is 84.5 ns, which suits well for on-line measurements for it cannot out diffuse rapidly while being measured at elevated temperature since one measurement takes in order of 15 minutes. No after-effects (i.e., slow rearrangement of the probe and neighbourhood atom's to the final stable configuration) have been observed for this isotope. Implantations of ^{57}Mn for emission Mössbauer studies were performed at ISOLDE as well. ^{57}Mn is not an isotope used in Mössbauer studies, however it decays via $^{57}\text{Mn} \rightarrow ^{57}\text{Fe}$ β^- transition, thus populates the 14.4 keV ^{57}Fe Mössbauer state. The decay scheme is shown in Figure 3.8.

Concentration commonly do not exceed 10^{-3} at.%, therefore this method is well suitable for studies of truly dilute samples. Upon implantation the probe stops movement inside the material after 10-12 s. Hereafter, the implanted ^{57}Mn resides in the sample during its half-life, where possible annealing can take place. Relocation of the probe following the β^- decay may lead to the possible formation of interstitial Fe, in this case the bond-dissociation energy of the studied material should be less than the recoil energy (for the current decay is 40 eV) [38, 114]. The spectrum is recorded on the time scale of 98.3 s after the decay. For off-line experiments, a common source of ^{57}Co in Rh matrix was used.

The current chapter focuses on atomic scale studies of the EFG in two used TiO_2 polymorphs: rutile and anatase. The studies are complemented with DFT calculations and additional measurements such as GIXRD, tracer diffusion and XPS. The EFG is probed with $^{57}\text{Mn}/\text{Fe}$, ^{57}Fe and ^{111m}Cd isotopes in pristine and hydrogenated states. The majority of measurements is carried out as a temperature dependence, where the temperature range starts from RT and goes up to 700 K. Each separate experiment (section) contains the most important aspects from the literature relevant to the analysis as well as the experimental procedures are briefly described as the sections in this chapter are organised as self-containing articles.

4.1 Hyperfine Interactions and Diffusion at Cd in Rutile Single Crystals

In the current section, an investigation of the electronic and defect structure in (TiO_2) rutile single crystals by virtue of γ - γ TDPAC spectroscopy is presented. Studies were performed using ^{111m}Cd , implanted at ISOLDE/CERN complemented with diffusion studies and DFT calculations. Hyperfine field parameters were probed as a function of temperature between 298 K and 873 K. The results demonstrate that $^{111m}\text{Cd}/\text{Cd}$ implanted rutile has two local environments. The first environment is characterised with parameters attributed to Cd localised at the cationic site which goes relatively along with a specific case where a charged supercell with two additional electrons $\text{Cd}:\text{Ti}(2\bar{e})$ is in the scope. The origin of the second fraction could be rising from the subsurface regions, where according to a tracer diffusion study the major part of implant is bounded featuring different diffusion mechanisms. Performed *ab-initio* calculations suggest that the disruptive surface environment could contain apical or equatorial vacancies near the probe, inducing high EFGs for the second fraction. Current results seem to differ from those obtained before with different methods of probing (Ag/Cd and In/Cd). This subsection is based on Zyabkin *et al.* "Hyperfine Interactions and Diffusion of Cd in TiO_2 (rutile)", *J. Appl. Phys.* 126, 015102 (2019).

4.1.1 Overview

Titania has been studied extensively in the field of surface science, where TiO_2 is required to have high light absorption, good electron transport and large charge separation. However, the wide band-gap and low conductivity limit its technological application. There have been numerous studies devoted to doping, structural and surface modification aim at overcoming such limitations [115–117]. Recently, TiO_2 has been suggested as a promising semiconductor having high temperature ferromagnetic behaviour when doped with Cd, due to $p-d$ hybridisation between Cd and the nearest oxygen atom [118]. This is different from the room temperature ferromagnetism observed with Au/Fe doping in TiO_2 , where the phenomenon is often attributed to dopant-cluster formation [119]. Not long ago, hydrogen doping and controllable creation of oxygen vacancies (V_o) have bolstered photocatalytic activity, which significantly narrows the band-gap and adds mid-gap or tail states [40]. Regardless, even changes taking place in undoped samples remain ambiguous. The diversity is due to inner defects, which can vary based on the preparation method/subsequent annealing [120]. For instance, nonstoichiometric TiO_2 could be formed as $\text{Ti}_n\text{O}_{2n-1}$ Magnéli phases when samples feature oxygen deficiency. TDPAC stands as one of the few subtle methods allowing to probe the local lattice environment utilising diverse isotopes and is an excellent tool to study inner defects such as V_o . The required amount of implanted isotopes is small, which causes the least amount of impact on the local environment upon implantation damage recovery. However, even at low implantation fluences, one can affect the structure significantly, leading to new phase formations (such as Ti interstitials, V_o arrangements or Magnéli) [39]. The last can be formed as well in the case of oxygen insufficiency.

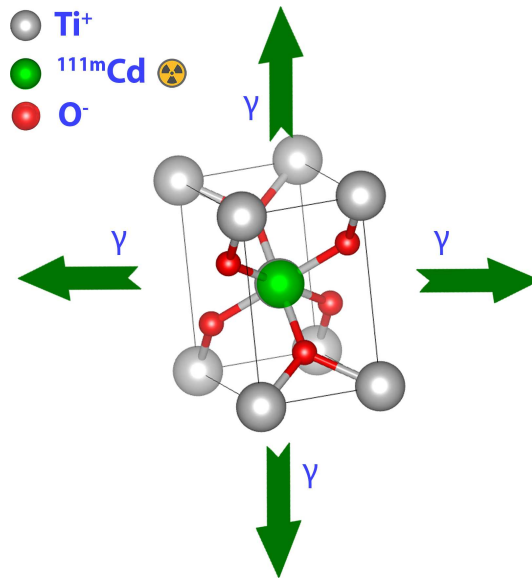


FIGURE 4.1: Rutile lattice with incorporated Cd isotope at the cationic site. Grey spheres are Ti ions, while red represent O anions

Depending on the subsequent annealing, most of these defects can be stamped out when the structure is fully annealed and implanted isotopes reside at the Ti site as shown in Figure 4.1. In spite of this, when annealing is performed in oxygen-lacking-atmosphere,

it could influence further development of those phases leading to the crystallographic shear formation as well as intensification of Cd diffusion [29, 30].

In spite of having studies on TiO_2 rutile ($P4_2/mnm$), where its hyperfine structure was investigated by means of TDPAC spectroscopy with heterogeneous parent isotopes, the results seem to be quite inconsistent. Wenzel *et al.* [121] carried out studies with $^{111}\text{In}/\text{Cd}$ within a temperature range on pristine powder, in both vacuum and O_2 . Studies in both atmospheres showed that Cd was surrounded with 2 local environments. Where the first had a well defined EFG with observable frequency $\nu_Q = 105$ MHz and asymmetry $\eta = 0.18$, second was characterised by $\nu_Q = 110$ MHz and $\eta = 0.35$, attributed to the substitutional site and defect complexes, respectively. Adams *et al.* [83] performed similar measurements with $^{111}\text{In}/\text{Cd}$ on polycrystalline samples. The authors noticed similar results at first; however, during temperature measurements, asymmetry behaved unexpectedly and vanished first at 750 K and then emerged and rose over the previous maximal value, in what followed a similar trend as in nuclear resonance observations, but not as in the case of other isotopes [82]. The results turned out impossible to explain solely on the basis of charge and ionic size changes. Das *et al.* [122] studied interactions in the bulk and nanoparticles of rutile with $^{111}\text{Ag}/\text{Cd}$. The obtained hyperfine results followed a phase-transition (anatase-rutile) depending on the time/temperature of annealing. The authors noticed a different impact of the same probe (^{111}Cd) originating from different parent isotopes (In/Cd and Ag/Cd) on V_{zz} , where the EFG in case of $^{111}\text{Ag}/\text{Cd}$ was in the order of $20.3 \cdot 10^{21} \text{ V} \cdot \text{m}^{-2}$ while $5.8 \cdot 10^{21} \text{ V} \cdot \text{m}^{-2}$ when In/Cd was employed. The observations were temporally associated to various after-effects originating from various decays [122]. That said, no sound explanation was suggested. Additionally, calculations partly supported with PAC measurements on single crystals with various orientations were published, where Cd was considered as an impurity. Qualitatively, influence of temperature was calculated by applying thermal expansion coefficients, and the findings suggested that the structural relaxations were changed with temperatures [123]. Schell *et al.* [124] observed various behaviours implanting simultaneously In and Cd isotopes in single crystals. The authors suggested that partial charge compensation could occur with $^{111m}\text{Cd}/\text{Cd}$, while it develops fully in the case of $^{111}\text{In}/\text{Cd}$.

In the aforementioned experiments, the comprehension was potentially affected by the after-effects. The decay causes an additional dynamic interaction, which has been well demonstrated recently [85]. Furthermore, most published results on TiO_2 rutile have shown dependencies of hyperfine parameters on measurement temperature as well as various electric field gradients originating from several parent isotopes [121]. The change is observed seemingly due to large relaxations which in turn affect the local environment [125]. Hence, depending on the parent isotope producing ^{111}Cd , the local environment is subject to change.

In the current section, the temperature dependence of $^{111m}\text{Cd}/\text{Cd}$ on TiO_2 rutile (single crystals) hyperfine parameters by means of ion implantation with subsequent TDPAC studies is presented. All experiments were performed at the on-line isotope mass separator ISOLDE/CERN [98]. The intermediate state has a lifetime $t_{1/2} = 85$ ns whilst the parent state decays with $t_{1/2} = 48.5$ minutes. The nuclear quadrupole moment of the intermediate nuclear state relevant for the hyperfine interaction is $Q = 0.76(2)$ b [113]. The experimental results are complemented with *ab-initio* calculations, diffusion studies and compared with previously published data.

4.1.2 Experimental

PAC experiments were carried out on a basis of coplanar 4-detector TDPAC spectrometer equipped with BaF₂ detectors placed around a tubular furnace at 90° geometry with a decent time resolution (650 ps). Commercially obtained rutile TiO₂ single crystalline samples with dimensions of 3 × 0.5 mm were received from Goodfellow. Isotopes of ^{111m}Cd were implanted at room temperature into samples with energy of 30 keV and a dilute concentration in the order of 1.1 × 10¹¹ at/cm² provided by the ISOLDE/CERN radioactive beam facility [98]. Since the implantation damage had to be reduced, all samples were annealed for 15 minutes at 873 K in a quartz tube, in air (annealed were all but samples measured at 873 K) prior to TDPAC measurements. It is important to point out that samples measured at RT were measured outside of the furnace. The chosen ^{111m}Cd isotope decays to ¹¹¹Cd and a cascade of 151-245 keV is released via isomeric transition, thus after-effects or/and chemical rearrangements can be excluded. SRIM calculations [107] showed that the depth of implantation should not exceed 30 nm (average 15 nm). The simulated implantation profile was shown in Figure 3.3, subsection 3.2.1.

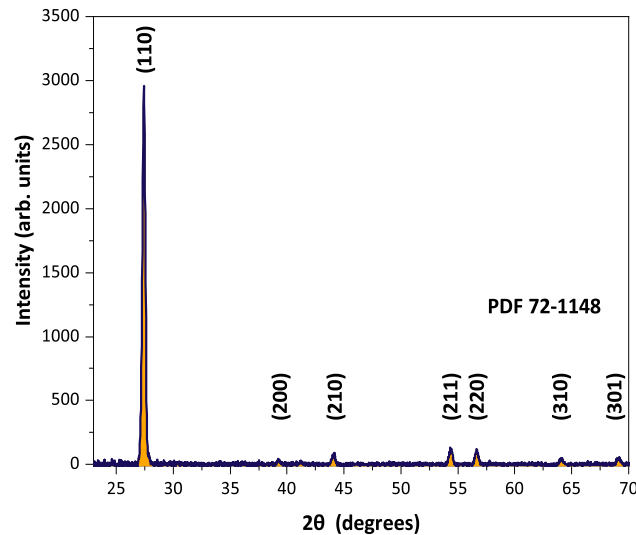


FIGURE 4.2: XRD pattern of pristine samples prior to studies.

A tracer diffusion method was applied with the same Cd isotope (see section 3.2.2). Approximately 4×10^{11} atoms of that ^{111m}Cd isotope were implanted. To be sure that nothing had an impact on the measurements the samples were annealed under the same conditions as the other samples with subsequent studies using an on-line diffusion chamber [109, 110]. Later on, the penetration profile was experimentally determined by virtue of ion beam sputtering using an Ar-ion beam. To measure the activity of each section, an available NaJ γ -detector with a 16 K multi-channel analyser was employed to observe the 245 keV peak. The relative radioactivity of the Cd isotope was carefully determined by the background subtraction, including the Compton scattering, and the half-life correction. The penetration depth can be estimated by the mass difference of the sample before and after the whole experiment using a microbalance, and assuming a constant sputtering rate. During sputtering, the beam current was recorded and proved to be constant within

$\pm 5\%$. X-ray diffraction patterns were recorded with a SIEMENS/BRUKER D 5000 X-ray diffraction using Cu-K α radiation at 40 kV and 40 mA, with a pristine sample being scanned from 20° to 80° with a step size of 0.02° in Bragg-Brentano geometry (shown in Figure 4.2).

4.1.3 Results and Discussion

4.1.3.1 Annealing of the Local Environment

Figure 4.3 represents perturbation functions for TiO₂ measured over a temperature range, while Figure 4.4 shows derived hyperfine parameters. Two fractions (labelled as F.I and

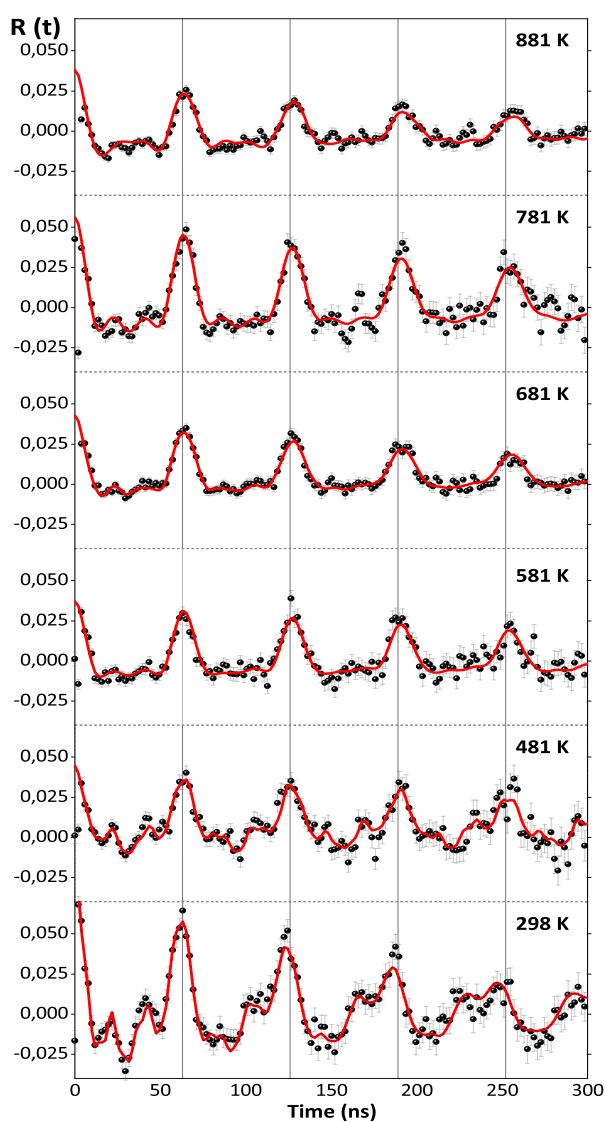


FIGURE 4.3: Perturbation functions for TiO₂ samples implanted with $^{111m}\text{Cd}/\text{Cd}$ probe and measured at indicated temperatures. The red solid line represents experimental fitting.

F.II) were needed to fit the following spectra. The derived parameters are shown in Table 4.1. A sample measured at room temperature (298 K) exhibited a well defined frequency (F.I) $\omega_{01} = 100.2(2)$ Mrad \cdot s $^{-1}$, asymmetry parameter $\eta_{01} = 0.20(1)$ and distribution width $\delta_{01} = 3.3(2)\%$. Since these numbers are close to Ag/Cd studies [121], it is indoubtable to attribute Cd being at the substitutional site. The second fraction was characterised with $\omega_{02} = 286.5(9)$ Mrad \cdot s $^{-1}$ and $\eta_{02} = 0.24(1)$. The fractions ratio is 61.9(22) and 38.1(27)% for F.I and II, respectively.

Table 4.1: $^{111m}\text{Cd}:\text{TiO}_2$ fitting parameters featuring two fractions. Here, ω_0 is given in Mrad \cdot s $^{-1}$, δ and percentage are in % while V_{zz} numbers are presented in (10^{21} V \cdot m $^{-2}$).

Temp.	Fraction I percentage	ω_{01}	η_{01}	δ_{01}	V_{zz}
298 K	61.9(22)	100.2(2)	0.20(1)	3.3(2)	5.786
481 K	75.6(66)	98.4(3)	0.13(1)	1.9(3)	5.680
581 K	85.2(56)	98.5(2)	0.07(1)	1.7(2)	5.687
681 K	87(6)	98.3(2)	0.06(2)	2.8(2)	5.672
781 K	89.1(54)	98.6(2)	0	2.1(2)	5.695
881 K	91.4(47)	98.0(2)	0	3.4(2)	5.657
Temp.	Fraction II percentage	ω_{02}	η_{02}	δ_{02}	V_{zz}
298 K	38.1(27)	286.5(9)	0.24(1)	4.6(9)	16.54
481 K	24.4(33)	282.3(11)	0.23(1)	1.0(4)	16.30
581 K	14.8(10)	201.8(15)	0.25(5)	0	11.65
681 K	13(1)	183.2(11)	0.24(1)	0	10.55
781 K	10.9(7)	166.1(23)	0.22(5)	0	9.593
881 K	8.6(9)	142.5(5)	0.25(1)	0	8.228

To be able to easily follow changes taking place in derived parameters of F.I, Figure 4.4 is complemented with previously reported experimental data. Figure 4.4 shows previously reported V_{zz} which were recalculated considering the last reported Q of Cd based on the same calculations [113]. The current results at room temperature are slightly different from previous ones captured in monocrystals. While the EFG is slightly lower than ones previously reported, the asymmetry parameter is higher. It is reasonable to expect the decrease of ω_0 with an increase of temperature due to the lattice thermal expansion, local relaxation. As the temperature is rising the asymmetry decreases down to $\eta = 0.07(1)$ and vanishes later on. Linear growth occurred after asymmetry reached 0 in previous experiments performed on polycrystalline samples [83] at 700-800 K. On the current set of experiments one cannot clarify this growth.

Variations in the fraction ratio are depicted in Figure 4.4. Following annealing at 700 - 800 K F.I reaches 90%, whilst F.II almost disappears with 8.6%. The EFG of the first fraction shows minor fluctuations from 481 to 781 K, after it drops to its minimum of $V_{zz} = 5.657 \cdot 10^{21}$ V \cdot m $^{-2}$ at 881 K. Previously, both single (5.83) and poly (5.86) crystallines' V_{zz} have been characterised having higher EFGs which have not been observed in the current study [83, 126]. The distribution width fluctuates over temperatures for the F.I, while it

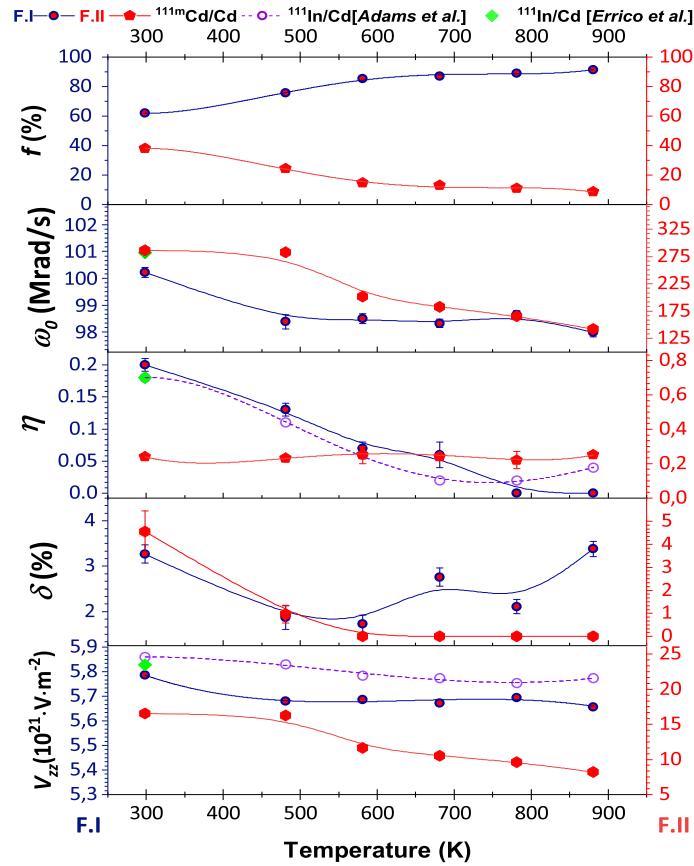


FIGURE 4.4: Hyperfine parameters of TiO_2 samples implanted with $^{111m}\text{Cd}/\text{Cd}$ probe and measured at indicated temperatures, accompanied by results of similar studies performed on bulk samples of rutile. For the convenience of following the trends data point were fitted with the polynomial regression function. The data from the references is shown for a good comparability, and belongs to the left axis (F.I). EFGs from references were recalculated utilising the last reported Q of Cd, based on the same first-principle calculations.

disappears for F.II from 581 K. A piking behaviour between of 500 - 800 K is similar to the polycrystalline $^{111}\text{In}/\text{Cd}$ study [30]. One could explain the peak of distribution width in terms of V_o , which become highly mobile and the probe atoms commence their presence in a defect free local environment with rising temperatures [38]. Possessing initially high ω_0 F.II drops twice to 142.5(5) by 600 K. Based on the gradual decline of distribution width δ_{02} , one could assume that the lattice recovery is taking place during annealing and measurements performed above RT. Albeit, asymmetry of the second fraction is not affected by annealing and stays in order of 0.24(1) over the course of temperatures.

Measurements performed with $^{111m}\text{Cd}/\text{Cd}$ isotope cannot distinguish whether the relaxation caused by hopping of trapped V_o happens. Additionally, the high temperature ferromagnetic behaviour has not been observed. In order to understand how mobile Cd

impurities were tracer diffusion studies were carried out.

4.1.3.2 Cd-tracer Diffusion

The concentration profile of ^{111m}Cd in rutile (blue circles) is presented in Figure 4.5 as a function of the penetration depth. The resulting tracer distribution is characterised by a high near-surface activity followed by a decrease of the concentration following approximately the Gaussian solution of the diffusion problem [127]:

$$c^*(x, t) = \frac{M_0}{\sqrt{\pi D_v t}} \exp\left(-\frac{x^2}{4D_v t}\right). \quad (4.1)$$

Here, c^* is the relative specific activity of the layer, which is proportional to the solute concentration, M_0 is the initial tracer amount, x is the penetration depth, t is the diffusion time, and D_v is the volume diffusion coefficient. However, previous diffusion experiments performed in the same on-line diffusion chamber under the same conditions show the influence of distinctly increasing tracer concentrations at the near-surface branches of the penetration profiles [128, 129]. Accordingly, the profiles were analysed using Strohm's solution [130]:

$$c^*(x, t) = \frac{\frac{M_0}{2}}{\sqrt{1 + \left(\frac{2D_v t}{\sigma^2}\right)}} \times \left[\operatorname{erfc}\left(\frac{-\frac{x_0}{2\sigma^2} - \frac{x}{4D_v}}{\sqrt{\frac{1}{2\sigma^2} + \frac{1}{4D_v}}}\right) \cdot \exp\left(\frac{-(x - x_0)^2}{2\sigma^2 + 4D_v t}\right) + k \cdot \operatorname{erfc}\left(\frac{-\frac{x_0}{2\sigma^2} + \frac{x}{4D_v}}{\sqrt{\frac{1}{2\sigma^2} + \frac{1}{4D_v}}}\right) \cdot \exp\left(\frac{-(x + x_0)^2}{2\sigma^2 + 4D_v t}\right) \right], \quad (4.2)$$

with M_0 being the maximum relative specific activity, x_0 the implantation depth, σ^2 the width of the implanted tracer distribution, and k which accounts for the surface conditions. If $k = +1$, the surface acts as a perfect reflector for the diffusing atoms or the surface acts as a perfect sink if $k = -1$. In this experiment, no Cd evaporation at the surface was observed; however, Strohm's solution is generally applicable for tracer experiments with implanted tracer atoms in a specific depth. The value k was found to be $+1$, so the sample surface acted as a perfect reflector for the diffusing Cd atoms during the annealing treatment under air conditions. In the near-surface branch, the volume diffusion coefficient was found to be $D_v^I = 4.9 \times 10^{-18} \text{ m}^2\text{s}^{-1}$. Beginning at a depth of approximately 300 nm a second branch with a decreasing tracer concentration to the background level following the Gaussian solution was observed. In this branch, the volume diffusion coefficient was found to be $D_v^{II} = 4.5 \times 10^{-16} \text{ m}^2\text{s}^{-1}$, which is approximately 2 orders of magnitude faster than in the near-surface branch. Sasaki *et al.* [131] found that the charge state of the impurity in single-crystalline rutile plays an important role according to the diffusion mechanism, i.e., divalent impurities like Co and Ni diffuse rapidly along the "open channels" parallel to the c -axis in the rutile structure and trivalent impurities like Sc and Cr diffuse by interstitialcy mechanism. There are also impurities like Fe and Mn which are so-called mixed-valent

impurities and diffuse both along the open channels and by the interstitialcy mechanism. Recently, abnormal diffusion behaviour in the open channels of rutile has been described, which is dependent on the size of dopants [132].

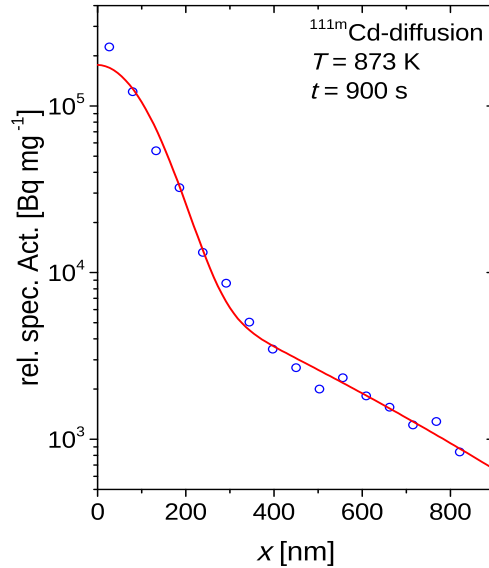


FIGURE 4.5: Penetration profile for Cd-diffusion measured at 873 K (blue circles). The red solid line corresponds to the fits by Eq.(4.1), and (4.2) and x is the penetration depth.

In this experiment, Cd likely belongs to the group of divalent impurities, and shows anisotropic migration (similar to Co, Ni) of dopants [131]. In accordance to Sasaki *et al.* [131], one can expect solely one mechanism taking place; however, current results seem to feature two distinct realisations. The second one could be related to the fact that rutile is typically nonstoichiometric and always contains not only V_o but also interstitial Ti ions. Those interstitials can in turn enable the diffusion process perpendicular to the c -axis via so-called “kick-off” mechanism [132]. Through this path, a dopant is switching between the substitutional and interstitial site. Thus, the slow near-surface branch is mainly influenced by the Cd-ions diffusing perpendicularly to the c -axis via the kick-off realisation, while the second branch in the range of 300 – 800 nm corresponds to the Cd-ions diffusing rapidly along the open channels.

Even though TDPAC spectra were well analysed in terms of two fractions, one may suspect that there may be a presence of another influence. That being said, the surface is still abounded in defects caused by implantation such as various V_o and complexes, which cannot be annihilated that easily, and one may expect the whole picture to be different and the surface layers feature in addition Magnéli phases or high quantity of interstitial Ti. On the whole, calculations may shed some light on this. There have been numerous attempts to study electronic properties of rutile TiO_2 based on many various approximations, and this task was remarkably simplified by varying solely scenarios where V_o could cause influence on the EFGs. In Table 4.2, V_{zz} DFT-based calculated hyperfine parameters for TiO_2 with Cd are summarised. It is important to point out that over the course of the studies performed on TiO_2 , various authors used the different quadrupole moments of Cd. This in

fact influenced final V_{zz} and some previous experimental results may be misleading.

4.1.3.3 *Ab-initio* Studies of the Electronic Structure

Since calculated hyperfine parameters are less sensitive to subtle changes which one cannot take into account, it is always preferable to compare them with experimental data. Therefore, to enhance the aforementioned results, several DFT-based *ab-initio* calculations for Cd-doped TiO₂ rutile were performed. For calculations with an isolated impurity, one had to construct a supercell sufficient enough for each impurity to not interact with its nearest one. The $2 \times 2 \times 3$ supercell is composed of 12 rutile unit cells. This supercell is tetragonal with $a = b = 9.173 \text{ \AA}$ and $c = 8.862 \text{ \AA}$ constants taken from 15 K neutron powder diffraction study [133]. Given the fact that real samples could feature various electron recombination processes near the impurity, it is vital to properly describe the structural and electronic properties of the system. Thus, were carried out calculations for various possible scenarios where Cd is replacing Ti. Likely, these scenarios are: an idealised situation where the impurity Cd:Ti⁰ has a neutral charge, one and two additional electrons provided, and where equatorial and apical V_o are near the probe.

Table 4.2: Comparison of calculated hyperfine parameters with current experimental data of TiO₂ rutile. Current scenarios are: Cd at the Ti site, 1, 2 additional electrons; and V_o ap. ap. and V_o eq. eq. are apical and equatorial oxygen vacancies, respectively. Me-O d_1 Me-O d_2 are the distances after relaxation given in \AA , between Me and four and two oxygen neighbours, respectively. Results from other publications are shown for the comparison. Experimental data from the current work taken at RT. In d_1 for V_o eq. an average distance (of 3) is used. V_{zz} numbers are presented in ($10^{21} \text{ V}\cdot\text{m}^{-2}$)

System:	V_{zz} ; direc.	η	Me-O d_1	Me-O d_2	Aprox.	Refs.
Rutile	-	-	1.95	1.97	PAW-PBE	This work
Cd:Ti ⁰	6.14	0.91	2.19	2.12	PAW-PBE	This work
Cd:Ti ⁰	-7.16; X	0.91	2.15	2.11	LDA	Ref. [134]
Cd:Ti ⁰	-7.90	0.80	2.15	2.11	PBE	Ref. [134]
Cd:Ti ⁰	6.00	0.83	-	-	GGA-WC	Ref. [135]
Cd:Ti(1 \bar{e})	6.41	0.41	2.20	2.12	PAW-PBE	This work
Cd:Ti(2 \bar{e})	6.18	0.30	2.20	2.12	PAW-PBE	This work
Cd:Ti(2 \bar{e})	4.55; Y	0.26	2.18	2.11	LDA	Ref. [134]
Cd:Ti(2 \bar{e})	5.00	0.39	2.20	2.13	GGA-WC	Ref. [135]
Cd:Ti + V_o eq.	20.15	0.15	2.21	2.11	PAW-PBE	This work
Cd:Ti + V_o ap.	17.65	0.37	2.17	2.25	PAW-PBE	This work
Exp. F.I	5.79	0.20	-	-		This work
Exp. F.II	16.54	0.24	-	-		This work

Ab-initio calculations have been performed utilising the PAW method [136] based on $3 \times 3 \times 3$ k-points grids implemented in vasp environment [93] (5.4.1). In the current calculation the theoretical PBE exchange-correlation functional [137] with a $2 \times 2 \times 3$ supercell was utilised. In the crystal lattice, various possibilities are feasible (as well as functionals). Hence, only scenarios missing in the literature were taken into consideration. In this case, it

was related to oxygen vacancies. Determined hyperfine parameters are shown in Table 4.2 and complemented with existing measurements based on different approximations. The atomic coordinates were relaxed until the forces were smaller than $1 \text{ meV}/\text{\AA}$. Table 4.2 shows the results for the relaxation of the six nearest oxygen neighbours of the Cd impurity.

Calculations performed for rutile match closely with previous theoretical calculations and experimental results [133, 135]. As it is evident, d_1 and d_2 are anisotropic, where distances of d_2 are bigger than d_1 . Any changes in the local environment develop into inevitable swapping of anisotropy and d_1 becomes bigger. This observation has been well described previously [126] and based on the assumption that stretching of Cd-O d_2 bond induces shortening of Ti-O d_2 , while Ti-O d_1 is less exposed to changes due to expansion of Cd-O d_1 . The addition of electrons does not affect bonds significantly and they remain close to Cd:Ti⁰ and coincide with ones calculated with *Generalised Gradient Approximation by Wu and Cohen* (GGA-WC) functional. A slightly different picture is observed in the case of Cd:Ti + V_o eq. and ap. The latter shows decrease of equatorial oxygen distances, but the growth of the remaining apical distances. Moreover, in Cd:Ti + V_o eq. scenario, equatorial oxygen distances are now different for each atom of oxygen: $d(\text{Cd1-O41}) = 2.1677 \text{ \AA}$, $d(\text{Cd1-O32}) = 2.1445 \text{ \AA}$ and $d(\text{Cd1-O33}) = 2.3153$ and 2.10891 \AA (apical).

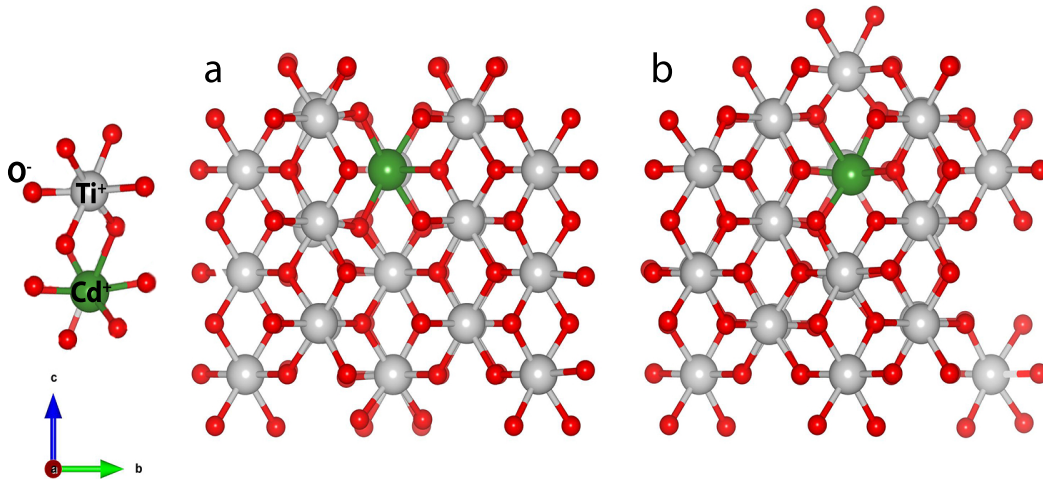


FIGURE 4.6: Two different Cd:Ti + V_o configurations in the $2 \times 2 \times 3$ rutile supercell. Here (a) stands for V_o apical and (b) represents V_o equatorial. Titanium and oxygen atoms are denoted as grey and red spheres, respectively, while green ones show cadmium.

Small differences between GGA-WC and LDA could be explained in terms of a strong EFG dependency r^{-3} . This dependency is induced by the charge sources due to the non-spherical charge distribution near the Cd nucleus and were observed in other doped metal oxide systems [78, 85]. Measurements performed at 298 K resemble our calculations most where the first fraction matches closely with PAW-PBE Cd:Ti(2 \bar{e}) and LDA calculations [134]. The local environment of Cd is changed once it is leaving its metallic state, which is unlikely to exist. To overcome the latter, 2 electrons are needed to fill the O- p band. Once electrons are provided, the local symmetry is affected. Obviously, the EFG is beyond these numbers.

Significant impact on the asymmetry could take place when implanted Cd is located

in the disrupted surface environment, where V_o are most stable [138]. The ion implantation leaves the surface layers in a more disrupted state, then they were before, making it a favourable place for defect accumulations, which can be hardly recovered after annealing. Based on the tracer study, it is possible to tentatively attribute additional environment for the second fraction. This attribution is additionally supported by calculations where cases featuring Cd:Ti near either V_o eq. ($20.15 \cdot 10^{21} \text{ V}\cdot\text{m}^{-2}$) or V_o ap. ($17.65 \cdot 10^{21} \text{ V}\cdot\text{m}^{-2}$) are considered (see Figure 4.6). Rising of temperature, however, decreases both the amount of F.II and the EFG, seemingly due to Cd diffusion into the bulk.

4.1.4 Conclusions

In the current study the hyperfine structure analysis of $^{111m}\text{Cd}/\text{Cd}$ as a function of temperature in TiO_2 single crystalline rutile has been presented. For a more accurate understanding of the processes taking place within, the results are complemented with both a tracer diffusion study and *ab-initio* theoretical study. Experimental data has shown the presence of two fractions - two local environments. Applied tracer diffusion studies have well demonstrated that Cd is fairly mobile. On the other hand, the biggest Cd fraction is located near the surface. Calculated results considering the presence of oxygen vacancies (apical) match closely with experimental data.

4.2 Defect Behaviour and Thermal Stability in Hydrogenated Anatase

Emission Mössbauer spectroscopy experiments using ^{57}Mn radioactive beam implanted at ISOLDE/CERN into pristine and hydrogenated anatase (TiO_2) thin films in dilute concentrations are reported. Studies contain both experimental and theoretical parts. The latter is by carrying out first-principles calculations based on the density functional theory. Obtained experimental results depict the evolution of electronic structure of pristine anatase thin films doped with Fe in a temperature range 300 - 700 K. Throughout the measurements both Fe^{2+} and Fe^{3+} have been spotted. Two annealing stages have been distinguished: 1) a 300-373 K stage where most of Fe^{3+} is transformed into Fe^{2+} due to vacancies movement; 2) up to 623 K, which is induced by Ti interstitials Ti vacancies mutual annihilation. Dissociation energy in anatase has been estimated to be of > 1.8 eV for Mn- V_o pairs. Hydrogenated eMS spectra show no Fe^{3+} , suggesting that hydrogen behaves as a shallow donor. In addition, surrounding oxygen vacancies favour the Fe^{2+} state. Depending on a degree of hydrogenation hydrogen in films acts differently. Sample treated at room temperature (RT) shows two distinct processes of hydrogen motion, starting with interstitial switching over to covalent, while in a 573 K treated sample both stages lay over each other due to bulk defect hindering desorption. What is more, UV-vis and conductivity measurements have been performed to determine an impact of the treatments on properties of the films, showing improved conductivity and higher absorption. XPS at RT reveals that the sample hydrogenated at 573 K shows presence not only of Ti^{3+} but also Ti^{2+} states, pointing out at significant amount of oxygen vacancies (V_o) and -OH bonds. Theory suggests that in anatase implanted with Mn(Fe), probes were located close to a vacancy, as next-nearest neighbours. This subsection is based on Zyabkin *et al.* "Experimental and Theoretical Study of Electronic and Hyperfine Properties of Hydrogenated Anatase (TiO_2): Defect Interplay and Thermal Stability", *J. Phys. Chem. C.*, 124 (13), 7511-7522 (2020).

4.2.1 Overview

Recently, anatase has attracted significant attention due to good performance for water splitting with high yields under ultraviolet exposure. High photocatalytic activity, in contrast to other TiO_2 polymorphs (rutile and brookite), is attributed to high carrier separation efficiency, mainly due to a different octahedral arrangement of Ti- O_6 [139, 140]. Furthermore, the material is abundant, stable, and highly reactive [141–143]. Recently, the reduction of anatase in different atmospheres (e.g., hydrogen) has triggered numerous experiments towards its application (from hydrogen production to photocatalytic reduction). The approach is based on the principle of introducing a plethora of defects, creating enough lattice disorder at the surface or near-surface regions of TiO_2 (i.e., oxygen deficiency and hydrogen doping) [40, 144, 145]. Such treatments have shown to remarkably intensify both visible and infrared absorption, thereby increasing the yields of hydrogen production above most photocatalysts of this type. The structure of hydrogenated anatase is identified as consisting of a crystalline lattice core surrounded by an amorphous shell (such as Ti_4O_7) containing the hydrogen dopant [40, 144, 146]. Besides the intentional lattice dopant, hydrogen is well known to be a common impurity in semiconductors with a prominent impact on electronic and optical properties. Theoretical investigations have shown that hydrogen

in TiO_2 primarily tends to bond with oxygen and then acts as a donor or as an amphoteric defect [51, 147].

Even though there is a lack of experimental data available on anatase doped with hydrogen, the results obtained on rutile vary remarkably. Recent studies on rutile have shown that the electron associated with a hydrogen centre is not delocalised (same as anatase), as one may assume for a shallow effective mass donor, but localised close to a Ti ion as a polaron [148, 149]. A few IR absorption studies on hydrogenated anatase show that after hydrogenation several new lines become evident. This has been attributed to the stretching of the local vibrational mode of -OH bonds [150, 151].

The photocatalytic efficiency of TiO_2 -based materials is confined not only by the large band-gap (3.2 eV for anatase) but also by the losses due to the defect-induced recombination [152]. On the contrary, when defects such as oxygen vacancies (V_o) or Ti^{3+} are induced in small quantities, they affect the photocatalytic performance positively [146]. Therefore, it is of great importance to understand the role of defects and their interactions in hydrogenated TiO_2 .

In this work, I report on studies of the defect and electronic structure of pristine and hydrogenated anatase TiO_2 thin films by means of ^{57}Fe emission Mössbauer spectroscopy (eMS) [100] following the implantation of ^{57}Mn ($t_{1/2}=1.5$ min.) in a temperature range from ~ 295 to 700 K. In addition, I complement the eMS studies with X-ray photoelectron spectroscopy (XPS), resistivity measurements, grazing incidence X-ray diffraction (GIXRD) and *ab-initio* density functional theory calculations within VASP and WIEN2K environments [92, 93].

To develop a clear picture of hydrogen behaviour in thin film two differently hydrogenated samples have been studied. Obtained results show that hydrogen has a strong influence on the electronic structure (in comparison to pristine samples) and shows a behaviour depending on the hydrogenation degree. One could clearly observe two types of hydrogen present in the samples: interstitial and covalently bound. Oxygen vacancies may potentially support hydrogen in the lattice up to high temperatures. Theory suggests that the defect interplay is more complex than previously expected.

4.2.2 Experimental Section

4.2.2.1 Sample Preparation

TiO_2 thin films were deposited onto Si and quartz substrates by radio frequency sputtering (LA 440S by VON ARDENNE) utilising a ceramic TiO_2 target (99.9% FHR Anlagenbau, Germany). During the process, the sputtering power was maintained at 200 W and the Ar flux was fixed at 80 sccm. The thickness of thin films was measured with an ellipsometer (Sentech SE 801) and the crystal structure was determined by virtue of GIXRD. Prior to hydrogenation, the samples were annealed at 773 K for 3 hours to ensure their crystallisation into anatase. Thereafter, the samples were treated in a chamber for plasma-enhanced hydrogenation treatment, where an inductively coupled plasma (ICP) instrument (Plasma Lab 100 ICP-CVD, Oxford Instruments) was used. The H_2 plasma treatment was performed for 30 minutes at two distinct temperatures, room temperature and 573 K, producing the $\text{TiO}_2\text{:H-RT}$ and $\text{TiO}_2\text{:H-573}$ samples, respectively. The ICP power was held at 2000 W, the chamber pressure at 3.5 Pa, and the H_2 flow rate at 50 sccm.

4.2.2.2 Sample Characterisation

The samples were characterised by GIXRD, UV-vis optical absorption, XPS, and resistivity measurements, while the information on Fe related defects and their charge states were obtained from emission Mössbauer Spectroscopy experiments.

GIXRD patterns were recorded with a SIEMENS/BRUKER D5000 X-ray diffractometer using Cu-K α radiation at 40 kV and 40 mA, with the samples being scanned from 23° to 80° with a step size of 0.02°. Optical absorption in the UV to visible wavelength range was measured using a UV-vis spectrometer (Varian Cary 5000 UV-vis-NIR). Room temperature resistivity measurements were conducted using a 10 V four-point probe setup (Jandel engineering) in linear Van der Pauw arrangement. XPS analysis was performed utilising the normal emission utilising monochromatic Al-K α ($h\nu = 1486.7$ eV) radiation. Further details of the experimental setup are described in [153]. Core-level spectra were recorded at a constant pass energy (13 eV) with a total energy resolution of 0.6 eV in the absence of charge neutralisation as well as a further binding energy correction. The correction of the binding energy was made with the C 1s peak, assigned with a binding energy of 285 eV. The accuracy for binding energy assignment was estimated to be ± 0.2 eV.

^{57}Fe eMS measurements were carried out at the ISOLDE/ CERN facility [98, 154] where the parent radioactive isotope was produced with 1.4 GeV proton induced fission in a heated UC $_2$ target and element-selective laser ionization [155]. Following acceleration to 40 keV and magnetic mass separation, the ^{57}Mn ions were implanted into the polycrystalline anatase TiO $_2$ samples held at the implantation/measurement temperature ranging from 295 to 735 K within an implantation chamber. Samples were mounted with surface normal at 30° relative to the beam direction. Emission Mössbauer spectra were recorded during the implantation using a resonance detector equipped with a ^{57}Fe enriched stainless steel electrode, mounted on a conventional drive system outside the implantation chamber at 60° relative to the sample's normal.

In all cases, the samples were implanted with a total fluence below 3×10^{12} ^{57}Mn ions/cm 2 , thus providing a truly dilute concentration. From SRIM calculations [107], the ion range was estimated to be 22 nm, the maximum local concentration $\sim 10^{-3}$ at.%. Isomer shift values are given relative to α -Fe at RT.

4.2.3 Results and Discussion

4.2.3.1 General Characterisation

Figure 4.7a shows the GIXRD patterns of the anatase thin films, as prepared (TiO $_2$:as-prepared), after 3 hours of annealing at 773 K (TiO $_2$: pristine) and the two hydrogen treated samples (TiO $_2$: H-RT and TiO $_2$: H-573 K). The films were 100(7) nm thick. The results show that the as-prepared film is amorphous, which, after 773 K annealing, is crystallised into the single anatase phase, with the diffraction reflections corresponding close to expectations (PDF-89-4921). After hydrogenation, the diffraction peaks increased slightly in intensity and became clearer. Neither the rutile phase, nor TiH $_2$ is observed in the GIXRD patterns.

After the hydrogenation, the samples changed their colour from white (pristine) to grey (TiO $_2$:H-RT) and black (TiO $_2$:H-573) reflecting changes in their optical and structural properties. Sun *et al.* [156] have reported the amount of hydrogen stored in the TiO $_2$ crystals may be dependent on their facets, which in turn could also affect the colour changes (a

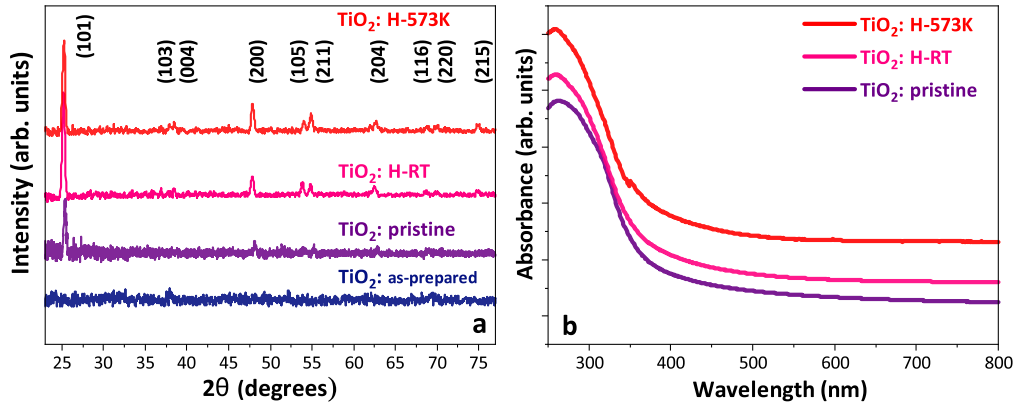


FIGURE 4.7: (a) XRD patterns and (b) UV-vis absorption spectra of as-prepared TiO₂ and after annealing (pristine), the samples hydrogenated at RT TiO₂:H-RT and the sample hydrogenated at 573 K TiO₂:H-573 K.

higher hydrogen concentration equals a darker colour). The amount of stored hydrogen was around 1.4 wt.% on the (101) surface (which is the most stable facet [157]), whilst 1.0 wt.% was found on the (001) surface. These authors commented that hydrogen should occupy the interstitial sites in the titanium-oxygen octahedra [156]. The effects of hydrogenation on the UV-vis absorption spectra of the films are presented in Figure 4.7b. The impact of hydrogenation at both temperatures is visible, however it is not so strong as in the case of TiO₂ powders [40]. The optical response of hydrogenated TiO₂ shows a clear increase in the absorbance, which is the characteristic of the oxygen vacancy impact on the light absorption properties of TiO₂ [158]. The TiO₂:H-573 sample extends the absorption edge of TiO₂ in the UV-visible range with a small red shift. The band-gap can be calculated using the Tauc model where the band-gap is dependent on equivalent absorption coefficient and the energy of photons [159]. From these calculations, the sample hydrogenated at room temperature exhibits decreased band-gap by 0.04 eV, while the 573 K sample shows a reduced band-gap by 0.13 eV. These changes are similar to the finding of previous works [160, 161]. Therefore, the UV-visible absorption spectra indicate the creation of oxygen vacancies in TiO₂ after hydrogenation.

Resistivity measurements show the gradual decrease of resistivity with the hydrogenation treatments. The pristine TiO₂ films showed a resistivity greater than $2 \times 10^5 \Omega \cdot \text{m}$ which is above the instrumentation limitation. However, the sample hydrogenated at RT shows a rapid decrease to $6.2 \times 10^{-6} \Omega \cdot \text{m}$ while the sample treated at 573 K shows a further decrease to $4.3 \times 10^{-6} \Omega \cdot \text{m}$. This can be interpreted as the release of electrons trapped in V_o or deficient Magnéli formations [29]. Therefore, in correlation with optical absorption results, the higher V_o concentration, the greater the electron participation in conductivity [162].

The near-surface/surface chemical bonding and electronic valence band positions of the TiO₂ films were investigated with XPS. Ti 2p and O 1s core-level spectra were recorded to evaluate the chemical states of Ti and O in TiO₂. The spectra of Ti 2p for the TiO₂ film

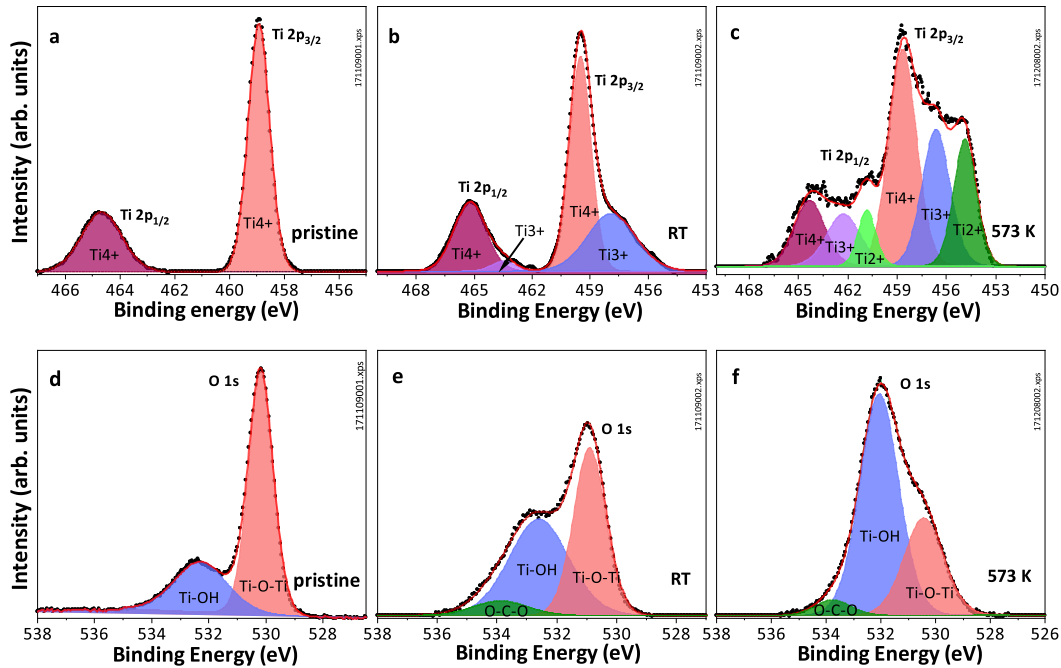


FIGURE 4.8: XPS core spectra for Ti 2p (a-c) and O 1s (d-f) of TiO₂ films before (a,d) and after hydrogenation treatments performed at room (b,e) and 573 K temperature (c,f).

before and after hydrogenation under different conditions are shown in Figures 4.8a-c. For the pristine sample shown in Figure 4.8a, only peaks due to Ti⁴⁺ are observed at 458.9 eV (2p_{3/2}) and 464.6 eV (2p_{1/2}) which are well known binding energies in pristine TiO₂ [163]. The spectrum of the sample hydrogenated at RT depicted in Figure 4.8b shows the evidence of reduction of Ti⁴⁺ ions to Ti³⁺ with two additional peaks centred at 457.9 eV (2p_{3/2}) and 463.1 eV (2p_{1/2}) attributed to Ti³⁺ ions. Previous research did not always report the presence of Ti³⁺ after such treatments, implying a high stability of Ti⁴⁺ which is against reduction to Ti³⁺ [164]. As shown in Figures 4.8a-c, after the hydrogenation at RT and 573 K, the Ti⁴⁺(2p_{3/2}) peak moves to 459.5 eV and 458.7 eV, respectively, in accordance with the previous results [165]. It has been reported that under certain circumstances Ti²⁺ states can be observed in black titania [41, 166]. Increasing the temperature during the plasma treatment caused a Ti²⁺ state to appear. This can be observed in Figure 4.8c, the new peaks emerged at 454.9 eV (2p_{3/2}) and 460.8 eV (2p_{1/2}) after hydrogen treatment at 573 K, which correspond to Ti²⁺.

Figures 4.8d-f show the O 1s core level XPS spectra for the pristine and hydrogenated samples at RT and 573 K. The O 1s spectra of the pristine sample can be deconvoluted into two peaks at 530.2 eV and 532.1 eV. The first is ascribed to oxygen in Ti-O-Ti bonds and the second to oxygen in Ti-OH in accordance with earlier data [167, 168]. There is evidence of changes in peak fractions of these two peaks representing Ti-O and Ti-OH bonds, although binding energies remain almost the same before and after hydrogenation treatments. However, a small positive shift in the binding energies of Ti-O-Ti after RT hydrogenation (from 530.1 to 530.9 eV) resembles the behaviour of Ti⁴⁺(2p_{3/2}), where

energies increased and returned after treatment at 573 K (from 458.9 eV to 459.5 eV). There is a third component on the surface, which has a binding energy of 533.5 eV and is assigned to an O-C-O bond owing to unintentional carbon contamination during sample handling/plasma treatments.

In addition, there is a clear trend of an increasing Ti-OH fraction and its further dominance over Ti-O-Ti after hydrogenation at 573 K. A similar tendency was observed and reported in other hydrogenated TiO₂ [40], which suggested the creation of more -OH bonds in subsurface regions.

Hydrogenated thin films show no significant disorder as presented in Figure 4.7. Even though the same hydrogenation parameters on rutile samples were utilised for a longer time period, a slightly amorphous phase of upper layers was detected by GIXRD. Based on the fact that there are no significant structural changes, and that the light absorption of the film after hydrogenation has been improved, One can deduce that the band-gap narrowing took place with hydrogenation. Several suggestions on the origin of the band-gap narrowing have been proposed. However due to its complexity and mutual Ti interstitial and vacancy interplay, the reasons remain unclear [40, 160]. Ti defects alone might play a small role; therefore one may guess that the localised states at 0.7-1.0 eV and 0.92-1.37 eV are induced by oxygen vacancies and Ti-H bonds, respectively [44, 158]. Researchers observed that the high electroconductivity in TiO₂ is due to Ti³⁺ and Ti²⁺ states along with oxygen vacancies, and this is in accordance with XPS results which show an increase of Ti defects with the temperature of the hydrogenation treatment [169, 170]. However, such extreme changes in electroconductivity have not been reported before. Typically, reduction from Ti⁴⁺ to Ti³⁺ originates from the surface and is always accompanied by a loss of oxygen.

With increasing time/temperature of hydrogenation treatments, hydrogen tends to increase its number of bonds with TiO₂. This is demonstrated in the changes of the Ti-O-Ti/Ti-OH ratio with hydrogenation as shown in Figures 4.8a-c.

XPS results indicate the presence of both the Ti²⁺ and Ti³⁺ states, which are likely accompanied by V_o defects in the TiO₂ films after hydrogenation treatment. Therefore, eMS was applied to probe these defects and their temperature-dependent interactions in hydrogenated TiO₂ on the atomic scale.

4.2.3.2 Emission Mössbauer Spectroscopy

A series of emission Mössbauer spectra recorded in the pristine sample is shown in Figures 4.9a-e, while Figure 4.9f is focused on the magnetic features (wings). I evaluated the spectra in terms of three components by virtue of the VINDA programme [88]. The central part consists of a doublet due to high-spin Fe²⁺ (D0). This part was calculated as a distribution of quadrupole splitting [171]. The quadrupole splitting and the isomer shift are coupled as $\delta = \delta_0 + \delta_1 \cdot \Delta E_Q$, where δ_1 and δ_0 are fitting variables. The derived isomer shift and quadrupole splitting at RT are $\delta_{RT} = 0.80(4)$ and $\Delta E_Q = 1.98(7)$ mm/s, respectively. It is straightforward to assign D0 to Fe ions at the substitutional sites in anatase [172]. The wings of the spectra show magnetic hyperfine splitting, similar to those observed previously in the eMS studies on rutile TiO₂ [38], which were attributed to high-spin Fe³⁺ showing spin-lattice relaxations on a comparable time scale as the lifetime of the 14.4 keV Mössbauer state of ⁵⁷Fe. This part of the spectra was analysed with the semi-empirical Blume-Tjon-based model (BT1&2) [173]. Figure 4.10c shows the relative area fractions of both Fe²⁺ and Fe³⁺ based on the simultaneous analysis of the spectra, while Figures 4.10a,b,d concen-

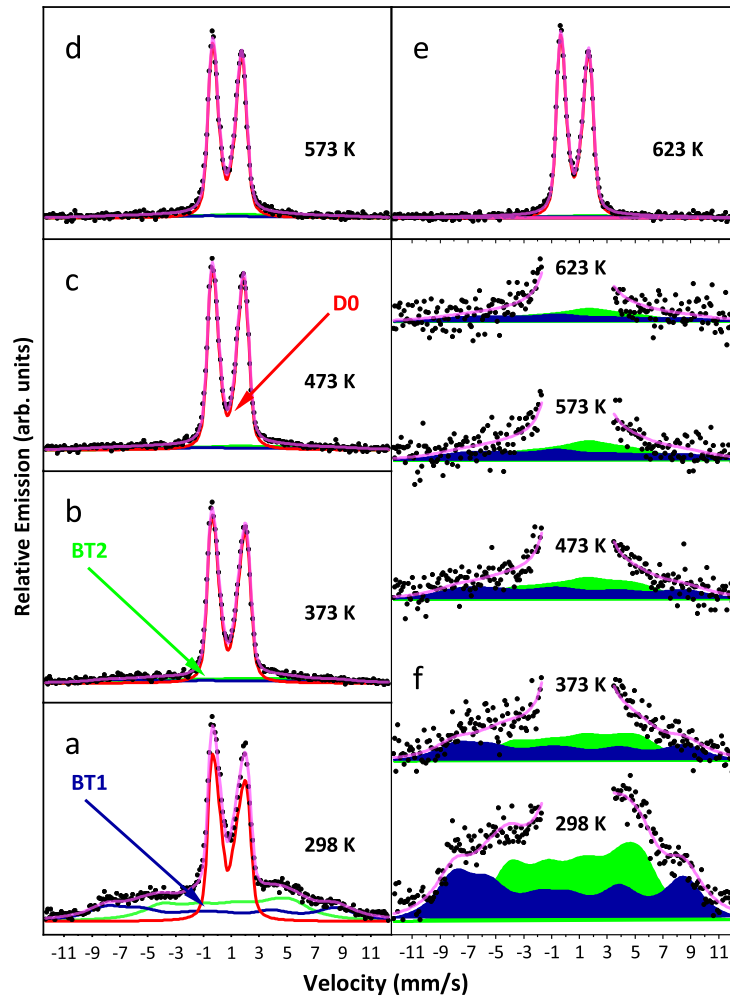


FIGURE 4.9: (a-e) ^{57}Fe emission Mössbauer spectra obtained at the temperatures indicated after implantation of ^{57}Mn into pristine anatase TiO_2 . (f) Magnified view of the spectra showing the effect of the magnetic splitting.

trate on the hyperfine parameters of Fe^{2+} . The derived results reveal two annealing stages: 1) between 300 K and 373 K and 2) from 373 to 623 K.

During the first stage, the majority of the Fe^{3+} ions are transformed into Fe^{2+} with increasing temperature, which is clearly observable in Figure 4.10c. The quadrupole splitting value of Fe^{2+} shown in Figure 4.10b shifts, and the isomer shift demonstrates an increase relative to the second-order Doppler shift (SOD) trend (in Figure 4.10a, shown as a solid line). The relative line broadening presented in Figure 4.10d decreases, and the quadrupole splitting distribution becomes more symmetric, as observed through the coupling parameter δ_1 between the isomer shift and the quadrupole splitting (not shown). This annealing stage is very similar to the annealing stage reported for rutile TiO_2 [38] around 330 K. At this temperature the Fe^{2+} area fraction, isomer shift and quadrupole splitting increased, while the quadrupole splitting distribution became narrower. One may attribute this stage

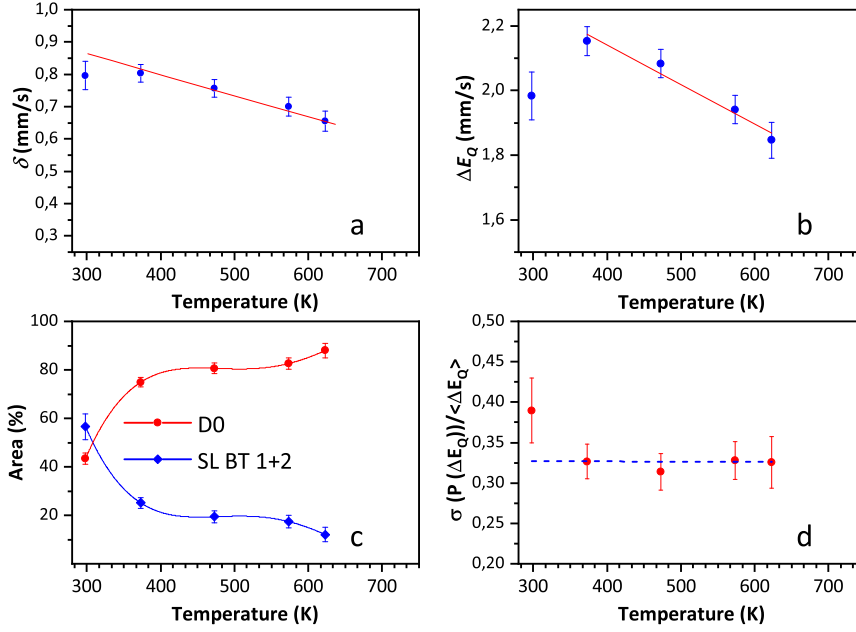


FIGURE 4.10: Temperature dependence of hyperfine parameters of Fe²⁺ (D0). (a) Average isomer shift. The solid line shows the second-order Doppler shift. (b) Average quadrupole splitting. The solid line shows the linear trend above 373 K. (c) Area fractions of the spectral components of the spectra in Figure 4.9. (d) Relative standard deviation of the quadrupole splitting distribution function. The dashed line shows the average above 373 K.

to the mobility of Ti interstitials (Ti_I) and/or Ti vacancies (V_{Ti}), leaving the probe atom in an environment with oxygen vacancies, thus promoting the 2+ state over the 3+ state. Gunnlaugsson *et al.* [38] interpreted the annealing effect in terms of Ti_I, mostly because rutile tends to form these interstitials more easily than anatase [174]. For this reason, the absence of the sharp annealing stage here at 330 K (unlike in rutile) can be in general interpreted as a less noticeable contribution of V_{Ti} and Ti_I mutual annihilation [174].

There is no evidence of the ~ 550 -600 K annealing stage reported in rutile TiO₂ [38], which the authors attributed to the dissociation of Mn-V_o pairs within the 1.45 min half-life of ⁵⁷Mn. This suggests that Mn-V_o pairs have higher dissociation energy in anatase, compared to rutile. Using the same method as in Ref. [38], one finds a dissociation energy > 1.8 eV for Mn-V_o pairs in anatase TiO₂. Furthermore, the second annealing stage observed here with Fe²⁺ (D0 component) dominating the spectra up to 650 K can be additionally supported by the fact that V_o are easily formed in anatase, especially under ion radiation [174, 175].

During the ⁵⁷Mn \rightarrow ⁵⁷Fe β^- decay an average recoil energy of 40 eV is transferred to the ⁵⁷Fe atom, which may lead to a relocation of atoms into the interstitial sites. However results show no indication of a spectral component that could be interpreted as due to interstitial Ti (the threshold displacement energy of Ti atoms is around 39(1) eV [176]). If interstitial Fe are formed, this could indicate that they can find their regular lattice site in less than 100 ns or they possess too low Debye-Waller factor to be observed in eMS measurements. The isomer shift shown in Figure 4.10a follows roughly the SOD at $T > 370$ K.

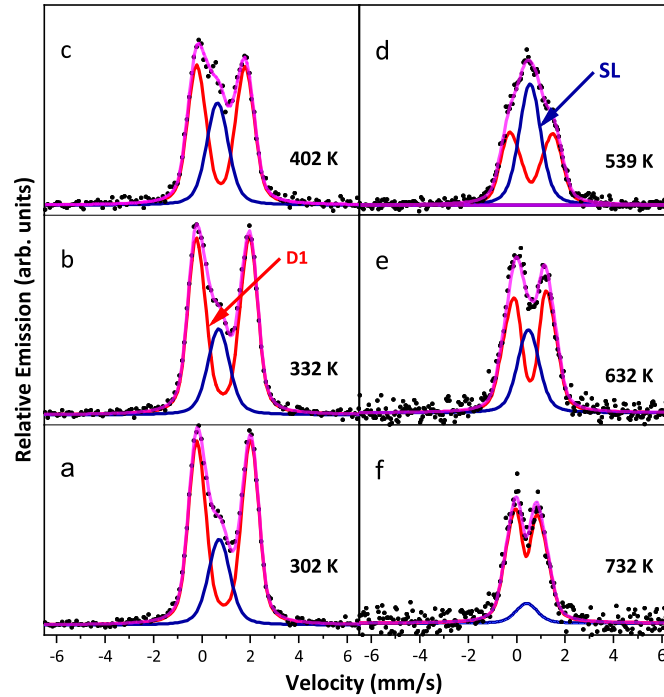


FIGURE 4.11: ^{57}Fe emission Mössbauer spectra obtained at the temperatures indicated after implantation of ^{57}Mn into $\text{TiO}_2\text{:H-RT}$.

The average quadrupole splitting in Figure 4.10b shows a smooth dependency above 370 K, with a sudden increase from 300 to 370 K. This resembles the results observed in rutile and is supposedly due to changes in the local environment [38]. Figure 4.10d shows that the same trend with the width of the quadrupole splitting distribution, suggesting that Fe^{2+} is not located in the amorphous environment in anatase. Only at higher doses of implantation, anatase becomes amorphous (1×10^{16} ions/cm 2) [177].

Figure 4.11 shows a series of eMS spectra obtained on the $\text{TiO}_2\text{:H-RT}$ sample. There are two major differences in comparison with the spectra obtained on the pristine sample (see Figure 4.9): 1) no Fe^{3+} component is observed and 2) the spectra have additionally an apparent single line (SL) and a doublet (D1), which resembles D0 in pristine TiO_2 and assigned to a high-spin Fe^{2+} . While the absence of Fe^{3+} can be explained by the doping effects of hydrogen, the presence of a single line in the eMS spectra from the noncubic structure of anatase at first glance represents an unexpected feature. The hyperfine parameters and relative area fractions of Fe^{2+} determined from the simultaneous analysis of the spectra are presented in Figures 4.12a-c. The derived isomer shift and quadrupole splitting for $\text{TiO}_2\text{:H-RT}$ obtained at RT for D1 are $\delta_{RT} = 0.90(4)$ and $\Delta E_Q = 2.19(6)$ mm/s, respectively. Apparently, these hyperfine parameters resemble those obtained in rutile.

The unknown SL has an isomer shift of $\delta_{RT} = 0.72(2)$ mm/s and demonstrates a temperature dependence. The isomer shift of D1 for the sample obtained after hydrogenation at RT depicted in Figure 4.12a does not follow the SOD. It is characterised by $\delta_{RT} = 0.90(4)$ mm/s close to 300 K and by $\delta \sim 0.4$ mm/s close to 750 K. The δ_{RT} is similar to the previously

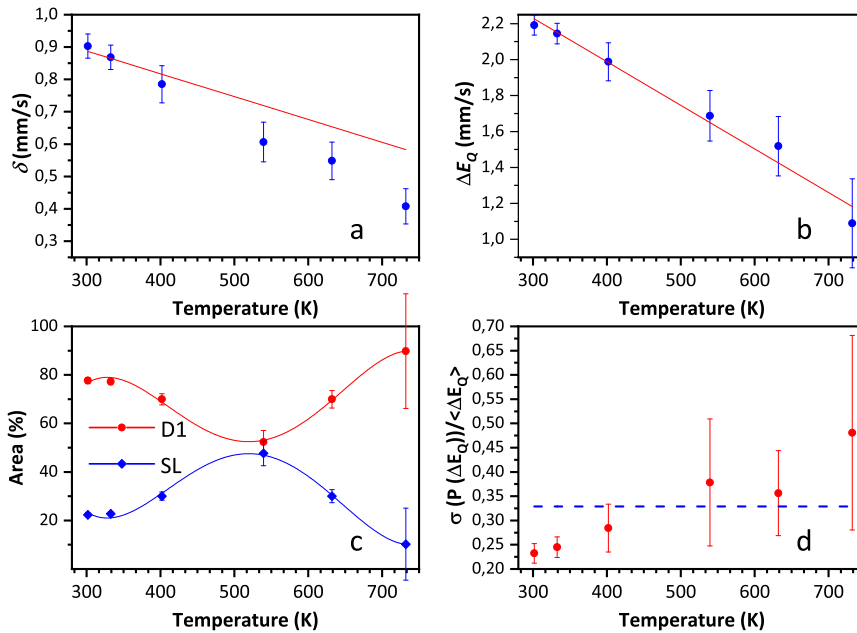


FIGURE 4.12: Temperature dependence of hyperfine parameters of Fe²⁺ (D1) for TiO₂:H-RT. (a) Average isomer shift. The solid line is a comparison to the SOD shift. (b) Average quadrupole splitting. (c) Area fractions of the spectral components of the spectra in Figure 4.11. (d) Relative standard deviation of the quadrupole splitting distribution function.

obtained D0 in the pristine sample shown in Fig 4.10. This could suggest either a change in the local environment or addition of another unresolved spectral component with a lower isomer shift. The quadrupole splitting ΔE_Q of D1 is close to ~ 2.2 mm/s, which is similar to the value obtained for D0 in the analysis of eMS spectra of the pristine sample above the 330 K annealing stage. For the pristine sample, the (extrapolated) quadrupole splitting of D0 is ~ 1.8 mm/s at 700 K, while for D1 of the sample hydrogenated at RT, the value 1.2 mm/s is obtained. The presence of two unresolved quadrupole split components in Figure 4.12d explains the broadening of the D1 component. Approximately at 300 K, the spectra are dominated by a contribution similar to D0 of the pristine sample, while at 750 K, they are also composed of another contribution that has a lower isomer shift and quadrupole splitting. The addition of the two contributions would give a broader final component at elevated temperatures. This suggests a broad annealing stage centred at around 500 K, coinciding with the peak in the SL area fraction as shown in Figure 4.12c. Moreover, there is no 330 K annealing stage observed in the pristine sample.

The sample hydrogenated at 573 K demonstrates a different temperature behaviour as depicted in Figure 4.13. There is no annealing stage visible in the pristine sample. However, the collapsing stage persists up to 650 K. The isomer shift of D2 component shown in Figure 4.14a has slightly higher values $\delta_{RT} = 0.92(3)$ mm/s near 300 K and at 700 K (if extrapolated) reaches $\delta \sim 0.6$ mm/s and seems to follow the SOD. The quadrupole splitting value is slightly lower at RT in comparison to TiO₂:H-RT, although if it is extrapolated up to 700 K it appears to be on the order of 1.7 mm/s, which is significantly larger than in the previous sample (see Figures 4.14b and 4.12b). The influence of hydrogenation on the area

fractions shows a steeper evolution of $\text{TiO}_2\text{:H-573 K}$ features, where the SL contributes only 11.2% of the spectral area (22.4% in the case of $\text{TiO}_2\text{:H-RT}$) at RT. Here, the fractions (D1 and SL) almost reach a parity at 500 K, afterwards the SL decreases steadily, which is different for the 573 K sample, where both components are stretch out for each other at 600 K. At this point, one may assume that the local atomic environment of D1 at RT is different to the one after the equivalent stage at 500 K (see Figure 4.12). Although Fe^{2+} components seem to be similar in pristine and after-hydrogenation samples near 300 K, the broadening of the D2 component remains alike to that in the $\text{TiO}_2\text{:H-RT}$ sample.

The hyperfine parameters change marginally after the hydrogenation treatment at 573 K. The D2 component shows only a small growth of $\delta_{RT} = 0.92(3)$ and decrease of $\Delta E_Q = 2.12(5)$ mm/s. The increase of quadrupole splitting for the hydrogenated samples shows that the electric local environment around probes has become more asymmetrical. Additional V_o and -OH bonds should increase the s -electron density at the nucleus, resulting in changes of isomer shift, which is reasonable since both act as shallow donors in TiO_2 even when H is isolated [24, 51, 147].

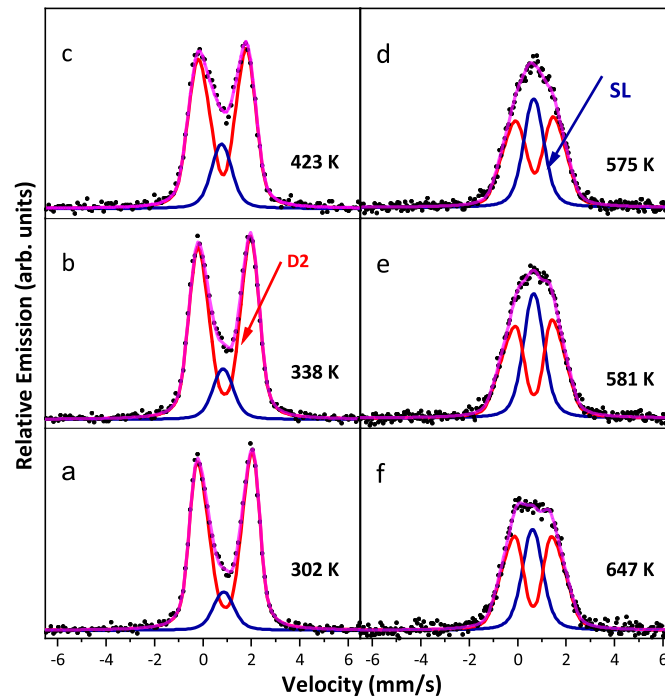


FIGURE 4.13: ^{57}Fe emission Mössbauer spectra obtained at the temperatures indicated after implantation of ^{57}Mn into $\text{TiO}_2\text{:H-573}$.

The nature of the SL and the absence of Fe^{3+} require more attention. To investigate this, one may need to study the local atomic environment further. At this point, the results can be explained in terms of charge transfer. In the current system, this transfer can be invoked by: 1) high amount of V_o in the upper layers, which supports the Fe^{2+} state as well as the presence of Ti^{2+} and Ti^{3+} , as detected by XPS measurements; 2) hydrogen bonds -OH; 3) both combined. Considering more than one degree of freedom, the annealing

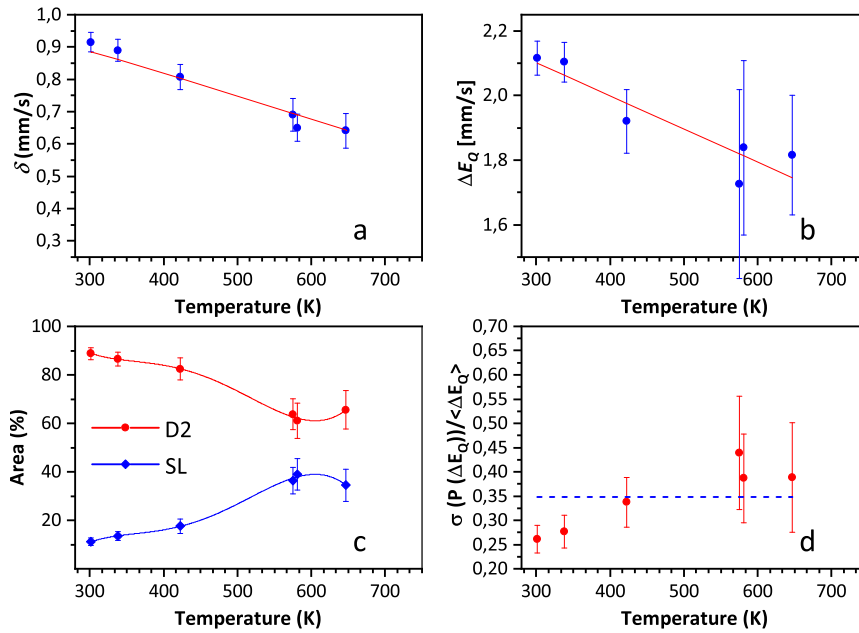


FIGURE 4.14: Temperature dependence of hyperfine parameters of Fe²⁺ (D2) for TiO₂:H-573. (a) Average isomer shift. The solid line is a fit to the SOD shift. (b) Average quadrupole splitting. (c) Area fractions of the spectral components of the spectra in Figure 4.13. (d) Relative standard deviation of the quadrupole splitting distribution function.

behaviour of the treated samples could be slightly ambiguous. As V_o undergo changes at low temperatures (at 360 K, I focus on point 2) hydrogen bonds - OH. On the grounds of a few experimental studies on metal oxides the hydrogen impurities are expected to be in several forms [60, 178]. By and large, it is energetically favourable for hydrogen to occupy two states in the bulk with different mobilities (i.e., activation energy). One form has a covalent bond to an oxygen atom (H_C^\bullet , placed perpendicular to c -axis), while the other behaves as a deep metastable interstitial (H_I^\bullet) or/and bound weakly via longer bonds to more than one neighbouring oxygen atom [54]. According to previous studies the charge state of H_I^\bullet remains to be unknown but is often assumed to be positive [179]. Results of another metal oxide WO₃ have shown that upon annealing hydrogen which is weakly bound (or free) can leave as H₂, whereas -OH leaves in the form of water [60]. The lower hydrogen concentration is, the higher energy is needed (the jumping frequency lowers). A recent IR absorption study on anatase has revealed that the barrier energy for hydrogen motion is beyond 0.9 eV, which is two times higher than that for rutile (0.53 eV) [180]. Thus, hydrogen in rutile cannot be accumulated in high quantities. Therefore, it is likely stabilised by the nearest defects. Bearing this in mind, it can be assumed that in the current case a possible synergistic configuration of a higher amount of hydrogen and vacancies is responsible for the observed annealing behaviour.

Due to the low activation energy, H_I^\bullet can already start to slowly diffuse out at RT. If the latter does not develop that swiftly, a hopping of hydrogen among equivalent oxygen neighbours could occur with high rates. A proton can be located vibrating near an oxygen atom, then it jumps over the shortest bond lengths (smaller activation energy) to another

oxygen and hops backwards to finalise the vibration near another oxygen [181]. The results show that implanted ^{57}Fe ions replace Ti ions in the lattice, where the hydrogen hopping to various oxygen atoms happens to be in the vicinity of the probes, thus affecting the electric-field gradient direction rapidly, on the time scale of the 14.4 keV lifetime of ^{57}Fe Mössbauer state. This can result in the occurrence of SL, which by all means is not a natural state in the tetragonal structure and can only be caused by dynamic processes. A similar tendency of H, for instance, was observed in SiO_2 [181].

With increasing temperature more atoms participate in the motion, which could result in a formation of an identical defect occupying a different lattice position (i.e diffusion of the species). Nonetheless, if the activation energy is not sufficient for breaking up a chemical bond, it may lead to a transition (or reorientation) between equivalent positions in the lattice [56]. For these reasons, one may need to consider that unbound-hydrogen has a significant impact on the electric field distribution around the probes. Studies performed by Lavrov *et al.* [150] have shown that anatase (TiO_2) doped with hydrogen is unstable against annealing at temperatures above 570 K. Combined stepping annealing and XPS analysis along with nuclear reaction analysis studies have shown that in rutile (TiO_2) hydrogen remains in the lattice up to 600 K, after which it depletes steeply [182]. Therefore, one may conclude that hydrogen movement in anatase consists primarily of two steps, with the second step superimposing on the first at higher temperatures. First, H_I^\bullet , which has a lower motion threshold, changes its orientation or moves throughout equivalent positions. This assertion can be justified by the eMS results in terms of the SL alteration with temperature. The eMS spectra obtained for the $\text{TiO}_2\text{:H-RT}$ sample shows no temperature dependence up to 350-400 K, whereas from ≈ 440 K a “jumping” of hydrogen throughout equivalent positions occurs. Second, when the activation energy is high enough, the H_C^\bullet covalent bond dissociation is triggered. As the speed of desorption is always dependent on the concentration gradient the recovery of areal fractions begins when most of the hydrogen is depleted from upper layers, thus explaining the “de-collapsing” of SL after ≈ 620 K.

The sample treated at 573 K exhibits a more perplexing scenario. Generally, it is similar to $\text{TiO}_2\text{:H-RT}$; however, the collapsing stage is evident throughout the high temperature ranges. The phenomena could be explained in terms of “hydrogen traps”. These traps are commonly formed when samples under study are with bulk defects, which in turn could be formed on a basis of V_o agglomeration. Once these bulk defects are formed, they prevent hydrogen atoms from swift diffusion and consequently from the early desorption [57, 182]. Besides, another scenario could take place. When two hydrogen interstitials form a single H_2 molecule, it could remain in the lattice under certain circumstances up to 973 K [183]. The gradual decrease in quadrupole splitting indicates a slow but steady recovery of defects. In this case it is fair to expect its development via the thermally-activated surface to the bulk diffusion of reduced Ti interstitials [184].

4.2.3.3 *Ab-initio* Calculations

To the best of my knowledge, there have been solely few attempts to perform density functional theory (DFT) calculations on anatase doped with Fe and only one study on changes in the electric field gradient (EFG) upon doping complemented with transmission Mössbauer measurements. For the comparison with calculations, only samples doped with relatively high amount of ^{57}Fe (2.8 and 5.4%) were used, calculations performed with one Fe atom in the supercell could miss out possible lattice distortions [185]. This mismatch between

theoretical approximations and experiments may cause a shift in the EFG that in fact could explain a typical 10-15% divergence of the experimental data from calculated results. Likewise, the obtained experimental data does not match well with the early published results by Rodríguez *et al.* [185] (FLAPW with LSDA and GGA was used). Therefore, it was necessary to perform our own calculations to check whether a closer match to our experimental results could be obtained.

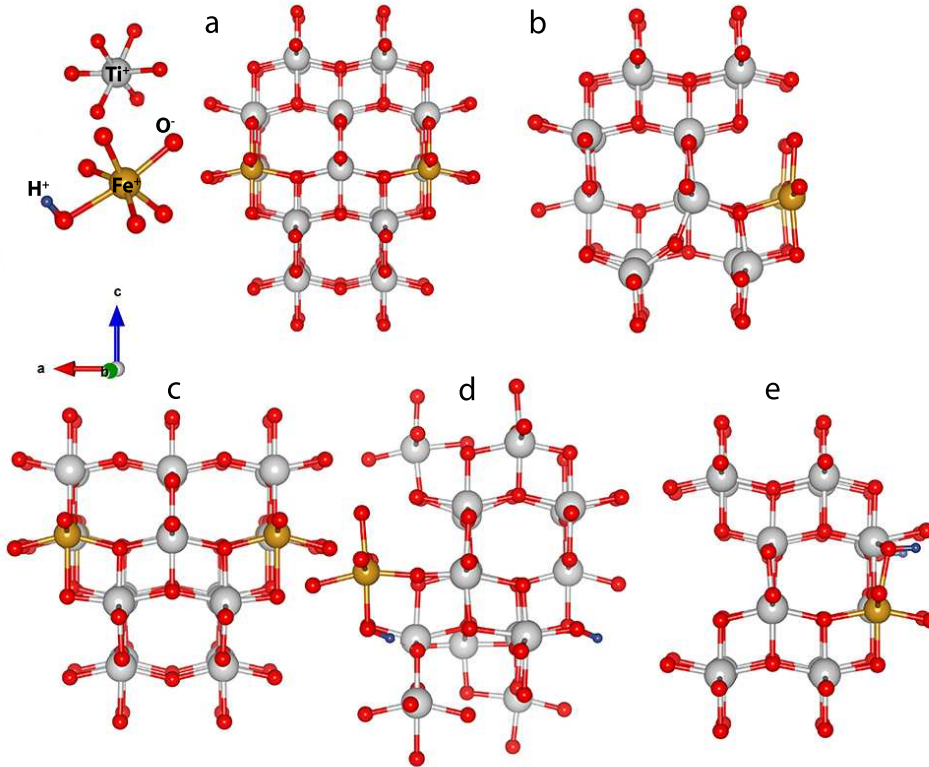


FIGURE 4.15: Possible TiO_2 configurations reconstructed using *ab-initio* calculations: (a) Fe:Ti; (b) Fe:Ti+ V_o equatorial; (c) Fe:Ti+ V_o equatorial nnn.; (d) Fe:Ti+OH#1; (e) Fe:Ti+OH#2.

To simulate isolated impurities, various approaches have been employed. Since our samples were implanted with dilute (ppm) amount of impurities, a $2 \times 2 \times 1$ supercell (SC) was utilised, taking into account that impurities did not interact with each other and structural relaxations were not affected. A tetragonal unit cell was featured with $a = b = 3.806 \text{ \AA}$ and $c = 9.724 \text{ \AA}$ constants taken from a 15 K neutron powder diffraction study [186]. In the current situation, it is important to predict and describe the charge state and structural, electronic, and hyperfine features of the impurity-host system. For that, calculations featuring various scenarios such as Fe being at the cationic site while surrounded with H and multiple configurations of equatorial/apical V_o around the Fe impurity and with added electrons were performed.

The *ab-initio* calculations were carried out employing the PAW method implemented in the VASP environment. The theoretical PBE exchange-correlation functional with $3 \times 3 \times 3$ k -point grids were used. Following the same strategy a SC with $a = b = 7.612 \text{ \AA}$ and $c =$

9.724 Å was constructed. For several cases the lattice parameters were optimised and only small differences were discovered in the results which are not presented here. In order to check the results, parameters for Fe:Ti and Fe:Ti(1 \bar{e}) with an additional electron by means of WIEN2K (17.1), using the accurate (linearised) augmented plane wave plus the local orbitals ((L)APW+lo) method were simultaneously calculated. The basis-set-size was defined by $K_{max} = 6/1.58 = 3.8$ arb.units⁻¹, and a $5 \times 5 \times 3$ k -points mesh. Besides, two more possible sources of error were tested: the size of the supercell and the use of the DFT+U approach to describe the d -electrons of Fe and Ti. The quadrupole splitting values was calculated based on $\Delta E_Q = 6|\nu_Q|\sqrt{1 + \eta^2/3}$ where the quadrupole coupling constant is given as follows: $\nu_Q = (ecQV_{zz})/[4I_e(2I_e - 1)E_0]$ with the asymmetry parameter $\eta = (V_{xx} - V_{yy})/V_{zz}$. The nuclear electric quadrupole moment, Q , represents the first excited state of ⁵⁷Fe, e is the elementary charge and V_{zz} is the EFG along the major axis (provides information on the symmetry of the electric field charge distribution) [187].

Table 4.3: Calculations obtained for TiO₂ anatase. Here d_{AV} is the mean length of Fe-O bonds (Å). V_{zz} is the largest component (given in 10²¹ V·m⁻²) and η is the asymmetry parameter of the EFG tensor. ΔE_Q and η are given in mm/s. U3 or U5 eV reflect when a charge is added to d -orbitals of Ti/Fe. Experimental data is for Fe²⁺ component taken at RT. δ_A is the isomer shift, based on the empirical model by Gunnlaugsson *et al.*. Mark \diamond is added for a $3 \times 3 \times 1$ SC. Equatorial and apical V_o - eq. and ap.; nnn stands for a next-nearest neighbour and m stands for a metastable state.

System:	d_{AV}	V_{zz}	η	ΔE_Q	δ_A
Fe:Ti \diamond	1.936	1.74	0	0.309	0.954
Fe:Ti+1 \bar{e} \diamond	2.012	2.17	0	0.385	1.025
Fe:Ti+OH#1 m.	2.010	-5.50	0.65	1.044	1.023
Fe:Ti+OH#2	2.031	-3.13	0.97	0.638	1.043
Fe:Ti+V _o ap.	2.017	-2.76	0.16	0.461	1.030
Fe:Ti+V _o eq.+U3	2.022	-7.25	0.37	1.318	1.035
Fe:Ti+V _o eq.+U5	2.026	-8.24	0.45	1.514	1.038
Fe:Ti+V _o nnn.	2.040	9.69	0.34	1.768	1.052
Fe:Ti+V _o eq.nnn. \diamond	1.994	-14.7	0.20	2.631	1.008
TiO ₂ Pristine _{exp} D0				1.98(1)	0.80(4)
TiO ₂ :H-RT _{exp} D1				2.19(6)	0.90(4)
TiO ₂ :H-RT _{exp} SL				-	0.72(2)
TiO ₂ :H-573K _{exp} D2				2.12(5)	0.92(3)
TiO ₂ :H-573K _{exp} SL				-	0.86(2)

Since eMS experiments were carried out with ⁵⁷Mn/Fe it was straightforward to consider the Fe:Ti configuration as the starting point. For this reason, a case where a Ti atom was substituted by Fe (see Figure 4.15a) and additionally Fe:Ti(1 \bar{e}) (checked with VASP & WIEN2K) was reconstructed first. Second, other calculations were implemented on the grounds of the Fe:Ti, additionally having hydrogen in two (OH#1) and (OH#2) configurations (Figures 4.15b-c). It was assumed that OH#1 could behave as H_T[•], while OH#2 could feature more robust bonding. Last but not least, Fe:Ti with either equatorial or apical V_o (Figures 4.15d-e) were performed. The calculated parameters are listed in Table 4.3. Besides the aforementioned calculations of the EFG, an empirical model was applied to determine

the Mössbauer isomer shifts in ionic and covalent binary compounds. The model predicts room temperature isomer shift values for Fe^{2+} in metal oxides. The empirical model relies mainly on the nearest-neighbour distances and Pauling electronegativity ($\Delta\chi_P < 2$) [97].

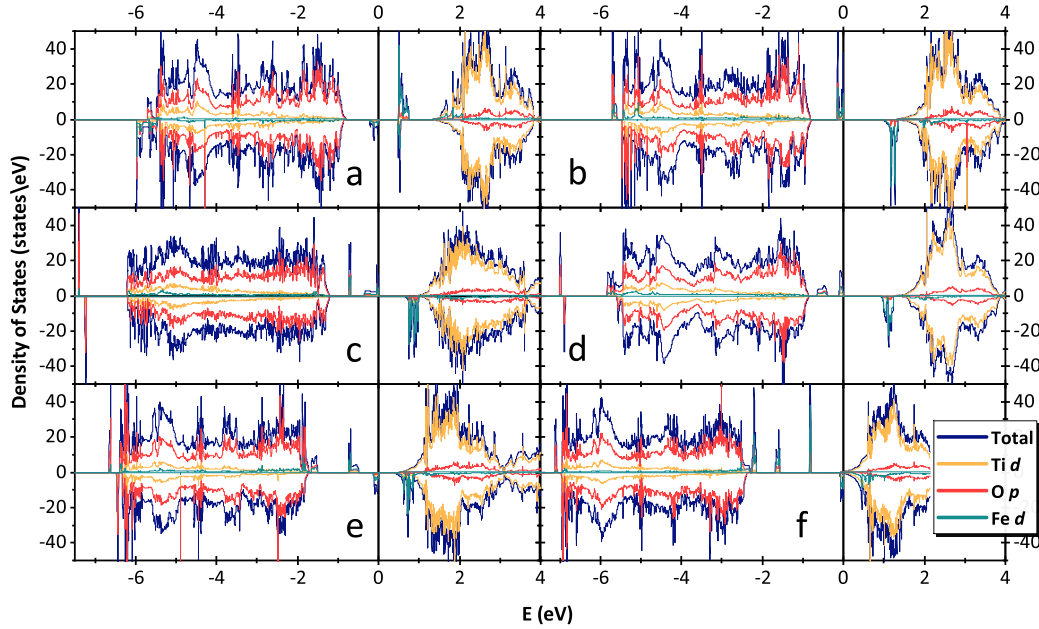


FIGURE 4.16: Densities of states for (a) Fe:Ti, (b) Fe:Ti+ $1\bar{e}$, (c) Fe:Ti+OH#1 m., (d) Fe:Ti+OH#2, (e) Fe:Ti+ V_o apical, (f) Fe:Ti+ V_o equatorial.

The performed calculations show that after relaxation local distortions affecting Fe:Ti bond lengths are anisotropic and higher than what have been observed with calculations performed by Rodríguez-Torres *et al.* [185], however slightly lower (1.94 Å) than the previously published XAFS data (Fe:Ti) (1.97 Å) [188]. The difference in bond lengths could be related to the displacement, which is symmetric in the PBE approximation. Furthermore, results for the calculated hyperfine parameters differ from ones obtained experimentally, similarly as in the previous study. On the basis of these calculations, one may ponder that a combined configuration of Fe:Ti+OH#2 with Fe:Ti+ V_o could result in close match with experimental data. In a charged supercell, the IS of a doublet likely remains within the range of Fe^{3+} . The trace of hydrogen breaks the symmetry of the EFG near the probe. Including V_o along with Fe doping in the calculation demonstrates that neither the high energetic stability nor results are close to the experimental data. Compared with the previous observation [185], the current experimental results are in better agreement with the calculated results of Fe-O next-nearest neighbour locations and QS match relatively close (1.77 with 1.98 mm/s, respectively) and the deviations are on order of 10-12%. Moreover, the performed calculations are done at 0 K and if there is a low crystal field splitting near the probe, then average values of the QS are used. Generally speaking, for Fe^{2+} there is always an additional electron in the system, which bears an extra part to the EFG and can jump between orbitals, that likely cancels out the QS which is evident in eMS results shown in Figures 4.12 and 4.14. Hence, V_o induce Fe^{2+} with reasonable QS values, while in the case

of -OH configurations they are characterised by lower QS values and likely are responsible for the SL.

The densities of states of the used configurations are shown in Figure 4.16. In most cases one finds semiconductors, where the valence band is mainly dominated by O p states, with insignificant hybridisation of Ti d states. However, the conduction band is almost completely given to Ti d states. One exception is the oxygen vacancy at the equatorial site, when the Fermi level moves to the bottom of the conduction band, thus turning the system metallic. The Fe impurity states are distributed in the valence band and localised in the peaks inside of the band-gap.

4.2.4 Conclusions

To summarise, hydrogenated anatase films show the presence of surface-bulk defects such as Ti-OH and V_o , which have a positive impact on light absorption and conductivity. ^{57}Fe emission Mössbauer spectroscopy following implantation of ^{57}Mn ($t_{1/2} = 1.5$ min) to a maximum local concentration of 10^{-3} at.% into pristine anatase films at various temperatures reveals two distinct annealing stages from RT up to 373 K and to 623 K. The first stage occurs due to a movement of vacancies and leaves the probes in a highly disturbed local atomic environment.

The second stage is induced by mutual annihilation of V_{Ti} and Ti_I . The hydrogenated samples show a different behaviour depending on the degree of hydrogenation. In both cases, there is no sign of Fe^{3+} , which is due to hydrogen being a shallow donor. Specifically, for the sample treated at RT, the interstitial hydrogen (with a small activation energy) starts hopping throughout equivalent positions around the probes even at RT. With increasing temperature there is a breakdown of the -OH bond and a further increase in temperature brings the additional amount of hydrogen into play. The latter manifests in eMS as the collapse of a doublet into a single broad line. Nonetheless, for the sample treated at 573 K, these two annealing stages overlap each other due to the bulk hydrogen traps. This is manifested as the collapsed eMS spectra at high temperatures because H_2 could be trapped in the bulk defects up to elevated temperatures. *Ab-initio* studies suggest that the observed eMS results are most likely related to a vacancy configuration near the probe ($\text{Fe}:\text{Ti}+V_o$ eq.nnn.°). Regarding the hydrogenated anatase, additional *ab-initio* studies are needed to reconstruct the position in the lattice that could yield the EFG values close to the experimental results.

4.3 Cd-H Pairs in Rutile

In the current section, an investigation of the electronic structure in hydrogenated rutile films is presented. The structure is probed by means of Time-Differential γ - γ Perturbed Angular Correlation spectroscopy with $^{111m}\text{Cd}/\text{Cd}$ isotope, implanted at ISOLDE/CERN. The measurements were conducted at 581 K as a function of hydrogenation temperature (temperature of the samples during hydrogenation). Despite the fact, that rutile single crystals show the presence of two local environments, the current pristine thin films sample had a single EFG. Upon various degrees of hydrogenation it underwent alterations, resulting in up to 3 different local surroundings, generally with high electric field gradient. Broad EFG distributions are likely due to randomly distributed point defects in the neighbourhood of Cd acceptors. Observed results suggest that hydrogenations at RT and 423 K are not sufficient enough to promote unique defect configurations, while in the range of 473-573 K the formation of specific defect configurations are observed. Therefore, one may assume that the formation Cd-defect complexes (Cd-H pairs) are temperature enhanced. At higher levels of hydrogenation (663 K), the sample becomes partly amorphous, which confines the reasonable usage of PAC. Complexes seem to be stable against annealing up to 581 K. This subsection has not been published/submitted yet.

4.3.1 Overview

Hydrogen is a well known impurity in semiconductors with a prominent impact on electrical, structural and optical properties. Intentional hydrogen incorporation (generally with plasma or implantation) allows to tune the band-gap and consequently improve solar light absorption caused by both reduction of ions and hydrogen doping [40]. Depending on a semiconductor type, hydrogen behaves differently. In wide-band-metal-oxides, hydrogen tends to bound to oxygen and can mainly act as an amphoteric impurity or as a donor [189]. The latter is the case for TiO_2 . In stable rutile, oxygen vacancies are also considered to contribute to the system. However, when there is an excess of electrons they tend to be localised at the Ti site, giving rise to a polaron formation. Moreover, a polaron remains favourable even when additional electrons are induced via a dopant [20, 190]. In the 70s an improvement of n -type conductivity was spotted after hydrogenation in TiO_2 . An interstitial hydrogen was suggested to form a single dative bond to an oxygen atom, where hydrogen was located in the open c channel of the crystal [191].

More recent studies with IR absorption spectroscopy have shown that hydrogen nature in metal oxides is far more complicated. It has been shown that hydrogen could feature several forms stable against low temperature annealing, and furthermore if it is stabilised by a defect nearby can remain in the lattice up to 1150 K [54, 182, 192, 193]. Stability of these complexes against other impacts raises questions. Under IR and electron irradiation diffusivity of hydrogen has significantly improved and is anisotropic, with the activation barrier remarkable lower in the c -direction [194, 195].

One of the subtle methods to probe structure, electronic properties and stability of impurities complexes in solids on the atomic scale is perturbed angular correlation spectroscopy. PAC is sensitive to the local electric field gradients present in the lattice near the probe atom. The EFG can be mainly described by the quadrupole coupling constant $\nu_Q = eQV_{zz}/\hbar$ (here Q is nuclear quadrupole moment and V_{zz} is the largest component of EFG tensor). In the current study ω_0 is employed instead, as the spin of Cd is specified $5/2^+$. More details

about the method can be found in sections 2.1 and 2.2. The method has been previously applied for studying acceptor complexes, passivation, influence of pressure and annealing on hydrogen bonds dissociation and impact of hydrogen on the electric field gradient in semiconductors (Si, GaP, InP, and InAs) [196]. In those studies hydrogen was introduced in several ways, including hydrogen plasma or low energy implantation. In the case of Si, for instance, hydrogen formed pairs with the majority of probes (up to 80%) and its incorporation in the lattice did not influence the axial asymmetry parameter, η , of the EFG, and only alterations in the observable frequencies demonstrated the changes [66]. Studies performed with another hyperfine interaction method - emission Mössbauer spectroscopy on hydrogen plasma treated anatase samples have shown that hydrogen complexes are likely to be featured in at least two main forms: interstitial (or weakly bounded with longer bonds) H_I^\bullet and hydrogen with a covalent bond to an oxygen atom H_C^\bullet . These complexes have different activation energy, and thus their thermal motion was triggered in two consequent steps: 1) H_I^\bullet moves through equivalent positions 2) H_C^\bullet , once activation energy is sufficient to break its bond (see section 4.2.3.2). In the case of highly doped and V_o -abundant samples both steps could overlap with each other. I performed several experiments with ^{111m}Cd on anatase samples and obtained no perturbations, as it happened in the case of $^{111}\text{Ag}/\text{Cd}$ isotope [122]. As pristine rutile behaves in a similar way as anatase does (see section 4.2.3.2), here I aim to spot ongoing changes in the electronic structure taking place during the first step of hydrogen dissociation [38, 182].

4.3.2 Experimental

TiO_2 thin films were prepared by radio frequency sputtering (LA 440S by VON ARDENNE) onto 1×1 cm Si substrates, utilising a ceramic TiO_2 target (99.9% FHR Anlagenbau, Germany). During the process, the sputtering power was kept at 210 W and the Ar flux was fixed at 80 sccm. The thickness of thin films was controlled with an ellipsometer (Sentech SE 801) and was in order of 500 nm. Prior to hydrogenation, the samples were annealed at 1073 K for 5 hours with slow cooling, to ensure their full crystallisation into rutile. Thereafter, the samples were treated in a chamber for plasma-enhanced hydrogenation treatment, where an inductively coupled plasma instrument (Plasma Lab 100 ICP-CVD, Oxford Instruments) was used. The H_2 plasma treatment was performed for 30 minutes in a broad temperature range (temperature of substrate) specifically at: room temperature (RT), 423, 473, 573 and 663 K. The ICP power was held at 3000 W, the chamber pressure at 3.5 Pa, and the H_2 flow rate at 50 sccm.

PAC experiments were carried out on a basis of 6-detector TDPAC spectrometer equipped with LaBr_3 detectors placed around a tubular furnace at 90° geometry with a decent time resolution (360 ps). Isotopes of $^{111m}\text{Cd}/\text{Cd}$ were implanted at room temperature into samples with energy of 30 keV and fluence in the order of 1.1×10^{11} at/cm² provided by the ISOLDE radioactive beam facility at CERN [98]. Since, the hydrogenation was done prior to the implantation the radiation-damage-recovery-annealings were performed during the measurements up to a certain extend. This decision was based on an early study of implantation damage in rutile where approximately 20% of damage was recovered near 500 K [197]. The chosen ^{111m}Cd isotope decays to ^{111}Cd and a cascade of 151-245 keV is released via isomeric transition, thus after-effects or/and chemical rearrangements can be excluded. SRIM calculations [107]) showed that the depth of implantation should not exceed 30 nm (average 15 nm). Quadrupole moment used for calculations of the EFG is 0.76(2) b [113].

X-ray diffraction patterns were recorded with a SIEMENS/BRUKER D 5000 X-ray diffraction using Cu-K α radiation at 40 kV and 40 mA, with a pristine sample being scanned from 20° to 80° with a step size of 0.02° in Grazing incidence.

4.3.3 Results and Discussion

4.3.3.1 Stability of Cd-H

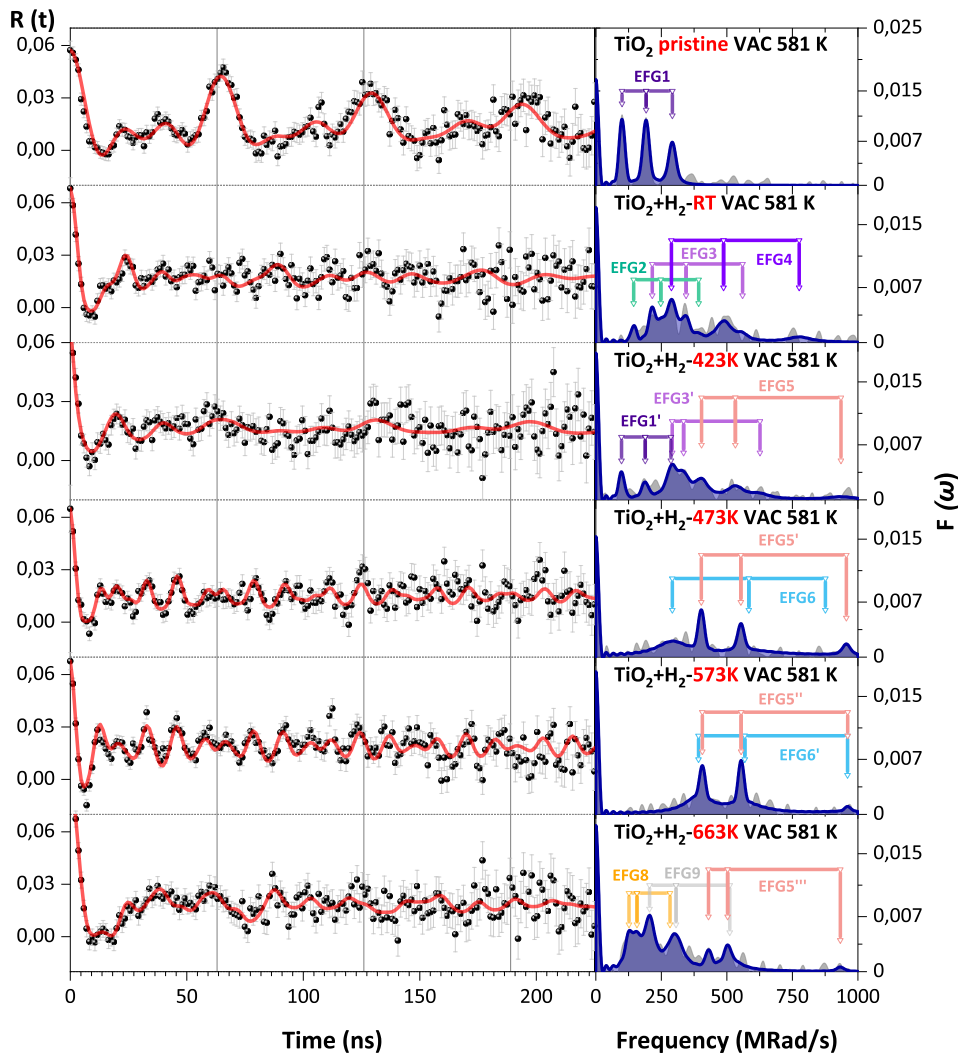


FIGURE 4.17: PAC spectra as a function of hydrogenation temperature with the corresponding Fourier transforms. Solid lines are the least-squares fit of the appropriate theoretical function to the experimental data.

Figure 4.17 shows the observable $R(t)$ spectra and their Fourier transforms, as measured at 581 K after implantation of ^{111m}Cd , for pristine and several TiO_2 samples hydrogenated

Table 4.4: $^{111m}\text{Cd}/\text{Cd}$ fitting parameters featuring main EFGs fractions. ω_0 is given in $\text{Mrad}\cdot\text{s}^{-1}$, δ and perc. are in % while V_{zz} numbers are presented in ($10^{21} \text{ V}\cdot\text{m}^{-2}$). EFG of the same origin are marked with colours.

State:	EFG:	Data:				
		perc.	ω_{0n}	η_{0n}	δ_{0n}	V_{zz}
Pristine	1	100	96.5(3)	0.19(2)	3.6(3)	5.57(2)
H ₂ -RT	2	8.4(5)	127.2(21)	0.37(8)	1.1(3)	7.35(2)
	3	27.7(46)	178.8(16)	0.46(2)	3.5(10)	10.32(3)
	4	63.9(71)	250.6(21)	0.39(1)	7.0(5)	14.49(4)
H ₂ -423K	5	38.2(75)	286.2(53)	0.68(2)	6.7(19)	16.52(5)
	1'	16.9(34)	94.7(18)	0.19(7)	4.2(8)	5.47(2)
	3'	44.9(41)	184.2(13)	0.83(2)	7.1(10)	10.63(2)
H ₂ -473K	5'	37.4(27)	295.3(10)	0.63(1)	1,3(1)	17.1(4)
	6	62.6(60)	292(14)	0.00	24.3(45)	16.86(9)
H ₂ -573K	5''	29.0(22)	296.2(6)	0.64(1)	0.6(1)	17.10(4)
	6'	71.1(24)	300.3(19)	0.57(2)	15.1(21)	17.34(4)
	5'''	9.6(32)	276.7(21)	0.81(1)	1.1(8)	15.98(4)
H ₂ -663K	7	66.2(71)	160.8(11)	0.54(2)	9.5(12)	9.28(3)
	8	24.2(46)	85.3(20)	0.75(3)	8,0(11)	4.93(2)

different temperatures. Table 4.4 summarises the fitting parameters of the main fractions of ^{111}Cd probe nuclei interacting with different EFG distributions.

Annealing at 581 K seems to be sufficient to recover most of the implantation damage of the pristine sample, where solely one fraction of a single triplet of frequencies, is seen to be present in the corresponding $R(t)$ Fourier spectrum. The corresponding $R(t)$ function has a well defined pattern, what is the characteristic of a single EFG/environment for the Cd atoms in TiO_2 , being only slightly damped as a function of time. The electric field gradient (EFG 1) resembles the values obtained on rutile [134, 198]. Absence of significant remaining implantation damage is evidenced by several factors. Firstly, one points the small damping of the $R(t)$ function that reveals a low density of defects, with an essentially defect free local environment. Secondly, the main frequency measured at this temperature $\omega_{01} = 96.52(3) \text{ Mrad}\cdot\text{s}^{-1}$ matches closely with previously reported values on rutile [198, 199] $\omega_0 = 98.5(2) \text{ Mrad}\cdot\text{s}^{-1}$.

The non-zero axially asymmetry parameter resembles results already measured at room temperature, although being slightly higher ($\eta = 0.19(2)$) than previously measured values on single crystals ($\eta = 0.7(1)$) [134, 198]. Based on these results, one may presume that most of atoms reside at the Ti substitutional site, in essentially defects-free environment.

After hydrogenation the spectra became remarkably complex and, without Fourier transform analysis it would be fairly challenging to distinguish amongst the variety of local environments/EFGs and their corresponding fractions. Upon hydrogenation treatment at RT, there is no evidence for EFG1. The spectrum was best fitted with the help of three EFG distributions, leading to a strongly damped $R(t)$ function, which is evidence for Cd atoms in a variety of local environments, characterised by EFG2, 3 and 4. One may point that it is known that the limit of solubility of deuterium in metal oxides is temperature dependent [200]; consequently, hydrogenation treatment at RT is likely not efficient to introduce

and promote hydrogen deeply into the lattice. Thus, a possible scenario, leading to the current PAC results in such sample, hints the existence of complex of hydrogen-related defects. These defects, upon interaction with the Cd probe, lead to a plethora of local environments, whilst Cd could still reside at or near the Ti sites. The actual matching of the ^{111m}Cd atoms distribution regarding the distribution of hydrogen is unknown. Most likely their relative distributions are not homogeneously overlapping.

At the limit of the experimental resolving power — statistics-wise, the assigned EFG2 contributes with small 8.4(5)% of a relatively undamped perturbation function (i.e., the signature of a relatively regular defect configuration). EFG3 contributes with 28(5) and has close V_{zz} and η EFG parameters such as EFG2, but demonstrating a much wider distribution, i.e., revealing the increase of defects density nearby. EFG4, being the principal contribution to the perturbation function (64(7)%), lastly characterises a fairly broad EFG distribution with a different characteristic V_{zz} and η . EFG4 likely evidences severe disorder induced during hydrogenation, which could not recover fast enough to be observed during the first ~ 1 hour of measurements performed at 581 K, when most of the statistics contribute to the TDPAC measurement.

It would be definitely difficult to say, without modelling of defects with theoretical calculations, what are the reasons of the observed EFGs? Regardless, it seems that although some preferential configurations of Cd related defects might prevail, these cannot be resolved due to the still high concentration of randomly distributed H atoms or H-related complex defects.

It is noteworthy that, the particular H-complex defect configurations formed during hydrogenation at RT, might be correlated with intrinsic defects in TiO_2 created during that process. We imply that the “likely” high density of poorly diffusing hydrogen atoms in the TiO_2 lattice induces the generation of intrinsic defects. This situation leads to the formation of complex hydrogen-lattice defects that are stable enough to remain observable during the TDPAC measurements performed at 581 K. However, as soon as the sample is heated during hydrogenation most of such complex defects will not predominate, e.g., after hydrogenation at 423 K, as observed during the following TDPAC experiments. This fact suggests that temperature activated hydrogenation with enhanced H-diffusion reduces the number of H-complex defects as well as H-lattice correlated defects.

Measurements performed on the sample hydrogenated at 423 K open a pathway for further discussions. The spectrum is analysed in terms of three broad EFG distributions, namely EFG1', EFG3' and EFG5. The corresponding $R(t)$ function has a slightly clearer and more developed shape, though still shows evidence for the broad EFG distributions. Seemingly, the current hydrogenation temperature allowed to bring back a small 17(3)% fraction of EFG1 (designated here as EFG1'), which is characterised with similar to EFG1 V_{zz} and η electric field gradient parameters.

This fraction demonstrates a relatively narrow EFG distribution. Next component, EFG3', may have the same nature as the one formed after hydrogenation at RT — EFG3. In comparison to EFG3, one may notice a growth of the principal contribution to the perturbation function from 28(5)% to 45(4)%, whilst V_{zz} and the wide distribution remain almost the same, $\delta_{03} = 3.5(1)\%$ and $\delta_{03'} = 7(1)\%$.

Apparently, the complex defects change and lead to more axially asymmetric EFGs signatures, as seen through the growth of $\eta_{03'}$ up to 0.83. EFG5, characterised with $V_{zz} = 16.52(5)^{21} \text{ V}\cdot\text{m}^{-2}$ and $\eta_{05} = 0.68(2)$, may be due to the further temperature development during hydrogenation of the defect configuration responsible for EFG4, with a similar wide

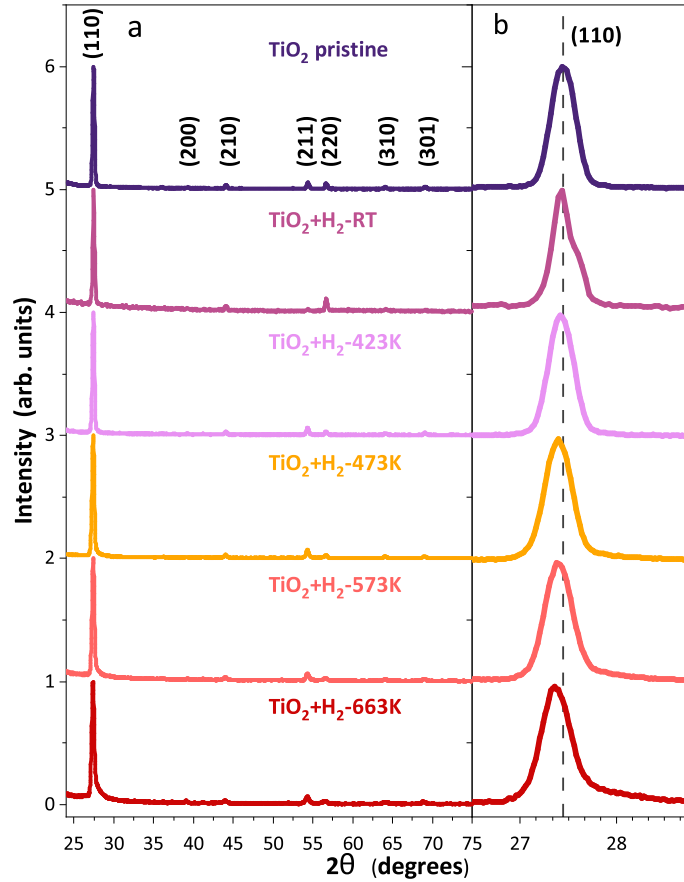


FIGURE 4.18: XRD patterns of hydrogenated rutile (a) and (b) the magnified (110) peak demonstrating a gradual shift.

EFG distribution. However, significant changes in the main frequency and axial asymmetry parameters, between EFG4 and EFG5 require that by no ways Cd is interacting with the same defect complex. At this point, one may argue that hydrogenation performed at 423 K is not entirely efficient to avoid the formation of still, e.g., H-lattice highly stable defects. Regardless, at this stage the material seems to be less damaged that further allowed a certain recuperation of implantation defects at relatively H-free zones for the implanted ^{111m}Cd probe atoms. Possibly, bestowed energy during hydrogenation, leading to higher dilution and less complex defects, allows hydrogen to interact more freely with the Cd acceptors in multiple ways, as might be seen in the case of samples hydrogenated at higher temperatures.

Upon hydrogenation at 473 K the corresponding $R(t)$ function became even more well defined and solely two different EFGs are needed for analysis (EFG5' and EFG6). One can notice that EFG5', with a surprisingly narrow distribution function contributing with 37(3)% to the $R(t)$, has central V_{zz} and $\eta_{05'}$ EFG parameters witch are quite close to the previously observed EFG5. Both EFG5' and EFG6 bear similar V_{zz} parameters: 17.0(4) and 16.9(9) $^{21} \text{V} \cdot \text{m}^{-2}$, respectively. While nevertheless, both the axial asymmetry parameter $\eta_{05'} = 0.63(1)$ differs from $\eta_{06} = 0$, as well as the relative attenuation parameter $\delta_{05'} =$

1.3(1)% and $\delta_{06} = 24(2)\%$. EFG6 is obviously a representative of a set of ^{111m}Cd probes at a particular local defect configuration with axial symmetry $\eta_{06}=0$, which is located in places with important density of randomly distributed defects. Even though it is not a trivial task to make anthologies, the spectral shape resembles results previously observed in other hydrogenated semiconductors (GaP:H, InP:H and InSb:H) [201]. Moreover, it has been argued that Cd-H pairs in these semiconductors generally have $\eta = 0$, which could hint on the origin of EFG6 observed at this temperature.

Following hydrogenation at 573 K, ^{111m}Cd implantation and subsequent measurement at 581 K, there is an obvious evidence for the remnants of EFG5', with a slightly decreased fraction, now designated as EFG5''. Undoubtedly, the defect interacting with the Cd atoms at the origin of EFG6, characterised by $V_{zz} = 16.9(9)^{21} \text{ V}\cdot\text{m}^{-2}$, $\eta_{06} = 0$ and $\delta_{06} = 24(4)\%$ is gone. A new predominant EFG6', which still has a wide distribution and characterised with $V_{zz} 17.3(4)^{21} \text{ V}\cdot\text{m}^{-2}$, $\eta_{06'} = 0.57(2)$ and $\delta_{06'} = 15(2)\%$ appears. Noteworthy is the fact that both Cd-defect configurations, EFG5'' and EFG6', evolve now in places with lower concentration of randomly distributed defects (see Table 4.4). From IR studies performed by Lavrov *et al*, one could think that hydrogen could remain in the lattice up to 1173K, if stabilised by an impurity or native defect in the local surroundings [192]. This might be only one factor explaining the lack of time dynamic effects observable in the R (t) spectra, due to H dynamics and trapping/de-trapping of H at the Cd probe atoms.

The presence of H-related defects and the further interactions with the Cd probe atoms do look highly stable at the measuring temperatures. These are probably complex defects, that act as deep traps for hydrogen and the Cd related probe atom, leading to no observable dynamics on the atomic scale under the present experimental conditions. Nonetheless, one can be convinced that partial implantation damage annealing is happening within the first half an hour of the measurement, the actual relevance of the diluted concentration of Cd and associated defects on the present set of experiments, looks very much irrelevant, regarding the hydrogenation (damage and doping) effects for all processing temperatures.

Hydrogenation at 663 K, implantation of ^{111m}Cd probes and subsequent measurement at 573 K presents quite unexpected results. Among the three different EFG distributions, therefore required to fit the data in the best feasible way, the only one that resembles an already measured EFG is EFG5'', although accounting for a reduced fraction of 10(3)%. At this point one may think that temperature of hydrogenation was too high, seriously degrading the sample's upper layers with no possible recovery (e.g., turning them slightly amorphous). Regardless, results obtained from GIXRD measurements show no evidence of such effect, and moreover demonstrate a shifting trend of the (110) reflection throughout treatments in the left-hand side.

The latter, was observed in ZnO doped with hydrogen and was attributed to hydrogen being incorporated into the the lattice [202]. Based on the observed frequencies one may assume that the family of observed EFG5 components are due to a combined complex, where one Cd atom is surrounded by the apical vacancy [198] and hydrogen. In order to perceive the exact location and chemical nature of the unique configuration one need to perform various DFT calculations. Preliminary calculations based on the approach described in section 4.1.3.3, with the same super cell parameters, but including a substitution of V_o with H were proved to be inadequate, employing the standard PAW method in vasp environment (see Figure 4.19). Therefore, performing large-scale quantum molecular dynamics simulations and and explore other possible defects configurations are two ways to further investigate the systems under the scope [203].

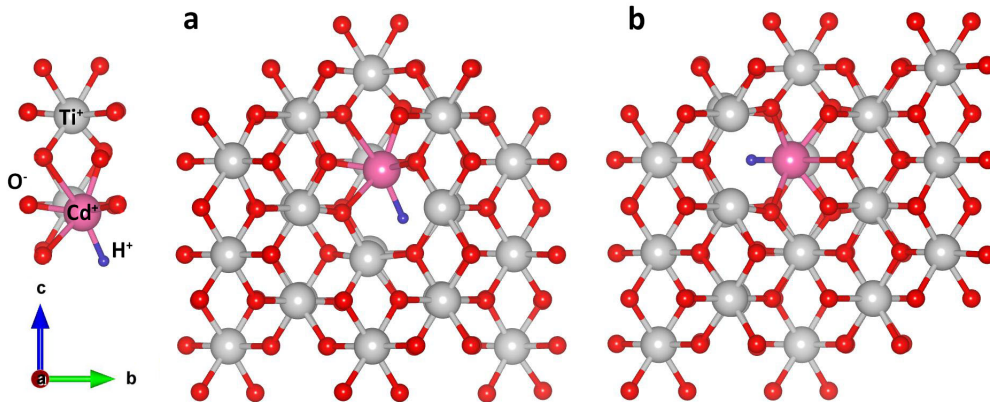


FIGURE 4.19: Two different Cd:Ti + V_o +H configurations in the $2 \times 2 \times 3$ rutile supercell. Here (a) stands for the case where V_o apical configuration is filled with hydrogen, while (b) represents V_o equatorial with placed hydrogen. Titanium and oxygen atoms are denoted as grey and red spheres, respectively, while pink and blue ones are cadmium and hydrogen.

4.3.4 Conclusions

First studies aiming to understand the building up of microscopic H-defect structures in TiO_2 thin films, upon various hydrogenation processes were done with the help of TD-PAC spectroscopy technique. ^{111m}Cd probe atoms were implanted in the pre-processed TiO_2 thin films and subsequent measurements were carried out at 581 K. The PAC results demonstrate that different and specific Cd-H-defects configuration complexes exist or vanish essentially depending on the pre-processing hydrogenation temperature. The low hydrogenation temperature range (423-573 K) studied in the present work, seems to be not sufficient to recover the TiO_2 local structure, keeping a high density of complex H-defects, maybe also interacting with intrinsic defects created during hydrogenation. When compared with the results obtained on hydrogenated anatase, rutile still demonstrates a different behaviour or, has the mechanism of dissociation which develops differently. While some defects show the corresponding EFG signatures, that could hint on the relevance of V_o and Cd-H pairing, there is a necessity of a strong and comprehensive research simulation programme. Supported by quantum molecular dynamics, looking for the stabilisation of complex H-defect structures and then combining it with an extensive usage of VASP and WIEN2K first principle simulations we could expect to find matching hyperfine structure (EFG) parameters that can be compared and validated with the present set of PAC results.

4.4 Influence of prolonged Hydrogenation on Titania

This section reports on the conversion electron Mössbauer spectroscopy studies, applied for studying of the electronic structure of prolonged hydrogenated TiO₂ thin films. Studies are performed at RT in a stepwise mode. Prior hydrogenation the films were co-sputtered (doped) with ⁵⁷Fe. Initial structure consisted mostly of high-spin Fe³⁺, which after hydrogenation demonstrates a gradual conversion into Fe²⁺. The conversion is accompanied with an occurrence of a magnetic sextet, resembling the one of α -Fe. This trend takes place up to 25-30 minutes of treatment, then a steady recovery occurs up to 125 minutes of treatment. Increase of the hydrogenation temperature from 573 K to 663 K suggest the similar parameters for Fe³⁺ as seen after 120 minutes of treatment. High temperature annealing applied after the hydrogenations for the structural oxidation and possible full recovery does not results in the pristine structure. The subsection has not been published/submitted yet.

4.4.1 Overview

Recently, hydrogenation of TiO₂-based materials in hydrogen atmosphere or plasma has received a remarkable attention [40, 146, 165]. The main reason for that is its positive influence on the light absorption and, consequently, better performance during photocatalytic water splitting [166]. Initially, performed in a way where samples were placed and annealed in hydrogen for a time span of several weeks, treatments with plasma turned out to be superior and allowed one to obtain same or even better results quicker. There is yet no sound explanation what is the reason behind additional gap states and improved light absorption and the reasons can be synergistic. When TiO₂ is treated in a reducing atmosphere it inevitable loses a certain amount of oxygen, thus forming several suboxide forms and phases such as TiO, Ti₂O₃, Ti₃O₅, Ti₄O₇ [29]. These suboxide can be responsible for the room temperature ferromagnetism, which has been ascribed to the metal oxides doped (i.e., with Fe) in dilute concentrations (so-called dilute magnetic semiconductors) [17, 204].

Historically, treatment of semiconductors in various plasma were applied for the chemical reduction (especially in C) and considered as an alternative route for the chloride-based Kroll process. None of these studies were able to result in a product which could be considered close to the metallic Ti though. Another application of various plasmas was aimed at the doping and was mostly applied to Si-based materials [205]. If samples were exposed for a prolonged time, a significant reduction of the upper layers would take place [206].

Mössbauer spectroscopy is often applied for studying the electronic structure behaviour in metal oxides and moreover in TiO₂-based materials. Seemingly, observed behaviour depends strongly on the dopant concentration. While there is just a handful of studies where dopants have been used in the ppm range and most of the studies have been performed where amount of dopant was in order of 1-5 at.%. Those studies, on the other hand, often seem to be not straightforward. Early studies performed by Stampfl *et al.* [207] on rutile TiO₂ doped with 1 wt.% of ⁵⁷Fe demonstrated solely the presence of Fe³⁺ (when annealed in O₂), while only Fe²⁺ was spotted after the same annealing in argon and hydrogen. It is often reported about the magnetic splitting seen at samples which contain up to 1 wt.% of transition metal dopant. This is generally accompanied with a blend of relaxation-blurred magnetic splitting and paramagnetic doublet configurations. A combined distribution of various relaxation periods for the paramagnetic relaxation could be responsible for this behaviour [208]. Coey *et al.* [209] applied CEMS for studying ferromagnetic behaviour in

rutile. It was discovered that both Fe^{2+} and Fe^{3+} were in the lattice, with area fractions varying depending on the Fe concentration. In this case Fe^{2+} was characterised with $\delta = 0.96$ mm/s and $\Delta E_Q = 2.11$ mm/s, whilst Fe^{3+} had $\delta = 0.40$ and $\Delta E_Q = 0.56$ mm/s. While all authors report on the presence of only high-spin Fe^{3+} and Fe^{2+} sites, there is information what upon certain conditions (elevated temperature) in rutile one could spot the intermediate and low-spin ($S=2$ and $S=0$) Fe^{2+} as well as Fe^{1+} [210].

Anatase was found to act similarly and the only difference at RT was found in bigger ΔE_Q values (1.1 mm/s (A) against 0.07 mm/s (R)) [211]. In the case of a rutile-anatase mixture, it was characterised with two high-spin Fe^{3+} components, where one had a near zero ΔE_Q while the other 0.7 mm/s. Rodríguez-Torres *et al.* [185] studied hyperfine structure of anatase doped up to 5.51 at.% and additionally performed *ab-initio* calculations. Based on a combined approach they ascribed Fe^{3+} ($\delta = 0.68$ mm/s and $\Delta E_Q = 0.36$ mm/s) as to being at the vicinity of one apical oxygen vacancy in the first coordination sphere.

Another fingerprint of TiO_2 materials doped with iron is a formation of Fe^{3+} clusters. These formations are fairly energetically favourable, since one V_o bears a double charge, whereas a Fe^{3+} ion substituting Ti^{4+} atom only a single negative charge. Uhm *et al.* [212] reported a component magnetically characterised with hyperfine field splitting of 33 T in TiO_2 doped with 4 wt.% of Fe. The authors claim the observance of Fe particles, which was additionally confirmed by TEM results.

Earlier in sections 4.2 and 4.3 we have studied several defects, which are formed during hydrogenation at certain temperatures and for a certain time, their thermal stability against annealing, pairs formation. However, it is yet to be ascertained what happens when samples are exposed to hydrogen plasma for a longer time.

4.4.2 Experimental

TiO_2 thin films were prepared in the same way as described in subsection 4.2.2.1. The thickness of thin films was controlled with an ellipsometer (Sentech SE 801) and was in order of 100 nm. Energy-dispersive X-ray spectroscopy showed that Fe content was in order of 1.8 at.%. Prior to hydrogenation, the sample was annealed at 813 K for 4 hours and cooled slowly. Final structure was checked with GIXRD and consisted of rutile with a minor contribution of anatase (approximately 10%). Thereafter, the samples were treated in a chamber for plasma-enhanced hydrogenation treatment, where an inductively coupled plasma instrument (Plasma Lab 100 ICP-CVD, Oxford Instruments) was used. The H_2 plasma treatment was performed stepwise in the following order 15, 25, 45, 95, 125 minutes (additively), while the sample was held at 573 K. Then, the same sample was exposed to the same hydrogenation procedure, while the substrate was held at 663 K for an additional half an hour. In all cases the ICP power was held at 3000 W, the chamber pressure at 3.5 Pa, and the H_2 flow rate at 50 sccm. After each of these treatment the sample was measured at CEMS (see section 3.2.3), with a conventional ^{57}Co source in the Rh matrix.

4.4.3 Results and Discussion

4.4.3.1 Stepwise Hydrogen Reduction

A series of variously hydrogenated TiO_2 spectra is shown in Figure 4.20. The following spectra were well evaluated with three components: two doublets and a magnetic sextet

by means of VINDA programme, while HAPPY SLOTH software was used for simultaneous analysis [88]. Derived hyperfine parameters are listed in Table 4.5.

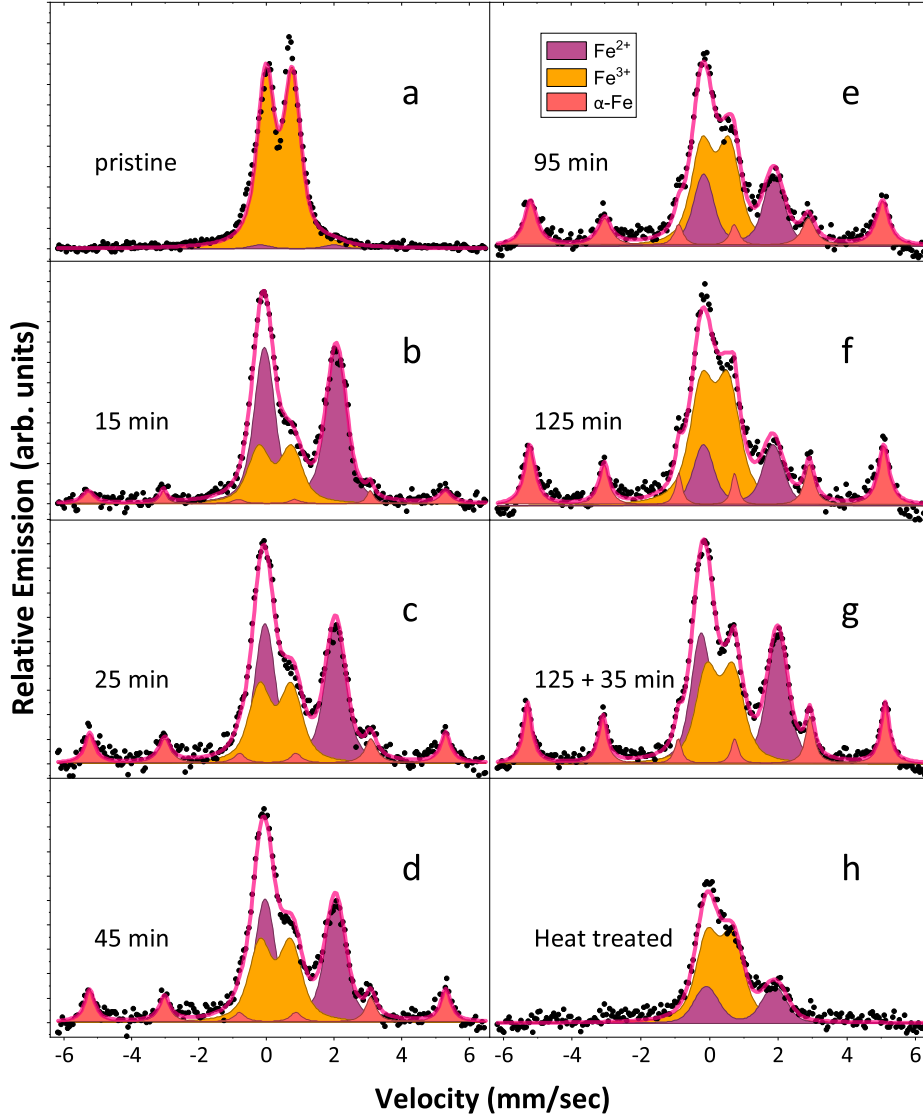


FIGURE 4.20: ^{57}Fe CEMS spectra with the simultaneous routine: (a) pristine, (b-f) hydrogenated at 573 K, (g) hydrogenated at 663 K and (h) annealed at 813 K.

Initially, the pristine sample demonstrates two contributions, as can be seen in Figure 4.20a. The fractions are assigned to Fe^{2+} and Fe^{3+} and characterised with $\delta = 0.96(3)$ mm/s, $\Delta E_Q = 2.2$ mm/s and with $\delta = 0.37$ mm/s, $\Delta E_Q = 0.78$ mm/s, respectively. Derived isomer shift parameters seem to be well in agreement with previously published CEMS and eMS data of Fe doped TiO_2 [38, 209], as in rutile Fe tends to adopt Fe^{3+} oxidation state. Higher ΔE_Q can be explained due to influence of the residual anatase [211].

Upon 15 minutes of hydrogenation the spectrum changed remarkably and a magnetic

Table 4.5: Derived hyperfine parameters for the hydrogenated spectra series. Here δ and ΔE_Q are given in mm/s, while B_{hf} is in T. Coloured cells correspond to hydrogenated states. Where error values are >0.01 is marked as such.

State:	Components:					
	Fe^{3+}		Fe^{2+}		$\alpha\text{-Fe}$	
	δ	ΔE_Q	δ	ΔE_Q	δ	B_{hf}
Pristine	0.37	0.78	0.96(3)	2.19	-	-
+H ₂ 15 min	0.26(1)	0.97(3)	1.00(1)	2.13(1)	0.005	32.72(17)
+H ₂ 25 min	0.27(1)	0.93(3)	1.00(1)	2.09(1)	0.034	32.60(8)
+H ₂ 45 min	0.26(1)	0.91(3)	1.00(1)	2.08(1)	0.032	32.62(8)
+H ₂ 95 min	0.28	0.80(2)	0.97	2.08	0.012	32.24(1)
+H ₂ 125 min	0.27(1)	0.78(2)	0.95(2)	2.04(3)	0.021	32.41(5)
+H ₂ 125+ 35 min [663 K]	0.41(1)	0.78(2)	0.99(1)	2.26(1)	0.001	32.76(3)
Heat treated [813 K]	0.31(1)	0.74(2)	0.92(2)	2.00(4)	-	-

sextet appeared. Hyperfine parameters of the sextet resemble such of pure $\alpha\text{-Fe}$ with $\delta = 0$ mm/s and $B_{\text{hf}} = 33$ T. As it was assumed that no new components would appear, thus the spectra were evaluated simultaneously. Such approach allows one to follow precisely changes in the area fractions over a temperature range. Obtained results are shown in Figure 4.21. At the outset, the pristine sample consists mostly of Fe^{3+} component, with a minor contribution of Fe^{2+} . Presence of Fe^{2+} at this stage can be explained in terms of V_{O} , the natural donor defect in TiO_2 . Metal oxides receive additional amount of vacancies to maintain the charge compensation, when doped with a transition metal [208].

Over the course of hydrogenation the fraction behaviour varies, thus making it possible to earmark 2 stages. The first stage (coloured in pink in Figure 4.21) commences with hydrogenation, when the majority of Fe^{3+} is converted into Fe^{2+} . The last reaches approximately 60 %, while the former is thrice decreased. The current stage is accompanied by the appearance and further growth of $\alpha\text{-Fe}$. The growth of last continues up to 125 minutes of treatment. During the second stage (after 25-35 minutes, area coloured in violet) a reverse tendency occurs (oxidation) which shows a falling of Fe^{2+} , while the rest two components are increasing. After 125 minutes of treatment the $\alpha\text{-Fe}$ fraction surpasses Fe^{2+} . Hydrogenation of the same sample for additional 25 minutes resulted in a sudden drop of Fe^{3+} and $\alpha\text{-Fe}$. In order to check how the structure would recover and whether it would be possible to return the previous doublet to the sample again, a heat treatment procedure (similar to crystallisation annealing after sputtering) was performed. The structure demonstrates the signs of recovery, with no trace of $\alpha\text{-Fe}$ though, within the current statistics.

Derived hyperfine parameters of Fe^{3+} presented in Table 4.5 seem to be slightly affected by the treatments. It shows a drop of IS after the treatment and growth of the QS. Although, quadrupole splitting somewhat follows the tendency seen in Figure 4.21 where it was rising along with the increase of Fe^{2+} and decreasing thereafter and can be explained from the increasing site distortion point of view.

While one may find it reasonable to observe the first stage (which seems to be in agreement with results discussed in section 4.2), due to the reduction and hydrogen doping of the upper layers, the sudden arrival of the second stage is out of tune and requires further discussion. Wdowik *et al.* [210] reported on findings in single crystalline rutile, that it was

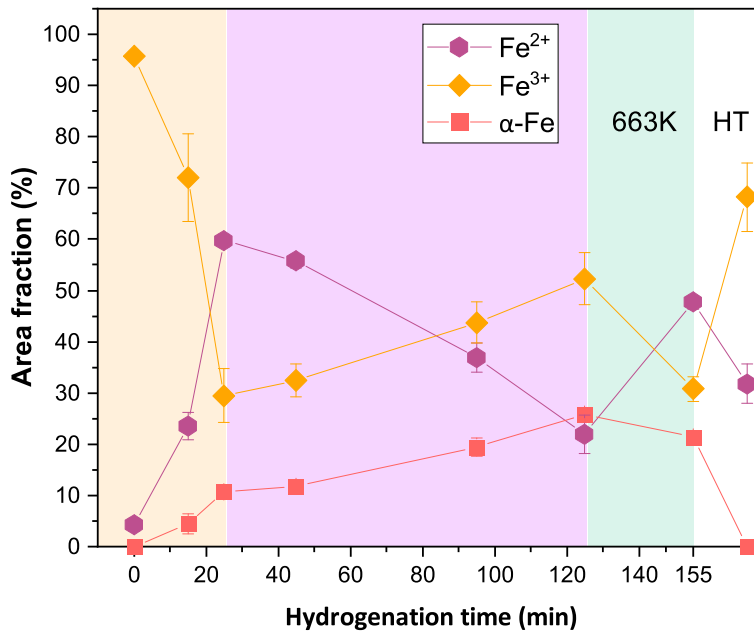


FIGURE 4.21: Area fractions obtained after a simultaneous fitting routine for the 573 K hydrogenated sample. There are two stages. The first stage (orange) demonstrates that the pristine sample is mainly characterised by Fe^{3+} which then starts to transform into Fe^{2+} during hydrogenation. While the second stage demonstrates a steady growth/recovery of Fe^{3+} . Blue area highlights the sample treated at 663 K. At this stage Fe^{2+} and Fe^{3+} behaviour resembles one seen after 30 of treatment. The white area represents the same sample annealed in air for 4 hours at 813 K and shows a vanishing of $\alpha\text{-Fe}$ and growth of Fe^{3+} . Points are connected with lines to highlight the dynamics.

possible to distinguish and assign intermediate and low-spin states of Fe^{2+} to be present in the system. At this point one may think of considering the transition of Fe^{2+} $S=2$ to $S=1$ or $S=0$ charge state (spin crossover) for their low values of IS. However, it is important to point out that in tetrahedral complexes the crystal field splitting energy is low, therefore, it is extremely rare that the crystal field splitting energy exceeds the electron pairing energy. As a consequence, electrons are rather to move up to the higher energy orbitals, than to pair [213], thus a transition to low or intermediate spins is very unlikely. Regardless, it is well known that ferrous low-spin compounds are characterised with high values of ΔE_Q , which does not seem to be the case here ($\Delta E_Q \approx 0.8$ mm/s). A more plausible assertion can be that severely damaged thin films are undergone to a dynamic recovery, which is generally triggered at 293 K and that the activation energy raises with plummeting of disorder density [197].

4.4.4 Conclusions

Studies reporting the effect of prolonged hydrogenation of TiO_2 films were performed by virtue of ^{57}Fe CEMS. The current work gives an outlook at the changes happening to the

hyperfine structure which was subjected to the various hydrogenation time. Based on the obtained results it is possible to separate two regions. At first, the pristine bears mostly Fe^{3+} oxidation state, which starts to transform into Fe^{2+} during the treatment. The process goes for 30-40 minutes, after which a recovery process is likely taking over, thus restoring partly Fe^{2+} . α -Fe is gradually growing in fraction during the treatment. Annealing of the sample at the crystallisation temperature for the same time in oxidising atmosphere does not recuperate the structure to its initial state.

A concept of a Mössbauer spectrometer based on the emission arrangement was first suggested shortly after the effect discovery [214]. Albeit, nothing has changed much since then and the majority of experimental set-ups in use, still rely on the samples doped either during preparation or when long lived probe nuclides are deposited electrolytically on desired materials. On the one hand, at ISOLDE, a different approach has been in use for several decades. In this particular case, a radioactive beam with a short-lived isotope of interest is employed for doping in small quantities (see section 3.2). With high yields of implantation a sample is measured within a dozen of minutes. On the other hand, the current state of the existing device is quite unreliable and lacks numerous important aspects. This design of the chamber puts significant limitations to the new types of experiments (such as under high applied magnetic fields and with light). Furthermore, the pumping procedure is carried out through a narrow collimator window of 3 mm, making a system evacuation time in order of 30 minutes (10^{-4} mbar), while continuously causing vibrations, thus affecting the experimental results. Since, the current facility puts limitations on precision of measurements a major replacement has been developed - *Emission Mössbauer Spectrometer from Ilmenau* (eMIL).

Several measures were taken to achieve the required goals:

1. The implantation chamber design was reworked, in order to make it possible to expose materials to light and induce changes in the hyperfine structure. From now on one may install various additional sections (extensions);
2. Flexible sample-holder was developed allowing to perform studies with various angles of exposure (ideally suited for on-line/off-line angular dependence measurements) up to elevated temperatures (up to 900 K, making studies of phase transition and defects annealing possible);
3. An automatised pumping station was designed and constructed;
4. Due to installation of completely new equipment the data acquisition, the axis control and the pumping station's control software were written anew.

The forthcoming sections issues an outlook of the hardware as well as software design.

5.1 Design Overview

Most of the absorption experiments are performed in transmission geometry. In this case one has the detector placed behind a thin absorber (sample) and this sample is being irradiated by radiation, coming from a radioactive source. Depending on the realisation, the emitted γ -rays energy is modulated by applying the Doppler effect either to the source or the absorber. It results in a spectrum recorded as a function of the relative velocity. On the other hand, in eMS experiments, the radioactive parent isotope is usually introduced in the samples of interest by doping or implantation (usually long-lived for off-line and short-lived for on-line experiments).

When dealing with the on-line experiments, isotopes are produced and implanted at facilities such as ISOLDE/CERN [100] and may take place simultaneously or time delayed (implant and measure). It is possible to highlight the in-beam experiments, in this group measurements occur on the time scale of Mössbauer state [215]. The main advantage of on-line studies is the amount of required isotope, where 10^{-4} at.% is sufficient (unlike in off-line experiments with a ^{57}Co or Sn source where one has to have at least 0.1 at.%). Such quantity and swift measuring time allow to measure without a risk of precipitation, therefore it becomes feasible to study impurities, isolated defects in diluted magnetic systems [204, 216, 217]. When the implantation is used to introduce the radioactive probe, the damage imparted on the host material invokes additional concern on the determination of the exact location of implanted atoms and their properties. Limit of the concentration for eMS studies is below the amorphisation threshold, which is in order of $10^{13} - 10^{14}$ ions/cm² depending on the material. When a sample is implanted with fluences below 10^{13} ions/cm², the implanted atom ceases the movement in amorphous zones (few nm across). These zones can be annealed (recrystallised) at relatively low temperatures, while amorphous layers remain stable up to elevated temperatures [218, 219]. Unless done on purpose, a common fluence applied in on-line eMS seldom goes above the amorphisation threshold.

The situation becomes even more tangled if during a decay to the ground state the recoil energy (e.g., $\langle E_R \rangle = 40$ eV for ^{57}Mn β^- decay) is sufficient enough to displace an atom to a random location in the lattice. However, it is possible to perform annealing in order to moderate the implantation damage.

The majority of the Mössbauer studies are based on the 14.4 keV γ -ray of ^{57}Fe , which is generally produced when ^{57}Mn or ^{57}Co isotopes decay into the the first excited state. With first attempts to perform aforementioned on-line experiments are running back to ISOLDE 3 in 1996. Equipment used for the measurements has been constantly upgraded in the last 20 years providing new possibilities for measurements (such as quenching experiments), but all these modifications have been bearing rather temporary character and the measurements could turn out fairly time consuming. Here, a newly developed emission Mössbauer spectrometer is presented. The spectrometer exploits new electronic solutions and provides a great flexibility toward its application along with a plug and play experience.

5.2 Hardware Set-up

Presently, a contemporary spectrometer relies mainly on software rather than hardware, for this reason a selection of unique elements is not longer needed [220]. The specialisation of hardware has become less diverse than in the case of analogue set-ups. Doubtless, an

attentive selection of components remains an important stage and impacts the overall performance. Figure 5.1 shows a schematic overview of the emission spectrometer's hardware set-up.

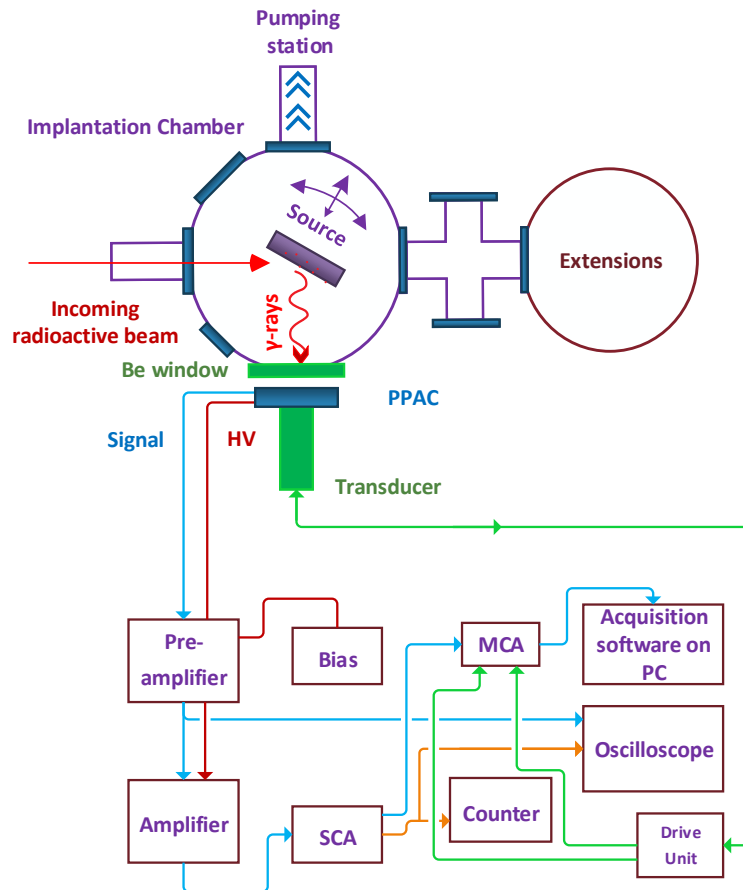


FIGURE 5.1: Schematic diagram of the implantation chamber and the electronics generally used in for eMS.

The scheme follows the classical principles common for Mössbauer spectroscopy [62, 221]. The main differences are coming through the fact that the source (sample) is kept inside the implantation chamber. The chamber is shown in Figure 5.2. As the sample is kept inside the chamber, it imposes limitations on the chamber design. Once the beam, coming from the UC_2 target, has reached the collimator at the chamber entrance (more details can be found in section 3.2) it hits the sample. The procedure of the ion implantation is performed at the incident angle of $\theta_I = 30^\circ$, whilst measured at $\theta_M = 60^\circ$ relative to the sample surface normal. Due to this special design the detector can only be installed on the transducer outside the chamber. More details are given in section 3.2.

For measurements in such conditions a detector with a rapid response is of big use. Gas filled detectors (which are also in use all over experimental nuclear physics) have been used since the 60s. An appropriate gas (often it is vaporised C_3H_6O) becomes ionised, when the ionising radiation interacts with it. Then, a detector produces an energy-dependent

electrical signal which comes from charged particles. One of the most popular detectors in the field of nuclear experimental physics is Parallel Plate Avalanche Counter (PPAC). The detector consists of two parallel thin electrode films separated by several mm. When a needed voltage corresponding to several hundreds of volts per millimetre is applied between the anodes and cathodes (in this case one plate is made from ^{57}Fe), ionised electrons from incident heavy ions immediately cause an electron avalanche. Unlike gas-flow proportional counters PPAC reveals larger signal-to-background ratio, swifter time response (10^{-9} s) and is simpler from the construction point of view [222]. It is important to stress on the fact that the current detector for eMIL was developed and assembled at Aarhus University, Denmark.

5.2.1 Chamber Unit

The chamber unit is based on a special 316LN ESR steel tubular chamber ($\varnothing=100$ mm). Use of 316LN ESR steel provides very low magnetic permeability and can withstand harmful impact of corrosion. All the rest CF and KF flanges, crosses are made of 316L steel.

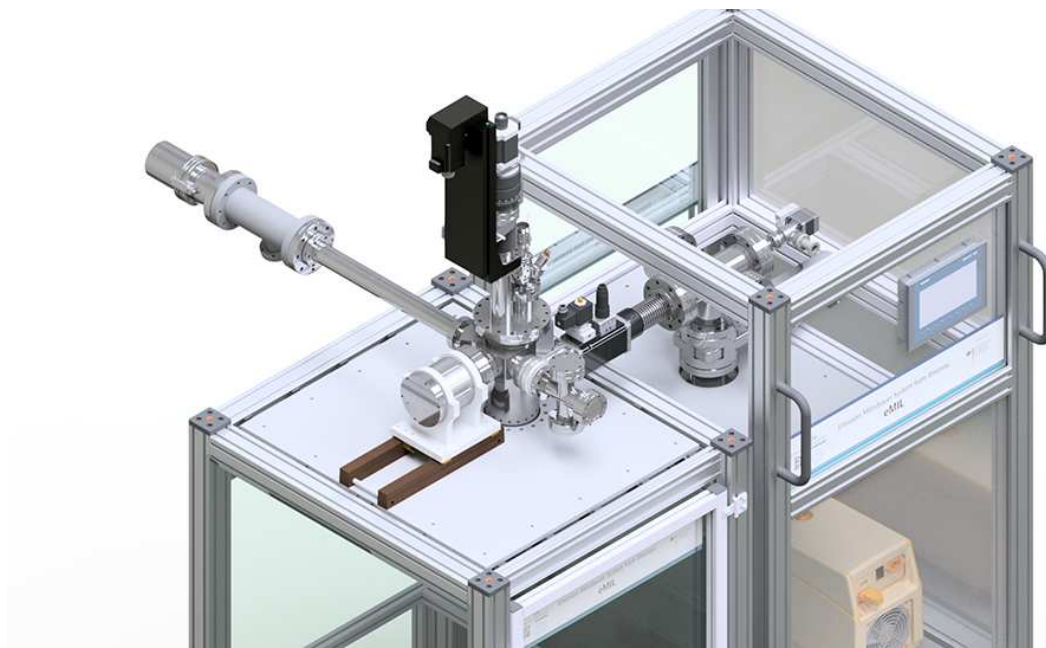


FIGURE 5.2: Picture of the implantation chamber with the PPAC detector mounted on the transducer. The chamber is plugged to the pumping unit via a soft bellow, the last is used in order to minimise harmful vibrations originating from the pumps.

The blueprints of the chamber (as well as hot-lid, with corresponding sample holder) is presented in Appendix A. 60 mm Al-profiles, on which the unit is built, ensure both sufficient reliability and provide opportunities to alter the set-up in the future. Beneath the chamber is a unit compartment, which has a heater controller module (Tectra HC 3500) plugged directly to the button heaters on the hot-lid via a 9 pins D-sub plug. The lid has 4 K-type thermocouples and 8 Cu electrodes to power up the heaters. The heaters are certified

to be within $\pm 5^\circ$ deviation, however in order to be on the safe side the thermocouples are additionally installed. Isolation is ensured by the ceramic fish bones. Additional ceramic crosspieces are placed among sample slots.

A remarkable flexibility of the set-up is achieved by virtue of so-called lids (or sample-holders). At the moment there is solely one lid available. The lid is built on a custom CF100 (M6) flange with 2 CF40 ports. One CF40 flange is for a manipulation system (2 stepping motors PKP268MD28B by Oriental Motor mounted on Z and Y stages D 40-150 S2 and LD40- 150S by VAb), which allows samples to be moved along Z and Y positions. While the second port is for the electrical feedthroughs and K-type thermocouples. The

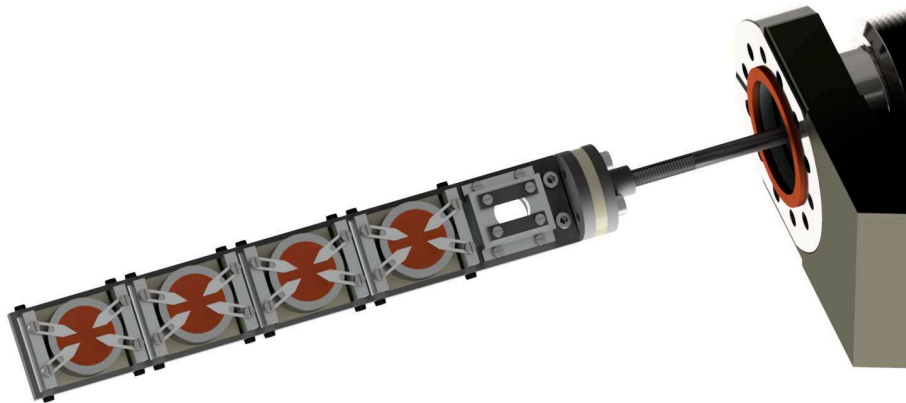


FIGURE 5.3: Illustration of the sample holder. There are four 1 inch (2.54 cm) button heaters mounted on ceramic substrates on separate beds (cells). Position of each sample can be adjusted by clamps, while the clamps are placed in a special way in order to minimise heat transfer to the other button heaters. Additional position is provided to a permanent α -Fe foil, for the calibration reasons. Thermocouples are plugged in through the connecting stems of heaters (underneath).

current design permits 4 samples to be measured without a need of breaking the vacuum in a temperature range from 300 to 1100 K. The latter is achieved with a special design and utilisation of button-heaters. The heaters are made from pyrolytic boron nitride and pyrolytic graphite (by HeatWave Labs). An additional spot is provided to a 5th sample, which can be a α -Fe foil. The current sample holder is shown in Figure 5.3.

The rotation (Z-axis) can be employed for the determination of the angular dependence of the collected spectrum. In a general case, an online measurement (implanting and measuring) is being taken for 4-5 minutes at $\theta_I = 30^\circ$ ($\theta_M = 60^\circ$). After this, the implantation is stopped and the sample is rotated in a way it is placed parallel to the detector. At this point the radiation during the decay is being collected for the same amount of time. Depending on the isotope the whole procedure can be repeated several times as a measure to improve the statistics. At this point, further expansions (cryogenic, magnetic and chemical measurements) can be easily mounted on another lid, fed through the bottom flange or through the cross placed on the axis of the beam (see Figures 5.1 and 5.2). Besides, on top of the CF

flange (placed on the cross in front of the chamber, see Figure 5.7) there is a Faraday cap (feedback of the beam). The remote control is realised via Arduino Uno Rev3, coupled with a pair of CNC single axis routers 3A TB6560. An electric scheme of the drives connection is shown in Figure 5.4. The drives are powered by a 12 V DC power supply.

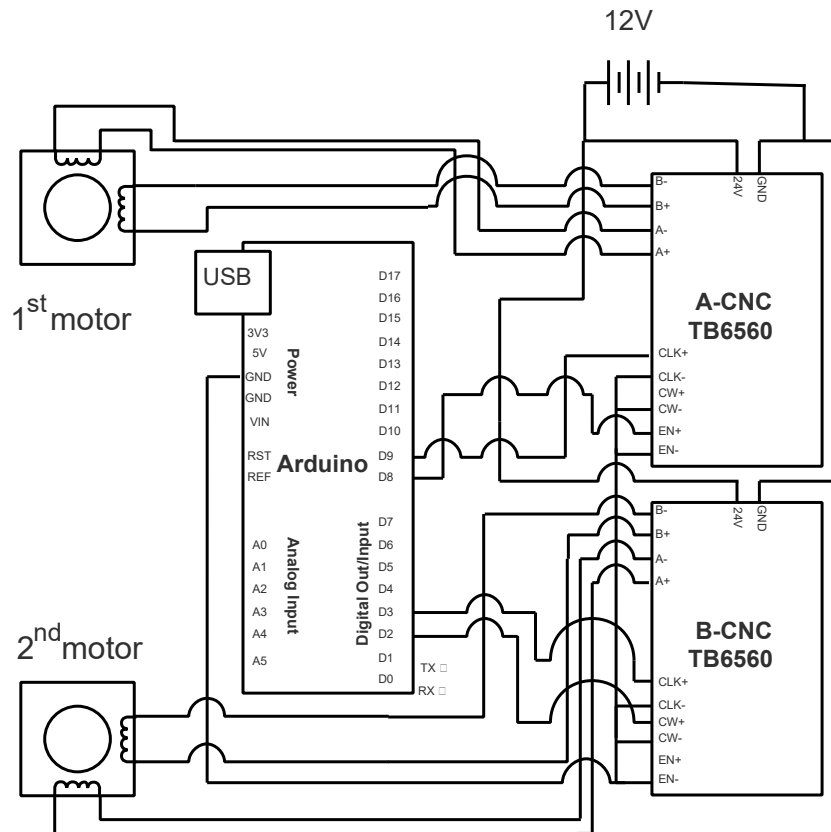


FIGURE 5.4: Schematic of the Y and Z drives control via Arduino Uno Rev3 and two CNC single routers TB6560.

5.2.2 Electronic Rack

During a measurement all radiation comes from a sample through a CF40 window placed on a side of the chamber and becomes collected by a PPAC detector which is placed on a MVT-1000 transducer (Wissel GmbH) relative to the incoming beam (at 90°). The transducer can reach velocities of far more than 1000 mm/s with a high linearity ($\pm 0.5\%$) in triangular and sinusoidal modes.

Here, the transducer is employed in a constant acceleration mode. In order to remove the high energetic electrons emitted during the β^- decay a Beryllium window is placed on the CF40 flange of the implantation chamber. This Beryllium filter effectively blocks high energy electrons, while allows γ -radiation to pass with approximate transmission of 90%. It is directly connected to a 142PC pre-amplifier (up to 3 kV) input by Ortec. The incoming signal is being transferred to both an amplifier and an oscilloscope. The last is used for



FIGURE 5.5: Photo of the developed electronic rack. The flight case includes a NIM crate with data acquisition modules, computer, oscilloscope, bias.

the adjusting of pulses height and amplitude. The signal is amplified and forwarded to the single channel analyser (590A amplifier combined with timing single channel analyser or SCA, Ortec). Output of the single channel analyser is connected to a counter unit. It is of big importance to control the pulses' shape as well as the count-rate. Any peculiar behaviour may hint on possible vacuum leaks, sample absence etc. Furthermore, the signal from SCA is transmitted to a Multi Channel Analyser (MCA), which allows multichannel scaling data acquisition (MCA4, by FASTComTech). MCA additionally collects information from the transducer (the start and channel advance signals). After the evaluation process the MCA transfers the signal to a PC. All data exchange with the PC and PLC is carried out via both RS-485 and usb connections (see section 5.2.4). Power supply is given via type C 230 rectangular plugs (DIN EN 175301-803). The system does not use any LEMO plugs and based solely on RG-58/U coaxial cables. Currently, the PC is built on quad-core i7 6700 3.40 Ghz with 32 Gb of RAM. All modules (omitting MCA) are powered by NIM8301 (CAEN). The only exception is the pre-amplifier, which is powered by CAEN N1471 four channel high voltage supply. The complete electronic rack is shown in Figure 5.5. Computer equipment and electronic units are contained in a music case for easy transportability.

5.2.3 Pumping Unit

A pumping unit is a separate part of eMIL. Due to safety reasons (i.e., one cannot open the target line when the pressure is insufficiently low) it has been entirely automatised. At the moment it consists of a fore-pump (roots pump by Pfeiffer ACP15), turbo pump (Pfeiffer HiPace 300) and 5 valve gates and angle valves (by VAT), Pfeiffer RPT 200 and CPT 200 gauges all controlled by RS-485 serial communication (industrial M8, M12 connectors) with Siemens Simatic 1212C (with a communication board SB1241RS485). This combination provides a robust base for establishing a point-to-point communication via RS-485 among nodes. Besides a PC control a HMI (Siemens Simatic KTP700) is placed on a side of the unit. Pumping scheme is shown Figure 5.6.

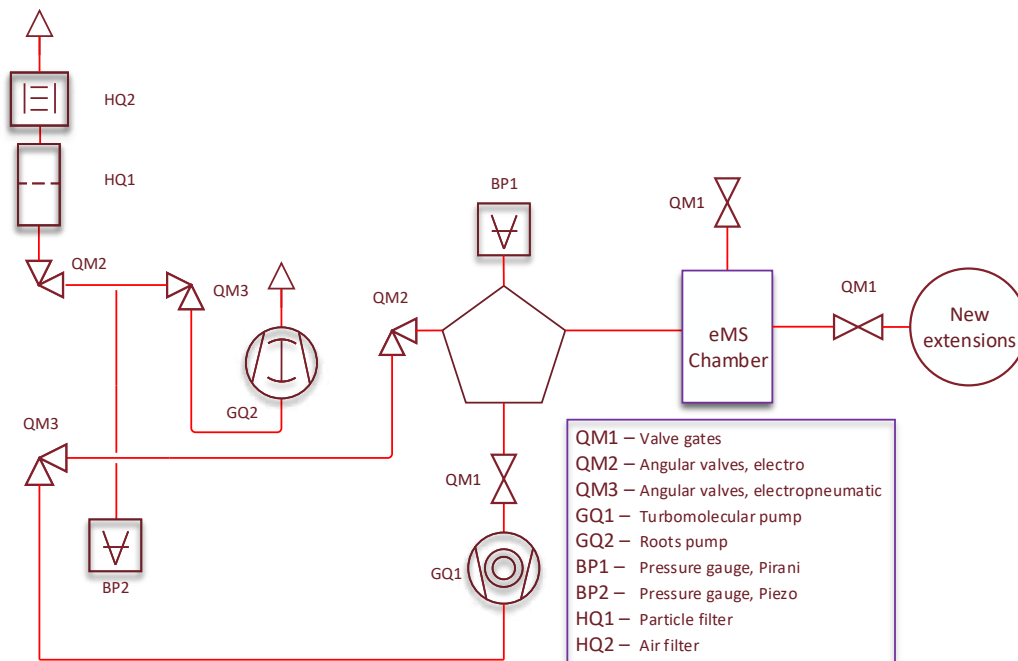


FIGURE 5.6: Circuit diagrams of eMIL's vacuum systems. The used symbols were picked in accordance with DIN ISO 1219 and DIN 28401, as appropriate.

Without additional alignments one can directly plug the chamber to the GLM branch and start experiments. Bottom part of the chamber is covered by a special lid, which allows to plug electro conductivity inputs, can be replaced by an ion pump or just a blind flange.

When the implantation chamber was devised we had to take into account numerous factors. On the one hand, most of them were attempts to overcome the limitations one came across before, while flexibility and expanding of applications were prioritised. This turned out in a bigger chamber, with a Beryllium window which permits use of 2 PPAC detectors, pumping coming from the pumping station and an additional port for light experiments. The light port is inspired by the fact that one may see changes in the quadrupole splitting and isomer shift, whilst a semiconductor sample is being irradiated by a light source (see Figure 5.7) [223].



FIGURE 5.7: Quartz window, for light exposure experiments located next to the beam (through the GLM chamber) on the left and the Beryllium window on the right.

5.2.4 Software

In order to make the measuring experience reliable and productive two main software applications were devised and programmed. The first is a LabView-based data acquisition part, which is the core of the eMIL and is responsible for data acquisition. The second is a Siemens Simatic application written for a PLC-controller. Simatic can be operated remotely from a PC or directly via human-machine-interface mounted on the pumping unit. The first part consists of numerous function-blocks. Here, the main inspiration was drawn from software of a Mössbauer spectrometer built on National Instruments' solutions - Nuclear DSP System [224]. The main difference here originates from a fact that our software does not obtain data directly from the MCA, but requires getting data from a hardware-dependent server programme (FASTComTech, MPant.EXE). This limitation is imposed by the closed code of FASTCom's FPGA. For this reason the starting procedure requires the MPant-daemon to be run first.

In the main menu the LabView programme multiple options are available. Central in the window it shows a graph with a measured spectrum with four functions: the First P. filter, Fold, Part/Shift and Rotate. The function First P. filter is rather practical in its purpose. Due to hardware constraints the first two data points tend to lag behind distorting the spectrum. The two first data points are therefore when the filter is switched on overwritten with the third data point. The other options, bear mostly complementary character allowing to the spectra to be generally transformed. When Fold is on the option Shift allows the two parts of the folded spectrum to be shifted in relation to each other. When Fold is off, the function Part allows the user to chose to see the Descending part, Ascending part or the whole unfolded spectrum. Additionally it is possible to rotate the spectra, i.e., reverse the velocity scale. On the other tab the count-rate over time is displayed.

When a new sample is about to be measured a user can define basic parameters on the sample (velocity range, XY-relative position, temperature of the button-heaters etc.). Once acquisition has started, it can be paused and then continued later on. Additionally, software allows to directly print spectra, read previously saved measurements and transform the output data (i.e., decrease number of channels). The second tab in the Viewer Pop-Up shows a graph with the count rate over time. It can be set to per second, per minute or per hour. The preferable output format is *.dat (along with *.txt and ms0), which is commonly used at ISOLDE/CERN along with VINDA programme [88]. The main window of the viewer is shown in Figure 5.8.

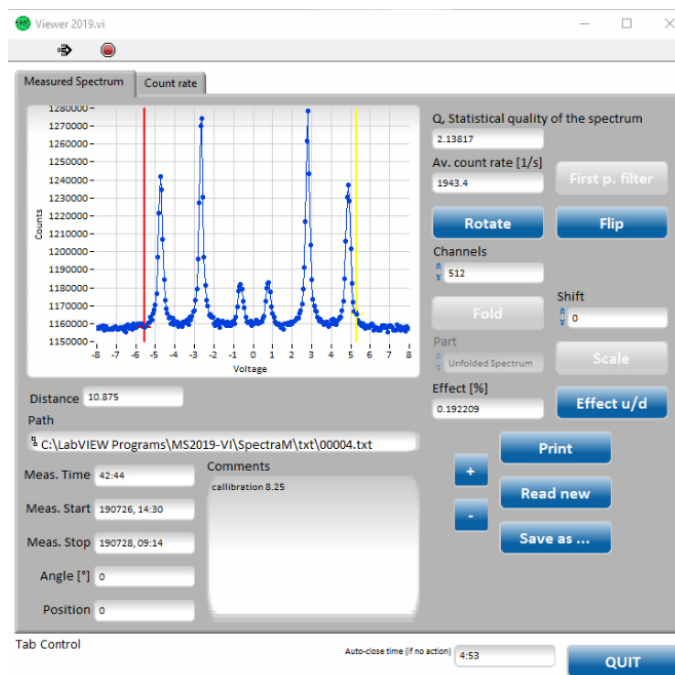


FIGURE 5.8: eMIL's spectra viewer window, with statistical information.

A user can easily control parameters such as voltage, current and observe changes in the real time of the HV-supply and NIM crate. Due to a special organisation of the data buffer, one has to keep an eye on the processing a queue in the real time (FIFO usage in runtime per cycle). The latter can be found under the monitoring button. Several auxiliary functions were additionally implemented. With this, it becomes feasible to estimate spectral quality (Q-factor). The statistical quality of a measured Mössbauer spectrum is quantified as follows:

$$Q = \frac{\varepsilon^2}{\varepsilon + 2} N_{\infty}, \quad (5.1)$$

here ε stands for the resonant effect:

$$\varepsilon = \frac{|N_{\infty} - N_0|}{N_{\infty}}, \quad (5.2)$$

at this point N_∞ is the total number of the counts and N_0 represents the number of counts at the maximum (minimum for transmission geometry) of a resonance peak.

In fact, the developed acquisition software has the flexibility to be used for Mössbauer spectroscopy in all transmission, emission or backscattered geometries.

5.3 Future Updates

Due to aforementioned advantages of the system several new ways of development have been proposed. At the moment the set-up supports measurements from RT up to elevated, with a possibility to perform angular-dependent measurements and experiments under applied light irradiation. However, eMIL provides a solid ground for additional modifications. One of the ways to improve data acquisition, for instance, is an installation of the second PPAC detector. Two detectors could significantly boost the data collection time. The bottom flange can serve as the base for a sputtering DC source, if samples are going to be treated by plasma. In order to make the system more reliable in terms of temperatures and changes taking place in the lattice is an installation on the bottom lid feedthroughs for electrical conductivity measurements. This is going to safely observe and check changes in materials such as V_2O_3 , where it may serve as a method to ensure the metal-to-insulator transition. For investigation of magnetic structure, there is an extension modular set-up in works (eMMA), which will allow studies with magnetic field up to 2.7 T (Vibrating Sample Magnetometer and possibility to measure Magneto-Optical Kerr Effect). eMMA devising is funded by Bundesministerium für Bildung und Forschung (BMBF) project 05K19SI1 and INTC (CERN) committee.

The growing demand of efficient and robust semiconductors for water splitting, water/air purification and solar cells has unfolded in a continues research and development of such materials. Among other approaches, the local structure modification of TiO_2 is being investigated. The most interesting scenario is to adjust the structure by tuning the local imperfections (e.g., vacancies, interstitials, defect complexes, fine doping). But the fact remains that it is not certain, how these defects behave and interact with each other on the atomic scale. The understanding of these behaviour-patterns may suggest the origin of the changes in the absorption, electronic and band structure.

The present dissertation attempts to answer the question above, and thus deals with the influence of these defects on the electronic structure and electric field gradients in anatase and rutile (TiO_2). Towards this target, along with standard characterisation techniques, four methods of the nuclear solid state physics have been employed: 1) $^{57}\text{Mn}/\text{Fe}$ emission Mössbauer spectroscopy; 2) ^{57}Fe conversion electron Mössbauer spectroscopy; 3) $^{111m}\text{Cd}/\text{Cd}$ time differential perturbed angular $\gamma - \gamma$ correlation spectroscopy; 4) Radio-tracer diffusion. The majority of the experimental studies are complemented with *ab-initio* calculations and standard experimental techniques. These results allow more reliable and broader interpretations of the physical basis behind every case.

Furthermore, for the future promising light excited Mössbauer experiments a contemporary and automatised setup for emission Mössbauer spectroscopy has been devised, built and optimised. The author additionally constructed a detector for CEMS studies of photocatalytic materials equipped with UV light sources, and an off-line Mössbauer LabView-based system on digital signal processing has been constructed.

The main conclusions of the current dissertation are listed as follows:

- Hyperfine interactions in monocrystalline rutile were probed with TDPAC as a function of temperature. Results show that the local structure is composed of two fractions (or electric filed gradients). The first EFG belongs to the Cd at Ti site configuration, which has slightly lower numbers with $^{111m}\text{Cd}/\text{Cd}$, than it was with $^{111}\text{Ag}/\text{Cd}$ isotope and is more asymmetric. Another EFG is characterised with high numbers of V_{zz} and demonstrates high distributions, where the last almost entirely disappear

near 900 K. Cd atoms demonstrate anisotropic migration, with two branches: near-surface and bulk. Diffusion develops approximately two orders of magnitude faster in the bulk. It is likely that the ion implantation leaves the surface layers disrupted therefore, making them a favourable place for defect accumulations, which can be hardly recovered after annealing. This assertion is fortified with *ab-initio* calculations, what indicate the presence of oxygen vacancies (apical) near the probes. Rising of temperature, however, decreases both the amount of the second EFG and its frequency, seemingly due to Cd diffusion into bulk.

- Hydrogenated anatase demonstrates the presence of surface-bulk defects such as Ti-OH and V_o , which have a positive impact on light absorption and conductivity. Emission Mössbauer studies reveal two distinct annealing stages:
 1. from RT up to 373 K,
 2. from 373 K to 623 K.

The first stage occurs due to a movement of vacancies and leave the probes in highly disturbed local atomic environment. The second stage is induced by mutual annihilation of V_{Ti} and Ti_I . The hydrogenated samples show a different behaviour depending on a degree of hydrogenation. In both cases there is no sign of Fe^{3+} which is due to hydrogen being a shallow donor. Specifically, for the sample treated at RT, the interstitial hydrogen (with a small activation energy) starts hopping throughout equivalent positions around the probes even at RT. With increasing temperature there is a breakdown of the -OH bond and with further increasing temperature brings the additional amount of hydrogen into play. The later manifests in eMS as the collapsing of a doublet into a broad single line. Nonetheless, for the sample treated at 573 K, these two annealing stages overlap each other due to the bulk hydrogen traps. This is manifested as the collapsed eMS spectra at high temperatures, for H_2 could be trapped in the bulk defects up to elevated temperatures. *Ab-initio* calculations suggest that the observed eMS results are most likely related to a vacancy configuration near the probe ($Fe:Ti+V_o$ eq.nnn.^o).

- The PAC results demonstrate that different and specific Cd-H defects configuration complexes exist or vanish essentially depending on the pre-processing hydrogenation temperature of rutile TiO_2 . The low hydrogenation temperature range (423-573 K) studied in the present work, seems to be not sufficient to recover the TiO_2 local structure, keeping a high density of complex H-defects, maybe also interacting with intrinsic defects created during hydrogenation. When compared with the results obtained on hydrogenated anatase, rutile still demonstrates a different behaviour or, has the mechanism of dissociation which develops differently. While some defects show the corresponding EFG signatures, that could hint on the relevance of V_o and Cd-H paring.
- When TiO_2 is exposed to the hydrogenation treatment for a continuous period of time the electronic structure demonstrates a peculiar conduct. Based on the obtained results it is possible to separate two regions. At first, the pristine bears mostly Fe^{3+} oxidation state, which starts to transform into Fe^{2+} during the treatment. The process goes for 30-40 minutes, after which a recovery process is likely taking over, thus

restoring partly Fe^{2+} . α -Fe is gradually growing in fraction during the treatment. Annealing of the sample at the crystallisation temperature for the same time in oxidising atmosphere does not recuperate the structure to its initial state.

- The newly developed emission Mössbauer spectrometer has been devised, developed and constructed. The fully automatised setup supports measurements from room up to elevated temperatures, with a possibility to perform angular-dependent measurements and experiments under applied light irradiation. Software for the pumping unit as well as for the electronic rack is developed and adjusted.

Perspectives:

For future work, additional TDPAC experiments on hydrogenated samples at both higher and cryogenic temperatures would be desirable. Having this in mind, one may observe the dynamic processes of hopping hydrogen once this region is more precisely determined. However, experiment featuring $^{111}\text{In}/\text{Cd}$ isotope could be of bigger use due to the implantation caused damage, which in this case can be avoided. Hence, future studies may take advantage of electrochemically deposited carrier free $^{111}\text{InCl}_3$ and diffused later on through low temperature annealing.

There is a desirable need of various *ab-initio* studies, which one may need in order to reconstruct which position in the lattice could yield the EFG values close to the experimental results. Experimental results of the eMS can be significantly expanded with super cell configurations of bigger volume. Scenarios where apical and equatorial V_o are combined with various hydrogen configurations would provide a better outlook on the structural relaxation and the resulting electric field gradient. It is worthy to point out that such calculations require plenty of time and computational power. Regarding the case of TDPAC studies performed at 473 K, here one may need to sway to and fro in order to pick appropriate large-scale quantum molecular dynamics simulations, which can unveil the dynamics of the ongoing processes.

eMIL has been constructed having in mind the solid ground for the additional modifications. One of the ways is to improve data acquisition, for instance, is an installation of the second PPAC detector. Two detectors could significantly boost the data collection time. The bottom lid can serve as the base for a sputtering DC source, if samples are going to be treated by plasma without breaking the vacuum. In order to make the system more reliable in terms of temperatures and changes taking place in the lattice is an installation on the bottom lid feedthroughs for electrical conductivity measurements. This is going to allow safely observe and check changes in materials such as V_2O_3 , where it may serve as a method to ensure the metal-to-insulator transition. For investigation of magnetic structure there is an extension modular setup in works (eMMA), which will allow studies with magnetic field up to 2.7 T (Vibrating Sample Magnetometer and possibility to measure Magneto-Optical Kerr Effect).

During the course of the current PhD study several contributions have been given to the scientific community. Materials which are used in the current dissertation are marked with • symbol.

Publications:

1. **Dmitry V. Zybkin**, Vít Procházka, Marcel Miglierini and Miroslav Mašláň, “Electrolytic cell-free ^{57}Co deposition for emission Mössbauer spectroscopy”, *J. Radiat. Phys. Chem.* 146, 86-90 (2018)
2. **Dmitry V. Zybkin**, Juliana Schell, Daniel Gaertner, Thanh T. Dang, João N. Gonçalves, Georg Marschick and Peter Schaaf, “Hyperfine Interactions and Diffusion of Cd in TiO_2 (rutile)”, *J. Appl. Phys.* 126, 015102 (2019) •
3. Juliana Schell, **Dmitry V. Zybkin**, Doru C. Lupascu, Hans-Christian Hofsäss, M. O. Karabasov, A. Welker and P. Schaaf, “A hyperfine look at titanium dioxide”, *AIP Adv.* 9, 085208 (2019) •
4. Miroslav Behul, Marian Vojs, Marian Marton, Pavol Michniak, Miroslav Mikolasek, Dominik Flock, Mario Kurniawan, Hauke-Lars Honig, **Dmitry V. Zybkin**, Manuel Oliva-Ramirez, Lothar Spiess, Andreas Bund, Martin Papula and Robert Redhammer, “Nanostructured boron doped diamond enhancing the photoelectrochemical performance of TiO_2/BDD heterojunction anodes”, *Vacuum* 171, 109006 (2020)
5. J. Schell, T. T. Dang, **D. V. Zybkin**, R. Mansano, D. Gaertner and A. W. Carbonari “Investigation of local environment of SnO_2 in an applied magnetic field”, *Physica B* 586, 412120 (2020)
6. **D. V. Zybkin**, H. P. Gunnlaugsson, J. N. Gonçalves, K. Bharuth-Ram, B. Qi, I. Unzueta, D. Naidoo, R. Mantovan, H. Masenda, S. Ólafsson, G. Peters, J. Schell, U. Vetter, A. Dimitrova, S. Krischok and P. Schaaf, “Experimental and Theoretical Study of Electronic and Hyperfine Properties of Hydrogenated Anatase (TiO_2): Defect

Interplay and Thermal Stability”, *Journal of Physical Chemistry C* 124 (13), 7511–7522 (2020) •

7. **Dmitry V. Zybkin**, Ulrich Vetter, Fredericus A. M. Linderhof, Haraldur P. Gunnlaugsson and Peter Schaaf, “eMIL: advanced emission Mössbauer spectrometer for measurements in versatile conditions”, *Nuclear Instruments and Methods in Physics Research Section A* 968, 163973 (2020) •

Conferences:

1. **Dmitry Zybkin**, Juliana Schell, Ulrich Vetter, Haraldur Pall Gunnlaugsson, Hilary Masenda, Peter Schaaf, and the ISOLDE Collaboration, “Defects investigation in black anatase”, *Deutsche Physikalische Gesellschaft, Spring Meeting*, DS 7.8 (2018) •
2. **Dmitry Zybkin**, Juliana Schell, Ulrich Vetter, Robinson Santos, and Peter Schaaf, “Perturbed angular correlation studies of H₂ plasma treated rutile”, *Deutsche Physikalische Gesellschaft, Spring Meeting*, DS 31.17 (2018) •
3. G. Marschick, J. Schell, B. Stöger, M. O. Karabasov, **D. Zybkin**, A. Welker, M. C. Escobar, V. Shvartsman, I. Efe and D. C. Lupascu, “PAC studies on the alpha-beta phase transition in multiferroic bismuth ferrite”, *Hyperfine Interactions 2019*, O-15 (2019);
4. D. Naidoo, G. Peters, H. Masenda, K. Bharuth-Ram, H. P. Gunnlaugsson, R. Adhikara, K. Johnston, P. Krastev, R. Mantovan, K. Naicker, S. Ólafsson, J. Schell, I. Unzueta, **D. Zybkin**, “An emission Mössbauer study of Fe implanted WC-Ni cemented carbide”, *Hyperfine Interactions 2019*, PG-02 (2019);
5. **Dmitry Zybkin**, Juliana Schell, Ulrich Vetter and Peter Schaaf “Structure evolution of hydrogenated TiO₂ by means of perturbed angular correlation”, *Deutsche Physikalische Gesellschaft, Spring Meeting*, DS 25.11 (2019) •
6. **Dmitry Zybkin**, H.P. Gunnlaugsson, Peter Schaaf and the ISOLDE Collaboration, “Hydrogenated anatase annealing with eMS”, *WEMS 2019*, (2019) •
7. **Dmitry Zybkin**, Ulrich Vetter and Peter Schaaf, “eMIL: advanced emission Mössbauer spectrometer”, *WEMS 2019*, (2019) •
8. Miroslav Behúl, Marian Vojs, Marián Marton, Pavol Michniak, Mario Kurniawan, Hauke-Lars Honig, **Dmitry Zybkin**, Manuel Oliva Ramirez and Andreas Bund, “Influence of TiO₂ thickness on PEC properties of BDD/TiO₂ electrodes”, *Proceedings of the International Conference Modern Electrochemical Methods XXXIX*, (2019);
9. **Dmitry Zybkin**, Ulrich Vetter, Fredericus Linderhof and Peter Schaaf, “eMIL: advanced emission Mössbauer Spectrometer”, *Deutsche Physikalische Gesellschaft, Spring Meeting*, O 48.9 (2020) •

Appendix A

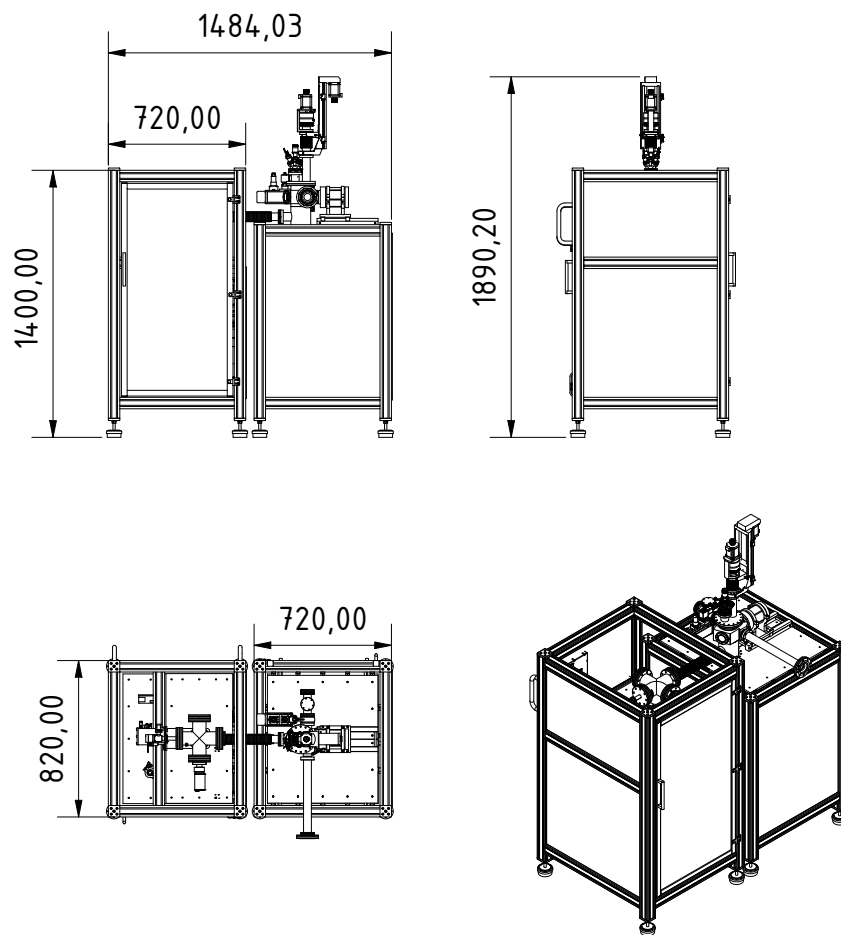
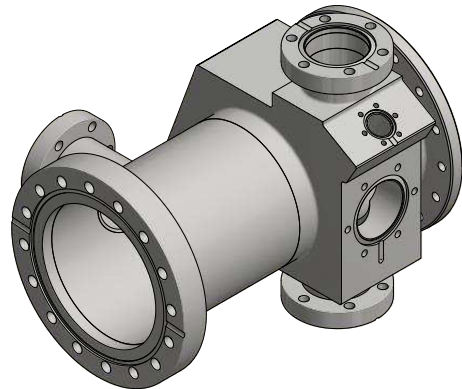
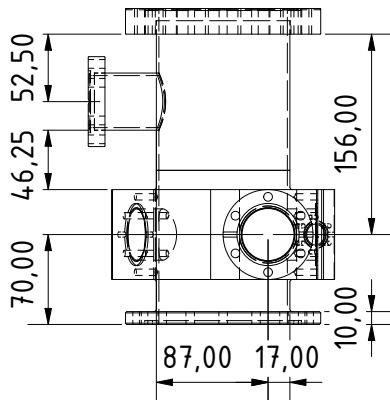
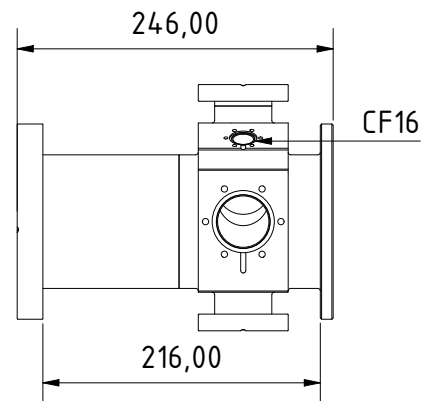
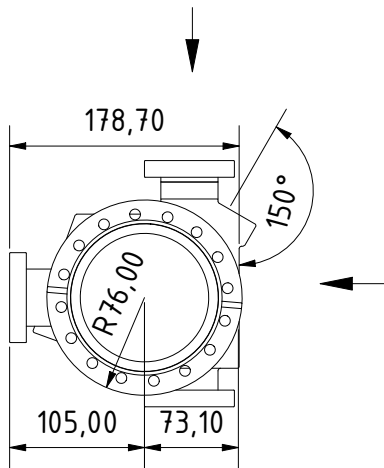
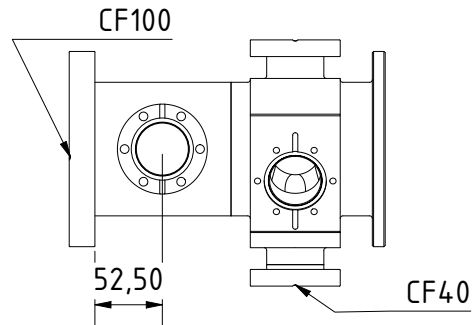
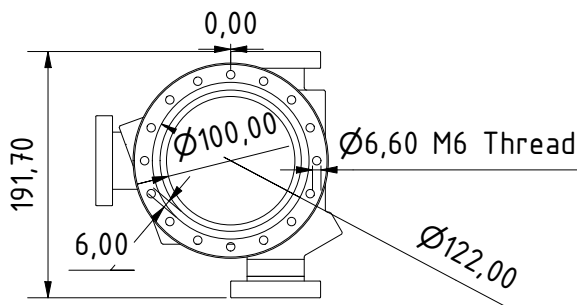
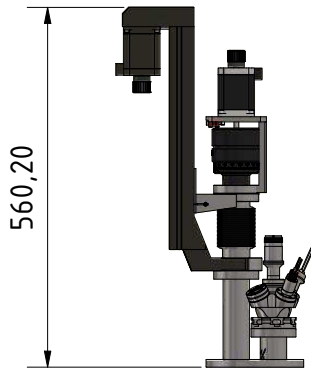
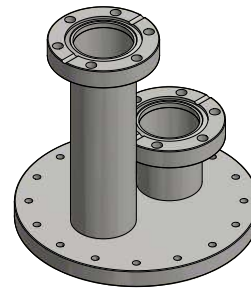
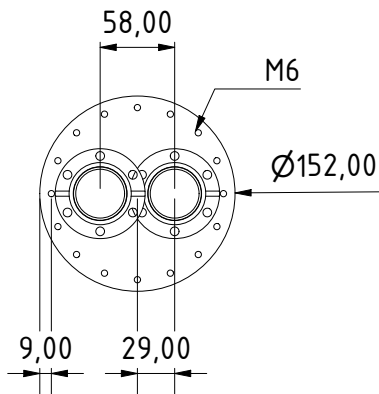
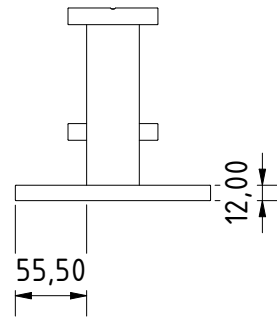
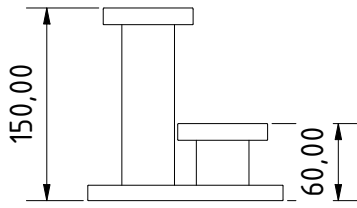


FIGURE 1: Dimensions of assembled eMIL.



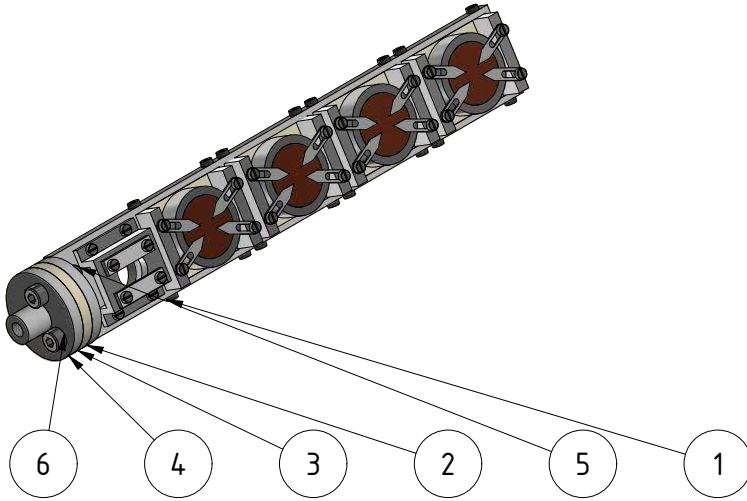
				Date	Name	eMIL chamber, 316LN STEEL; CF16, CF40, CF100		
				Drawn	30/01/2020			D.V. Zybkin
				Checked				
				Standard				
						chamber		
								1
						A4		
State	Changes	Date	Name					



				Date	Name	eMIL's HOT-LID, 316L STEEL; CF40, custom CF100 M6		
				Drawn	31/01/2020			D.V. Zyabkin
				Checked				
				Standard				
						the lid flange		
								1
						A4		
State	Changes	Date	Name					



PARTS LIST			
ITEM	QTY	PART NUMBER	DESCRIPTION
1	1	Assembled Holder	SS 304, Ceramic
2	1	Adapter 1a	SS 304
3	1	Adapter 1b	Ceramic
4	1	Adapter 1c	SS 304
5	2	ISO 4762 - M3 x 8(1)	Hexagon Socket Head Cap Screw
6	2	ISO 4762 - M4 x 12(1)	Hexagon Socket Head Cap Screw

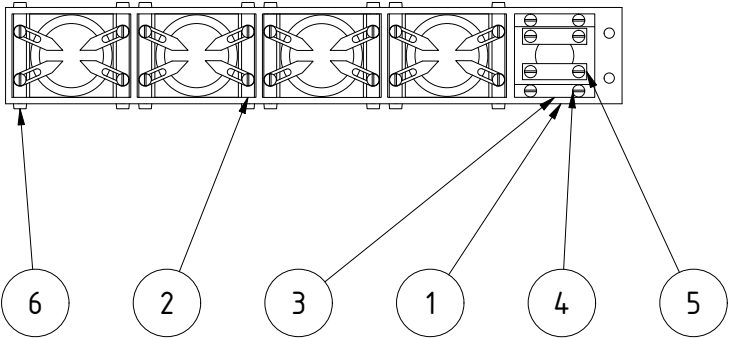


				Date	Name	eMIL sample holder	
			Drawn	20/02/2020	D.V. Zybkin		
			Checked				
			Standard				
						HOLDER_FF	
						1	
						A4	
State	Changes	Date	Name				



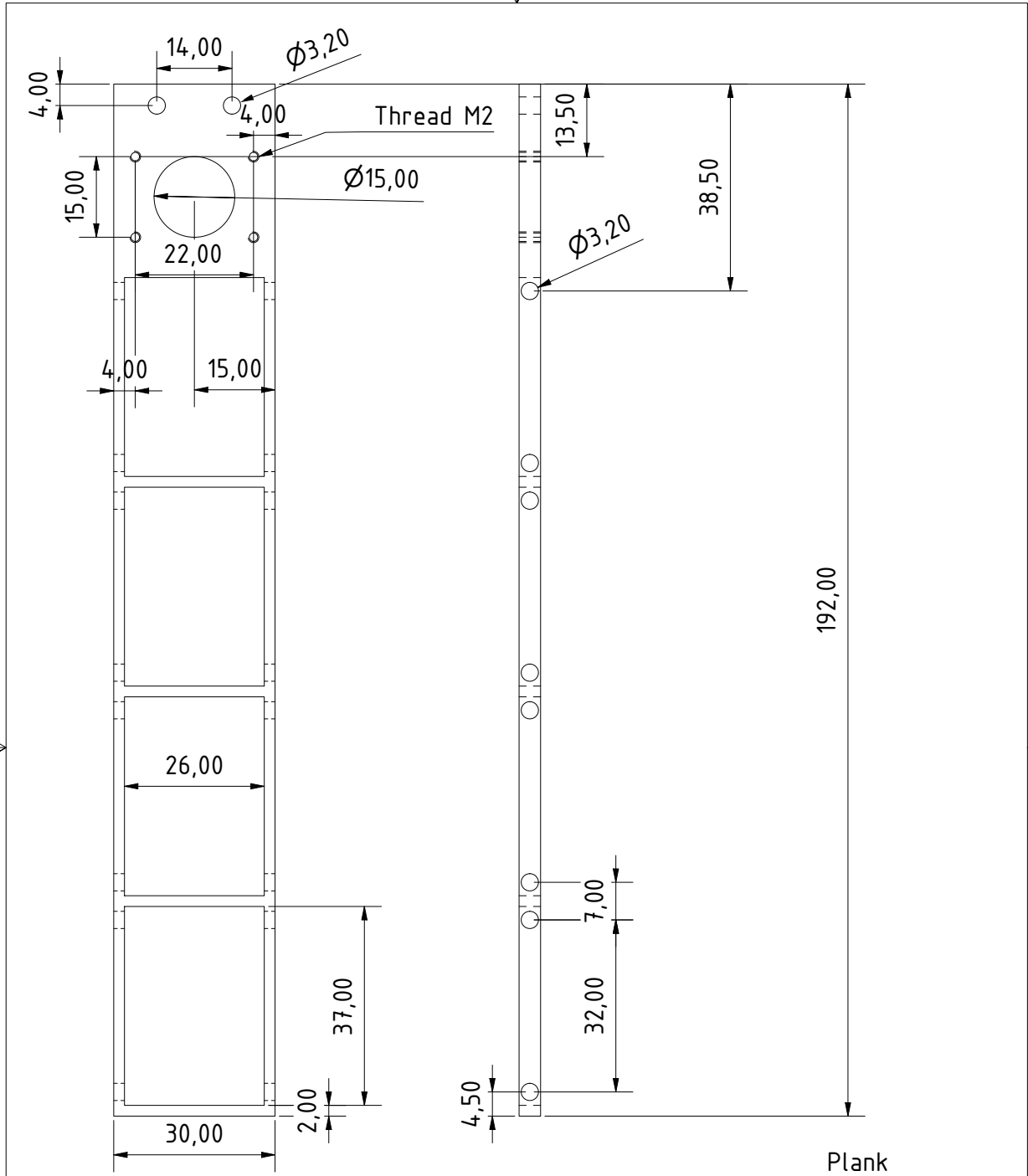


PARTS LIST			
ITEM	QTY	PART NUMBER	DESCRIPTION
1	1	Plank	Plank for Heaters with Housing
2	4	Button Heater,Housing 1	Heaters in Cells on Insulating Ceramic
3	1	Button Heater,Housing 2	Alpha Iron Sample Holder
4	8	ISO 1207 - M2 x 5(1)	Slotted cheese head screws - Product grade A
5	2	Clip	Clips for Sample Mounting
6	16	Hexalobular socket cheese head screw ISO 14580 - M2x5-4.8	ISO 14580 - Hexalobular socket cheese head screws - Second Edition



				Date	Name	eMIL sample holder		
				Drawn	20/02/2020			D.V. Zybkin
				Checked				
				Standard				
						HOLDER_FF		
						2		
						A4		
State	Changes	Date	Name					

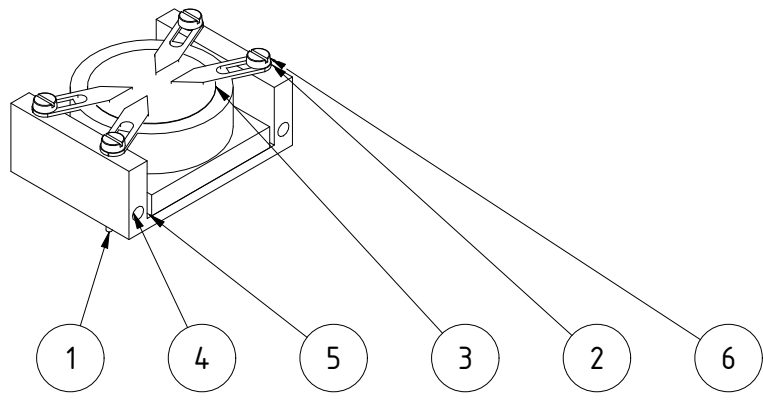




				Date	Name	eMIL sample holder		
				Drawn	20/02/2020			D.V. Zybkin
				Checked				
				Standard				
						HOLDER_FF		
						3		
						A4		
State	Changes	Date	Name					

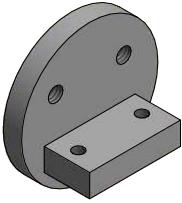
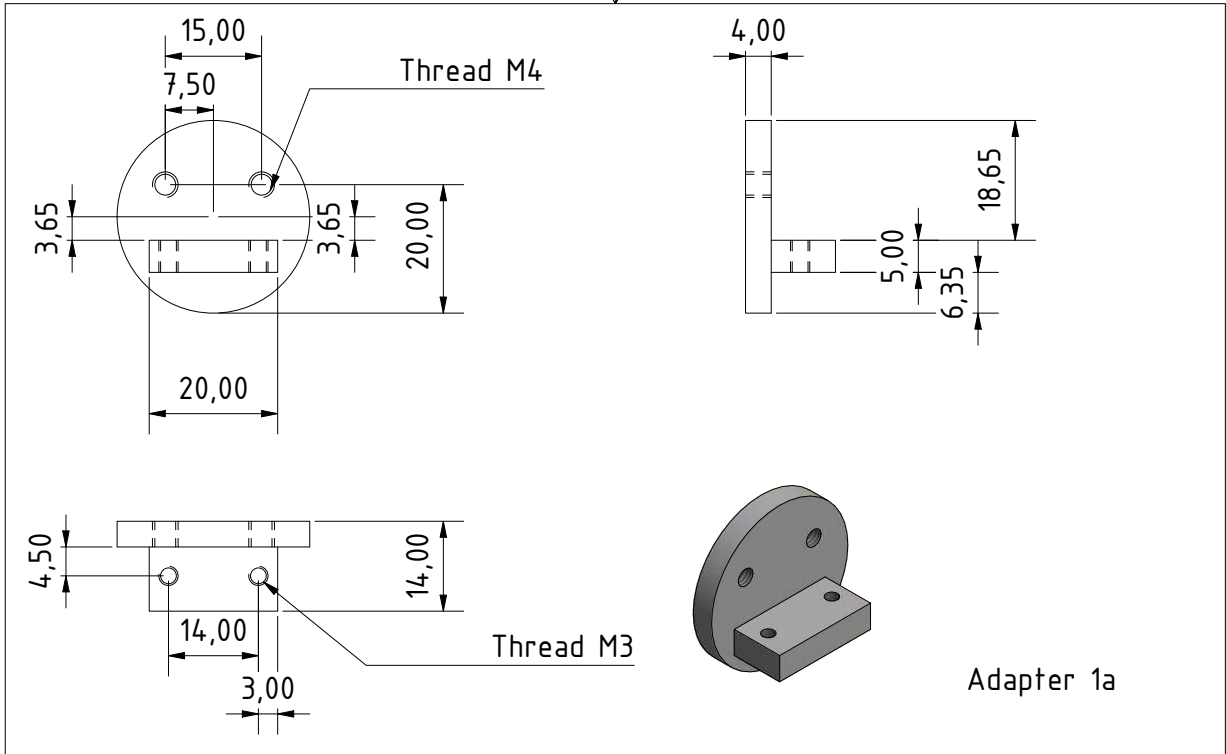


PARTS LIST			
ITEM	QTY	PART NUMBER	DESCRIPTION
1	1	ButtonHeater, HeatWave Lab 101138	Nitride Heaters
2	4	Clip	Clips for Sample Mounting
3	1	thin inter substrate	Cu foill d=20 mm
4	1	Housing	Square Cells
5	1	Ceramic Holder	Insulating Ceramic
6	4	ISO 1207 - M2 x 8(1)	Slotted cheese head screws - Product grade A

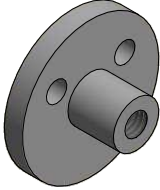
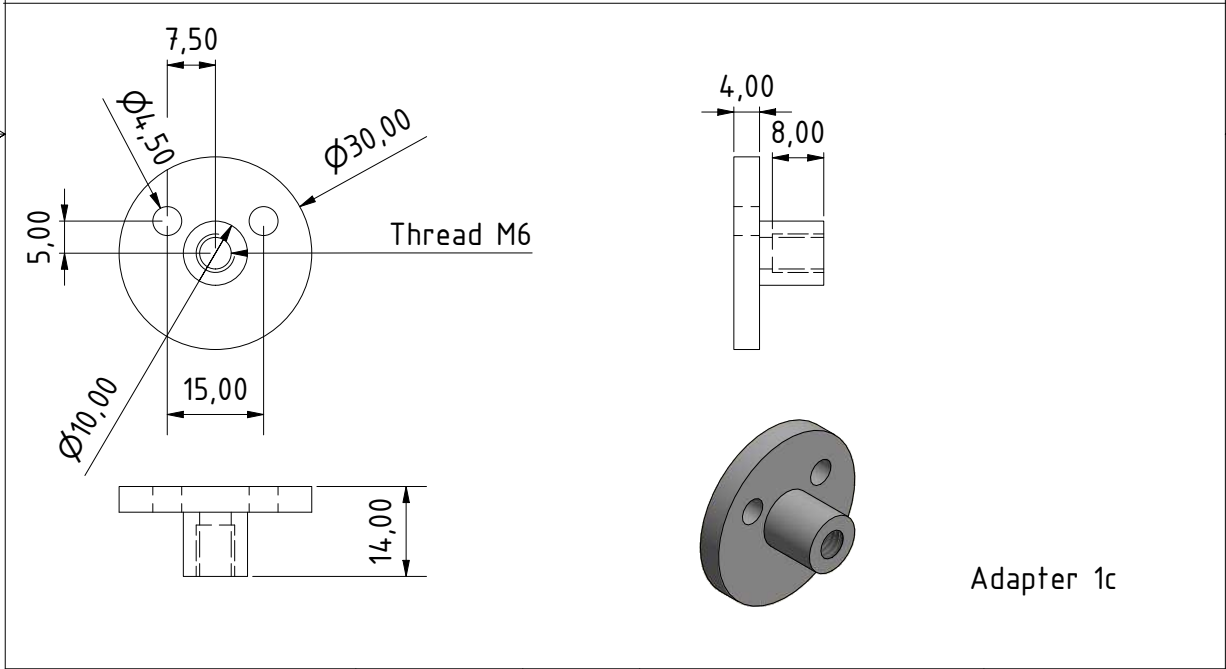


				Date	Name	eMIL sample holder	
			Drawn	20/02/2020	D.V. Zyabkin		
			Checked				
			Standard				
						HOLDER_FF	
						4	
						A4	
State	Changes	Date	Name				



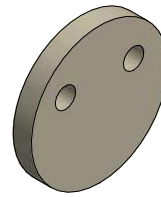
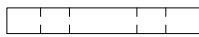
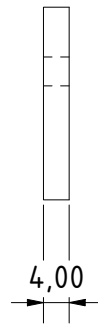
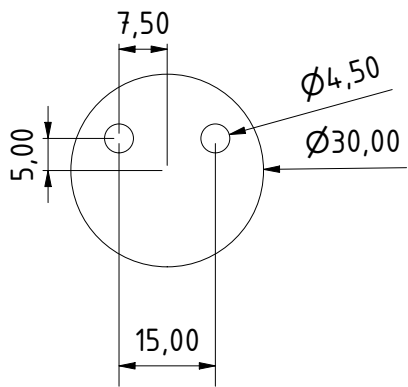


Adapter 1a

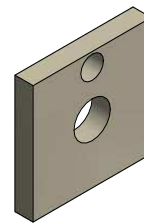
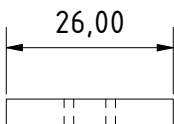
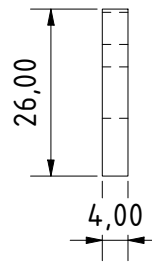
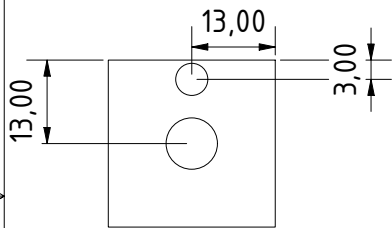


Adapter 1c

						eMIL sample holder	
		Drawn	20/02/2020	Name	D.V. Zybkin		
		Checked					
		Standard				HOLDER_FF	
						5	
						A4	
State	Changes	Date	Name				

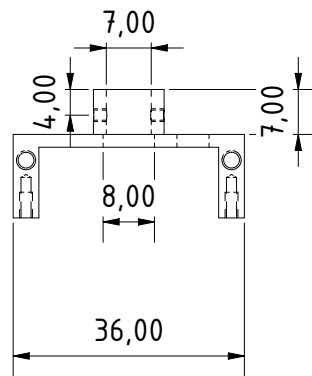
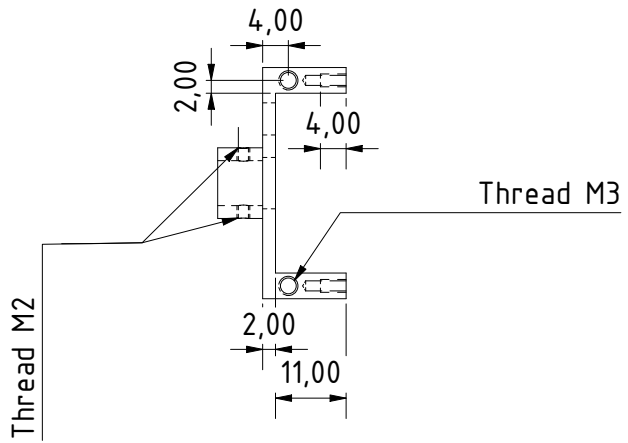
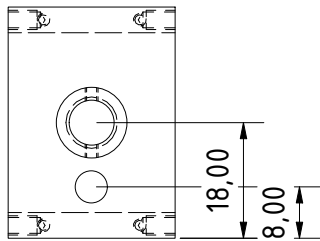
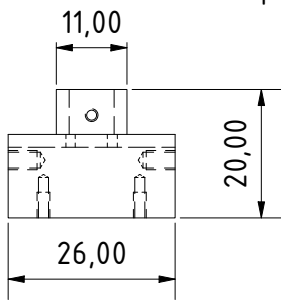
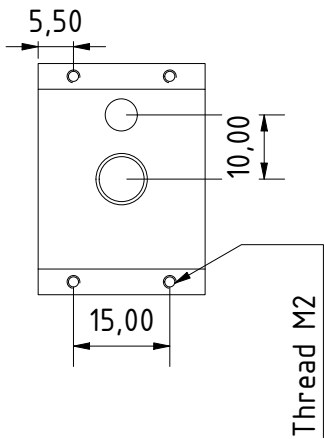


Adapter 1b



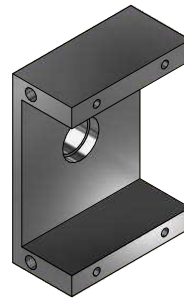
Ceramic Holder

				Date	Name	eMIL sample holder		
				Drawn	20/02/2020			D.V. Zybkin
				Checked				
				Standard				
						HOLDER_FF		
						6		
						A4		
State	Changes	Date	Name					



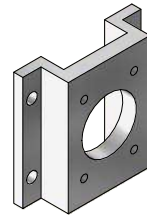
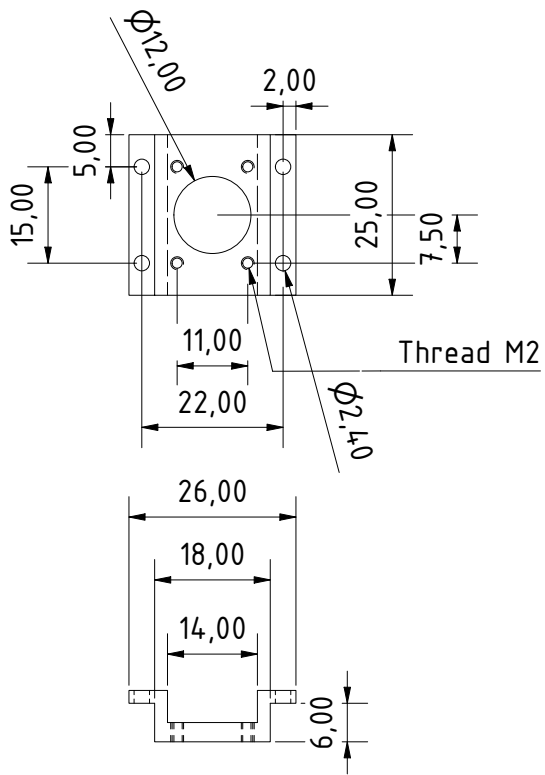
Thread M3

Thread M2



Housing 1

				Date	Name	eMIL sample holder		
				Drawn	20/02/2020			D.V. Zyabkin
				Checked				
				Standard				
						HOLDER_FF		
						7		
						A4		
State	Changes	Date	Name					



Housing 2

				Date	Name	eMIL sample holder		
				Drawn	20/02/2020			D.V. Zyabkin
				Checked				
				Standard				
						HOLDER_FF		
						8		
						A4		
State	Changes	Date	Name					

Bibliography

- [1] M. McCluskey and E. Haller, *Dopants and Defects in Semiconductors*. CRC Press, 2018.
- [2] Y. Yang, G. Liu, J. T. S. Irvine, and H.-M. Cheng, “Enhanced Photocatalytic H₂ Production in Core-Shell Engineered Rutile TiO₂,” *Adv. Mater.*, vol. 28, no. 28, pp. 5850–5856, 2016.
- [3] A. Radtke, P. Piszczek, A. Topolski, Z. Lewandowska, E. Talik, I. H. Andersen, L. P. Nielsen, M. Heikkilä, and M. Leskelä, “The Structure and the Photocatalytic Activity of Titania Based Nanotube and Nanofiber Coatings,” *Appl. Surf. Sci.*, vol. 368, pp. 165 – 172, 2016.
- [4] A. Fujishima and K. Honda, “Electrochemical Photolysis of Water at a Semiconductor Electrode,” *Nature*, vol. 238, no. 5358, pp. 37–38, 1972.
- [5] J. Low, B. Cheng, and J. Yu, “Surface Modification and Enhanced Photocatalytic CO₂ Reduction Performance of TiO₂: a Review,” *Appl. Surf. Sci.*, vol. 392, pp. 658 – 686, 2017.
- [6] T. Dietl, H. Ohno, F. Matsukura, J. Cibert, and D. Ferrand, “Zener Model Description of Ferromagnetism in Zinc-Blende Magnetic Semiconductors,” *Science*, vol. 287, no. 5455, pp. 1019–1022, 2000.
- [7] S.-D. Mo and W. Y. Ching, “Electronic and Optical Properties of Three Phases of Titanium Dioxide: Rutile, Anatase, and Brookite,” *Phys. Rev. B*, vol. 51, pp. 13023–13032, May 1995.
- [8] M. Kobayashi, V. V. Petrykin, M. Kakihana, K. Tomita, and M. Yoshimura, “One-Step Synthesis of TiO₂(B) Nanoparticles from a Water-Soluble Titanium Complex,” *Chem. Mater.*, vol. 19, no. 22, pp. 5373–5376, 2007.
- [9] M. V. Ganduglia-Pirovano, A. Hofmann, and J. Sauer, “Oxygen Vacancies in Transition Metal and Rare Earth Oxides: Current State of Understanding and Remaining Challenges,” *Surf. Sci. Rep.*, vol. 62, no. 6, pp. 219 – 270, 2007.
- [10] J. Schneider, M. Matsuoka, M. Takeuchi, J. Zhang, Y. Horiuchi, M. Anpo, and D. W. Bahnemann, “Understanding TiO₂ Photocatalysis: Mechanisms and Materials,” *Chem. Rev.*, vol. 114, no. 19, pp. 9919–9986, 2014.

- [11] J. Choi, H. Park, and M. R. Hoffmann, "Effects of Single Metal-Ion Doping on the Visible-Light Photoreactivity of TiO₂," *J. Phys. Chem. C*, vol. 114, no. 2, pp. 783–792, 2010.
- [12] W. Xie, R. Li, and Q. Xu, "Enhanced Photocatalytic Activity of Se-Doped TiO₂ under Visible Light Irradiation," *Sci. Rep.*, vol. 8, no. 1, p. 8752, 2018.
- [13] S. U. M. Khan, M. Al-Shahry, and W. B. Ingler, "Efficient Photochemical Water Splitting by a Chemically Modified n-TiO₂," *Science*, vol. 297, no. 5590, pp. 2243–2245, 2002.
- [14] R. Asahi, T. Morikawa, T. Ohwaki, K. Aoki, and Y. Taga, "Visible-Light Photocatalysis in Nitrogen-Doped Titanium Oxides," *Science*, vol. 293, no. 5528, pp. 269–271, 2001.
- [15] F. Zuo, L. Wang, T. Wu, Z. Zhang, D. Borchardt, and P. Feng, "Self-Doped Ti³⁺ Enhanced Photocatalyst for Hydrogen Production under Visible Light," *J. Am. Chem. Soc.*, vol. 132, no. 34, pp. 11856–11857, 2010.
- [16] K. Sasan, F. Zuo, Y. Wang, and P. Feng, "Self-Doped Ti³⁺-TiO₂ as a Photocatalyst for the Reduction of CO₂ into a Hydrocarbon Fuel under Visible Light Irradiation," *Nanoscale*, vol. 7, pp. 13369–13372, 2015.
- [17] B. Santara, P. K. Giri, K. Imakita, and M. Fujii, "Evidence of Oxygen Vacancy Induced Room Temperature Ferromagnetism in Solvothermally Synthesized Undoped TiO₂ Nanoribbons," *Nanoscale*, vol. 5, pp. 5476–5488, 2013.
- [18] H.-Y. Lee, S. J. Clark, and J. Robertson, "Calculation of Point Defects in Rutile TiO₂ by the Screened-Exchange Hybrid Functional," *Phys. Rev. B*, vol. 86, p. 075209, Aug 2012.
- [19] A. Janotti, J. B. Varley, P. Rinke, N. Umezawa, G. Kresse, and C. G. Van de Walle, "Hybrid Functional Studies of the Oxygen Vacancy in TiO₂," *Phys. Rev. B*, vol. 81, p. 085212, Feb 2010.
- [20] M. Setvin, C. Franchini, X. Hao, M. Schmid, A. Janotti, M. Kaltak, C. G. Van de Walle, G. Kresse, and U. Diebold, "Direct View at Excess Electrons in TiO₂ Rutile and Anatase," *Phys. Rev. Lett.*, vol. 113, p. 086402, Aug 2014.
- [21] H. Fröhlich, "Electrons in Lattice Fields," *Adv. Phys.*, vol. 3, no. 11, pp. 325–361, 1954.
- [22] S. X. Zhang, D. C. Kundaliya, W. Yu, S. Dhar, S. Y. Young, L. G. Salamanca-Riba, S. B. Ogale, R. D. Vispute, and T. Venkatesan, "Niobium Doped TiO₂: Intrinsic Transparent Metallic Anatase versus Highly Resistive Rutile Phase," *J. Appl. Phys.*, vol. 102, no. 1, p. 013701, 2007.
- [23] D. Morris, Y. Dou, J. Rebane, C. E. J. Mitchell, R. G. Egdell, D. S. L. Law, A. Vitadini, and M. Casarin, "Photoemission and STM Study of the Electronic Structure of Nb-Doped TiO₂," *Phys. Rev. B*, vol. 61, pp. 13445–13457, May 2000.

- [24] P. Deák, B. Aradi, and T. Frauenheim, “Polaronic Effects in TiO₂ Calculated by the HSE06 Hybrid Functional: Dopant Passivation by Carrier Self-Trapping,” *Phys. Rev. B*, vol. 83, p. 155207, Apr 2011.
- [25] P. Deák, B. Aradi, and T. Frauenheim, “Quantitative Theory of the Oxygen Vacancy and Carrier Self-trapping in Bulk TiO₂,” *Phys. Rev. B*, vol. 86, p. 195206, Nov 2012.
- [26] P. Deák, J. Kullgren, and T. Frauenheim, “Polarons and Oxygen Vacancies at the Surface of Anatase TiO₂,” *Phys. Status Solidi RRL*, vol. 8, no. 6, pp. 583–586, 2014.
- [27] S. K. Wallace and K. P. McKenna, “Facet-Dependent Electron Trapping in TiO₂ Nanocrystals,” *J. Phys. Chem. C*, vol. 119, no. 4, pp. 1913–1920, 2015.
- [28] L. Zhao, B. Magyari-Köpe, and Y. Nishi, “Polaronic Interactions between Oxygen Vacancies in Rutile TiO₂,” *Phys. Rev. B*, vol. 95, p. 054104, Feb 2017.
- [29] H. Noerenberg and G. Briggs, “Surface Structure of the Most Mxxygen Deficient Magnéli Phase - an STM study of Ti₄O₇,” *Surf. Sci.*, vol. 402-404, pp. 738 – 741, 1998.
- [30] J. Schell, D. C. Lupascu, A. W. Carbonari, R. Domingues Mansano, I. Souza Ribeiro Junior, T. T. Dang, I. Anusca, H. Trivedi, K. Johnston, and R. Vanden, “Ion Implantation in Titanium Dioxide Thin Films Studied by Perturbed Angular Correlations,” *J. Appl. Phys.*, vol. 121, no. 14, p. 145302, 2017.
- [31] A. F. Arif, R. Balgis, T. Ogi, F. Iskandar, A. Kinoshita, K. Nakamura, and K. Okuyama, “Highly Conductive Nano-sized Magnéli Phases Titanium Oxide (TiO_x),” *Sci. Rep.*, vol. 7, no. 1, p. 3646, 2017.
- [32] X. Tao, J. Wang, Z. Ying, Q. Cai, G. Zheng, Y. Gan, H. Huang, Y. Xia, C. Liang, W. Zhang, and Y. Cui, “Strong Sulfur Binding with Conducting Magnéli-Phase Ti_nO_{2n-1} Nanomaterials for Improving Lithium-Sulfur Batteries,” *Nano Lett.*, vol. 14, no. 9, pp. 5288–5294, 2014.
- [33] C. G. Van de Walle, “Hydrogen as a Cause of Doping in Zinc Oxide,” *Phys. Rev. Lett.*, vol. 85, pp. 1012–1015, Jul 2000.
- [34] K. Xiong and J. Robertson, “Hydrogen-Induced Defects and Degradation in Oxide Ferroelectrics,” *Appl. Phys. Lett.*, vol. 85, no. 13, pp. 2577–2579, 2004.
- [35] H. Pan, B. Gu, and Z. Zhang, “Phase-Dependent Photocatalytic Ability of TiO₂: A First-Principles Study,” *J. Chem. Theory Comput.*, vol. 5, no. 11, pp. 3074–3078, 2009.
- [36] W. Hebenstreit, N. Ruzycki, G. S. Herman, Y. Gao, and U. Diebold, “Scanning Tunneling Microscopy Investigation of the TiO₂ Anatase (101) Surface,” *Phys. Rev. B*, vol. 62, pp. R16334–R16336, Dec 2000.

- [37] K. Onda, B. Li, and H. Petek, "Two-Photon Photoemission Spectroscopy of TiO₂ (110) Surfaces Modified by Defects and O₂ or H₂O Adsorbates," *Phys. Rev. B*, vol. 70, p. 045415, Jul 2004.
- [38] H. P. Gunnlaugsson, R. Mantovan, H. Masenda, T. E. Mølholt, K. Johnston, K. Bharuth-Ram, H. Gislason, G. Langouche, D. Naidoo, S. Ólafsson, A. Svane, and G. W. and, "Defect Annealing in Mn/Fe-implanted TiO₂(rutile)," *J. Phys. D*, vol. 47, p. 065501, jan 2014.
- [39] M. Guermazi, P. Thevenard, M. Treilleux, and C. Dupuy, "Evidence of Extended Defects and Precipitates in TiO₂ Implanted with Potassium," *Mater. Res. Bull.*, vol. 15, no. 1, pp. 147 – 154, 1980.
- [40] X. Chen, L. Liu, P. Y. Yu, and S. S. Mao, "Increasing Solar Absorption for Photocatalysis with Black Hydrogenated Titanium Dioxide Nanocrystals," *Science*, vol. 331, p. 746, feb 2011.
- [41] A. P. Singh, N. Kodan, B. R. Mehta, A. Dey, and S. Krishnamurthy, "In-situ Plasma Hydrogenated TiO₂ Thin Films for Enhanced Photoelectrochemical Properties," *Mater. Res. Bull.*, vol. 76, pp. 284–291, 2016.
- [42] R. Ramos, D. Scoca, R. B. Merlo, F. C. Marques, F. Alvarez, and L. F. Zagonel, "Study of Nitrogen Ion Doping of Titanium Dioxide Films," *Appl. Surf. Sci.*, vol. 443, pp. 619 – 627, 2018.
- [43] S. Pearton, J. Corbett, and M. Stavola, *Hydrogen in Crystalline Semiconductors*. Springer series in materials science, Springer-Verlag, 1992.
- [44] Z. Wang, C. Yang, T. Lin, H. Yin, P. Chen, D. Wan, F. Xu, F. Huang, J. Lin, X. Xie, and M. Jiang, "H-Doped Black Titania with Very High Solar Absorption and Excellent Photocatalysis Enhanced by Localized Surface Plasmon Resonance," *Adv. Funct. Mater.*, vol. 23, no. 43, pp. 5444–5450, 2013.
- [45] Z. Zheng, B. Huang, J. Lu, Z. Wang, X. Qin, X. Zhang, Y. Dai, and M.-H. Whangbo, "Hydrogenated Titania: Synergy of Surface Modification and Morphology Improvement for Enhanced Photocatalytic Activity," *Chem. Commun.*, vol. 48, pp. 5733–5735, 2012.
- [46] T. Xia, C. Zhang, N. A. Oyler, and X. Chen, "Enhancing Microwave Absorption of TiO₂ Nanocrystals via Hydrogenation," *J. Mater. Res.*, vol. 29, no. 18, p. 2198–2210, 2014.
- [47] X. Chen, L. Liu, Z. Liu, M. A. Marcus, W.-C. Wang, N. A. Oyler, M. E. Grass, B. Mao, P.-A. Glans, P. Y. Yu, J. Guo, and S. S. Mao, "Properties of Disorder-Engineered Black Titanium Dioxide Nanoparticles through Hydrogenation," *Sci. Rep.*, vol. 3, pp. 1510 EP –, Mar 2013.
- [48] C. Kiliç and A. Zunger, "n-type Doping of Oxides by Hydrogen," *Appl. Phys. Lett.*, vol. 81, no. 1, pp. 73–75, 2002.

- [49] P. W. Peacock and J. Robertson, "Behavior of Hydrogen in High Dielectric Constant Oxide Gate Insulators," *Appl. Phys. Lett.*, vol. 83, no. 10, pp. 2025–2027, 2003.
- [50] F. Filippone, G. Mattioli, P. Alippi, and A. Amore Bonapasta, "Properties of Hydrogen and Hydrogen-Vacancy Complexes in the Rutile Phase of Titanium Dioxide," *Phys. Rev. B*, vol. 80, p. 245203, Dec 2009.
- [51] K. Xiong, J. Robertson, and S. J. Clark, "Behavior of Hydrogen in Wide Band Gap Oxides," *J. Appl. Phys.*, vol. 102, no. 8, p. 083710, 2007.
- [52] O. W. Johnson, W. D. Ohlsen, and P. I. Kingsbury, "Defects in Rutile. III. Optical and Electrical Properties of Impurities and Charge Carriers," *Phys. Rev.*, vol. 175, pp. 1102–1109, Nov 1968.
- [53] C. G. Van de Walle, P. J. H. Denteneer, Y. Bar-Yam, and S. T. Pantelides, "Theory of Hydrogen Diffusion and Reactions in Crystalline Silicon," *Phys. Rev. B*, vol. 39, pp. 10791–10808, May 1989.
- [54] W. P. Chen, Y. Wang, and H. L. W. Chan, "Hydrogen: a Metastable Donor in TiO₂ Single Crystals," *Appl. Phys. Lett.*, vol. 92, no. 11, p. 112907, 2008.
- [55] T. S. Bjørheim, S. Stølen, and T. Norby, "Ab Initio Studies of Hydrogenation and Acceptor Defects in Rutile TiO₂," *Phys. Chem. Chem. Phys.*, vol. 12, pp. 6817–6825, 2010.
- [56] I. Chaplygin, F. Herklotz, and E. V. Lavrov, "Reorientation Kinetics of Hydroxyl Groups in Anatase TiO₂," *J. Chem. Phys.*, vol. 149, no. 4, p. 044507, 2018.
- [57] O. W. Johnson, S. Paek, and J. W. DeFord, "Diffusion of H and D in TiO₂: Suppression of Internal Fields by Isotope Exchange," *J. Appl. Phys.*, vol. 46, no. 3, pp. 1026–1033, 1975.
- [58] R. E. Pritchard, M. J. Ashwin, J. H. Tucker, R. C. Newman, E. C. Lightowers, M. J. Binns, S. A. McQuaid, and R. Falster, "Interactions of Hydrogen Molecules with Bond-Centered Interstitial Oxygen and Another Defect Center in Silicon," *Phys. Rev. B*, vol. 56, pp. 13118–13125, Nov 1997.
- [59] E. Lavrov and J. Weber, "Hydrogen Molecules in GaAs," *Phys. B*, vol. 340-342, pp. 329 – 332, 2003.
Proceedings of the 22nd International Conference on Defects in Semiconductors.
- [60] W. P. Chen, K. F. He, Y. Wang, H. L. W. Chan, and Z. Yan, "Highly Mobile and Reactive state of Hydrogen in Metal Oxide Semiconductors at Room Temperature," *Sci. Rep.*, vol. 3, pp. 3149 EP –, Nov 2013.
- [61] T. Butz, "Analytic Perturbation Functions for Static Interactions in Perturbed Angular Correlations of γ -Rays," *Hyperfine Interact.*, vol. 52, pp. 189–228, Dec 1989.
- [62] P. Gütlich, E. Bill, and A. Trautwein, *Mössbauer Spectroscopy and Transition Metal Chemistry: Fundamentals and Applications*. Springer Berlin Heidelberg, 2010.

- [63] I. U. Solozabal, *Influence of Structural Defects on the Properties of Ni-based Heusler Alloys*. PhD thesis, Universidad del Pais Vasco / Euskal Herriko Unibertsitatea (ES), 2019.
- [64] D. Forkel-Wirth, "Exploring Solid State Physics Properties with Radioactive Isotopes," *Rep. Prog. Phys.*, vol. 62, pp. 527–597, Jan 1999.
- [65] J. Christiansen and H. Ackermann, *Hyperfine Interactions of Radioactive Nuclei*. Topics in current physics, Springer-Verlag, 1983.
- [66] R. Dogra, A. P. Byrne, and M. C. Ridgway, "The Potential of the Perturbed Angular Correlation Technique in Characterizing Semiconductors," *J. Electron. Mater.*, vol. 38, no. 5, pp. 623–634, 2009.
- [67] H. Frauenfelder and R. Steffen, *Alpha-, Beta-, and Gamma-Ray Spectroscopy*. Angular Correlation, North-Holland Amsterdam, Netherlands, 1965.
- [68] M. O. Zacate and H. Jaeger, "Perturbed Angular Correlation Spectroscopy – A Tool for the Study of Defects and Diffusion at the Atomic Scale," *Defect and Diffusion Forum*, vol. 311, pp. 3–38, 1 2011.
- [69] A. R. Arends, C. Hohenemser, F. Pleiter, H. de Waard, L. Chow, and R. M. Suter, "Data Reduction Methodology for Perturbed Angular Correlation Experiments," *Hyperfine Interact.*, vol. 8, pp. 191–213, Apr 1980.
- [70] M. Forker, "The Problematic of the Derivation of the Electric Fieldgradient Asymmetry Parameter from TDPAC Measurements or Mössbauer Spectroscopy in Imperfect Crystal Lattices," *Nuclear Instruments and Methods*, vol. 106, no. 1, pp. 121 – 126, 1973.
- [71] N. P. Barradas, "NFIT the PAC MANual (1992)," *Lissabon*, vol. 1, no. 1, 21992.
- [72] N. P. Barradas, M. Rots, A. A. Melo, and J. C. Soares, "Magnetic Anisotropy and Temperature Dependence of the Hyperfine Fields of ^{111}Cd in Single-Crystalline Cobalt," *Phys. Rev. B*, vol. 47, pp. 8763–8768, Apr 1993.
- [73] R. Johnson and M. T. Rogers, "Anomalous Temperature Dependence of the NQR Frequency in NH_4ReO_4 ," *J. Magn. Reson.*, vol. 15, no. 3, pp. 584 – 589, 1974.
- [74] H. Bayer, "Zur Theorie der Spin-Gitterrelaxation in Molekülkristallen," *Z. Phys.*, vol. 130, pp. 227–238, Apr 1951.
- [75] T.-C. Wang, "Pure Nuclear Quadrupole Spectra of Chlorine and Antimony Isotopes in Solids," *Phys. Rev.*, vol. 99, pp. 566–577, Jul 1955.
- [76] T. Kushida, G. B. Benedek, and N. Bloembergen, "Dependence of the Pure Quadrupole Resonance Frequency on Pressure and Temperature," *Phys. Rev.*, vol. 104, pp. 1364–1377, Dec 1956.
- [77] C. Ritter, M. R. Ibarra, J. M. De Teresa, P. A. Algarabel, C. Marquina, J. Blasco, J. García, S. Oseroff, and S.-W. Cheong, "Influence of Oxygen Content on the Structural, Magnetotransport, and Magnetic Properties of $\text{LaMnO}_{3+\delta}$," *Phys. Rev. B*, vol. 56, pp. 8902–8911, Oct 1997.

- [78] D. Richard, G. N. Darriba, E. L. Muñoz, L. A. Errico, P. D. Eversheim, and M. Rentera, “Experimental and First-Principles Theoretical Study of Structural and Electronic Properties in Tantalum-Doped In_2O_3 Semiconductor: Finding a Definitive Hyperfine Interaction Assignment,” *J. Phys. Chem. C*, vol. 120, no. 10, pp. 5640–5650, 2016.
- [79] W. Sato, H. Ueno, A. Taniguchi, Y. Itsuki, Y. Kasamatsu, A. Shinohara, K. Asahi, K. Asai, and Y. Ohkubo, “Nuclear Quadrupole Relaxation of ^{140}Ce Implanted in Highly Oriented Pyrolytic Graphite,” *Phys. Rev. B*, vol. 74, p. 214302, Dec 2006.
- [80] J. Christiansen, P. Heubes, R. Keitel, W. Klinger, W. Loeffler, W. Sandner, and W. Witthuhn, “Temperature Dependence of the Electric Field Gradient in Non-cubic Metals,” *Z. Phys.*, vol. 24, pp. 177–187, Jun 1976.
- [81] D. Torumba, K. Parlinski, M. Rots, and S. Cottenier, “Temperature Dependence of the Electric-Field Gradient in hcp-Cd from First Principles,” *Phys. Rev. B*, vol. 74, p. 144304, Oct 2006.
- [82] O. Kanert and H. Kolem, “The Unusual Temperature Dependence of the Electric Field Gradient at Titanium Sites in Rutile (TiO_2),” *J. Phys. Condens. Matter*, vol. 21, pp. 3909–3916, Jul 1988.
- [83] J. M. Adams and G. L. Catchen, “Anomalous Crystal Chemistries of the $^{111}\text{In} \rightarrow ^{111}\text{Cd}$ and $^{181}\text{Ta} \rightarrow ^{181}\text{Ta}$ Probes in Rutile TiO_2 Studied using Perturbed-Angular-Correlation Spectroscopy,” *Phys. Rev. B*, vol. 50, pp. 1264–1267, Jul 1994.
- [84] E. L. Muñoz, A. W. Carbonari, L. A. Errico, A. G. Bibiloni, H. M. Petrilli, and M. Rentería, “TDPAC Study of Cd-Doped SnO ,” *Hyperfine Interact.*, vol. 178, p. 37, Aug 2008.
- [85] G. N. Darriba, E. L. Muñoz, A. W. Carbonari, and M. Rentería, “Experimental TDPAC and Theoretical DFT Study of Structural, Electronic, and Hyperfine Properties in ($^{111}\text{In} \rightarrow ^{111}\text{Cd}$)-Doped SnO_2 Semiconductor: Ab Initio Modeling of the Electron-Capture-Decay After-Effects Phenomenon,” *J. Phys. Chem. C*, vol. 122, no. 30, pp. 17423–17436, 2018.
- [86] R. L. Mössbauer, “The discovery of the Mössbauer effect,” *Hyperfine Interact.*, vol. 126, pp. 1–12, Jul 2000.
- [87] Y. Chen and D. Yang, *Mössbauer Effect in Lattice Dynamics: Experimental Techniques and Applications*. Wiley, 2007.
- [88] H. Gunnlaugsson, “Spreadsheet Based Analysis of Mössbauer Spectra,” *Hyperfine Interact.*, vol. 237, no. 1, p. 79, 2016.
- [89] *Happy Sloth PC Programm for Mössbauer Spectra Fitting*, vol. 5805 of ICAME, Springer, 2017.

- [90] P. Hohenberg and W. Kohn, "Inhomogeneous Electron Gas," *Phys. Rev.*, vol. 136, pp. B864–B871, Nov 1964.
- [91] W. Kohn and L. J. Sham, "Self-Consistent Equations Including Exchange and Correlation Effects," *Phys. Rev.*, vol. 140, pp. A1133–A1138, Nov 1965.
- [92] P. Blaha, K. Schwarz, G. Madsen, D. Kvasnicka, J. Luitz, and K. Schwarz, "An Augmented Plane Wave plus local Orbitals Program for Calculating Crystal Properties: Wien2K User's Guide (Wien:Technische Universität Wien)," *TU Wien*, 2008.
- [93] G. Kresse and J. Furthmüller, "Efficiency of Ab-Initio Total Energy Calculations for Metals and Semiconductors using a Plane-Wave Basis Set," *Comput. Mater. Sci.*, vol. 6, no. 1, pp. 15 – 50, 1996.
- [94] D. Singh and L. Nordström, *Plane waves, Pseudopotentials, and the LAPW Method*. Springer US, 2006.
- [95] P. E. Blöchl, "Projector Augmented-Wave Method," *Phys. Rev. B*, vol. 50, pp. 17953–17979, Dec 1994.
- [96] U. D. Wdowik and K. Ruebenbauer, "Calibration of the Isomer Shift for the 14.4 KeV Transition in ^{57}Fe using the Full-Potential Linearized Augmented Plane-Wave Method," *Phys. Rev. B*, vol. 76, p. 155118, Oct 2007.
- [97] H. Gunnlaugsson and H. Masenda, "Mössbauer Isomer-Shift of Ferrous Iron Impurities in Ionic and Covalent Binary Compounds," *J. Phys. Chem. Solids*, vol. 129, pp. 151 – 154, 2019.
- [98] R. Catherall, W. Andreazza, M. Breitenfeldt, A. Dorsival, G. J. Focker, T. P. Gharsa, J. Giles T, J.-L. Grenard, F. Locci, P. Martins, S. Marzari, J. Schipper, A. Shornikov, and T. Stora, "The ISOLDE Facility," *J. Phys. G*, vol. 44, no. 9, p. 094002, 2017.
- [99] J. Schell, P. Schaaf, and D. C. Lupascu, "Perturbed Angular Correlations at ISOLDE: A 40 Years Young Technique," *AIP Adv.*, vol. 7, no. 10, p. 105017, 2017.
- [100] K. Johnston, J. Schell, J. G. Correia, M. Deicher, H. P. Gunnlaugsson, A. S. Fenta, E. David-Bosne, A. R. G. Costa, and D. C. Lupascu, "The Solid State Physics Programme at ISOLDE: Recent Developments and Perspectives," *J. Phys. G*, vol. 44, p. 104001, aug 2017.
- [101] M. Deicher, G. Weyer, T. Wichert, and the ISOLDE Collaboration, "Solid State Physics at ISOLDE," *Hyperfine Interact.*, vol. 151, pp. 105–123, Dec 2003.
- [102] S. Rothe, B. A. Marsh, C. Mattolat, V. N. Fedosseev, and K. Wendt, "A Complementary Laser System for ISOLDE RILIS," *J. Phys.: Conf. Ser.*, vol. 312, p. 052020, sep 2011.

- [103] V. Fedoseyev, K. Bätzner, R. Catherall, A. Evensen, D. Forkel-Wirth, O. Jonsson, E. Kugler, J. Lettry, V. Mishin, H. Ravn, and G. Weyer, “Chemically Selective Laser Ion Source of Manganese,” *Nucl. Instrum. Methods Phys. Res., Sect. B*, vol. 126, no. 1, pp. 88 – 91, 1997.
- [104] M. Nagl, M. Barbosa, U. Vetter, J. Correia, and H. Hofsäss, “A New Tool for the Search of Nuclides with Properties Suitable for (n)uclear Solid State Physics based on the Evaluated Nuclear Structure Data Files,” *Nucl. Instrum. Methods Phys. Res., Sect. A*, vol. 726, pp. 17 – 30, 2013.
- [105] T. A. Webb, L. Nikkinen, J. Gallego, and D. H. Ryan, “A Simple Digital TDPAC Spectrometer,” *Hyperfine Interact.*, vol. 222, pp. 103–108, May 2013.
- [106] M. Nagl, U. Vetter, M. Uhrmacher, and H. Hofsäss, “A new all-Digital Time Differential $\gamma - \gamma$ Angular Correlation Spectrometer,” *Rev. Sci. Instrum.*, vol. 81, no. 7, p. 073501, 2010.
- [107] J. F. Ziegler, M. D. Ziegler, and J. P. Biersack, “SRIM - The Stopping and Range of Ions in Matter (2010),” *Nucl. Instrum. Methods Phys. Res., Sect. B*, vol. 268, no. 11, pp. 1818–1823, 2010.
- [108] T. Butz, *Fourier Transformation for Pedestrians. Fourier Series*, Springer Berlin Heidelberg, 2005.
- [109] H. Wolf, F. Wagner, and T. Wichert, “Anomalous Diffusion Profiles of Ag in CdTe due to Chemical Self-Diffusion,” *Phys. Rev. Lett.*, vol. 94, p. 125901, Apr 2005.
- [110] D. Gaertner, *Atomic Transport in Single Phased Equiatomic and Pseudo-Binary Couple High Entropy Alloys*. PhD thesis, University of Munster, 2020.
- [111] F. Salvat and J. Parellada, “Theory of Conversion Electron Mössbauer Spectroscopy (CEMS),” *Nucl. Instrum. Methods Phys. Res., Sect. B*, vol. 1, no. 1, pp. 70 – 84, 1984.
- [112] J. R. Gancedo, M. Gracia, and J. F. Marco, “CEMS Methodology,” *Hyperfine Interact.*, vol. 66, pp. 83–93, Nov 1991.
- [113] L. Errico, K. Lejaeghere, J. Runco, S. N. Mishra, M. Rentería, and S. Cottenier, “Precision of Electric-Field Gradient Predictions by Density Functional Theory and Implications for the Nuclear Quadrupole Moment and Its Error Bar of the ^{111}Cd 245 keV $5/2+$ Level,” *J. Phys. Chem. C*, vol. 120, no. 40, pp. 23111–23120, 2016.
- [114] K. Bharuth-Ram, W. Dlamini, H. Masenda, D. Naidoo, H. Gunnlaugsson, G. Weyer, R. Mantovan, T. Mølholt, R. Sielemann, S. Ólafsson, G. Langouche, and K. Johnston, “ ^{57}Fe Mössbauer Studies on $^{57}\text{Mn}^*$ Implanted InP and InAs,” *Nucl. Instrum. Methods Phys. Res., Sect. B*, vol. 272, pp. 414 – 417, 2012. Proceedings of the 17th International Conference on Ion Beam Modification of Materials (IBMM 2010).

- [115] L. Ellselami, H. Lachheb, and A. Houas, "Synthesis, Characterization and Photocatalytic Activity of Li-, Cd-, and La-Doped TiO₂," *Mater. Sci. Semicond. Process.*, vol. 36, pp. 103 – 114, 2015.
- [116] S. Shetty, S. K. Sinha, R. Ahmad, A. K. Singh, G. Van Tendeloo, and N. Ravishankar, "Existence of Ti²⁺ States on the Surface of Heavily Reduced SrTiO₃ Nanocubes," *Chem. Mater.*, vol. 29, no. 23, pp. 9887–9891, 2017.
- [117] D. Wang, Y. Yan, P. Schaaf, T. Sharp, S. Schönherr, C. Ronning, and R. Ji, "ZnO/porous-Si and TiO₂/porous-Si Nanocomposite Nanopillars," *J. Vac. Sci. Technol. A*, vol. 33, no. 1, p. 01A102, 2015.
- [118] K.-C. Zhang, Y.-F. Li, Y. Liu, and Y. Zhu, "Possible Ferromagnetism in Cd-Doped TiO₂: a First-Principles Study," *Phys. B*, vol. 422, pp. 28 – 32, 2013.
- [119] Z. Zou, Z. Zhou, H. Wang, and Z. Yang, "Effect of Au Clustering on Ferromagnetism in Au-Doped TiO₂ Films: Theory and Experiments Investigation," *J. Phys. Chem. Solids*, vol. 100, pp. 71 – 77, 2017.
- [120] Z. Zhao, X. Zhang, G. Zhang, Z. Liu, D. Qu, X. Miao, P. Feng, and Z. Sun, "Effect of Defects on Photocatalytic Activity of Rutile TiO₂ Nanorods," *Nano Res.*, vol. 8, pp. 4061–4071, Dec 2015.
- [121] T. Wenzel, A. Bartos, K. P. Lieb, M. Uhrmacher, and D. Wiarda, "Hyperfine Interactions of ¹¹¹Cd in TiO₂ (Rutile) Studied by Perturbed Angular Correlations," *Ann. Phys.*, vol. 504, no. 3, pp. 155–163, 1992.
- [122] S. K. Das, S. V. Thakare, and T. Butz, "The Nuclear Quadrupole Interaction at ¹¹¹Cd and ¹⁸¹Ta Sites in Anatase and Rutile TiO₂: A TDPAC Study," *J. Phys. Chem. Solids*, vol. 70, no. 3, pp. 778 – 781, 2009.
- [123] L. A. Errico, "Ab initio Study of the Temperature Dependence of the EFG at Cd impurities in Rutile TiO₂," *Hyperfine Interact.*, vol. 158, pp. 29–35, Nov 2004.
- [124] J. Schell, D. C. Lupascu, J. G. Martins Correia, A. W. Carbonari, M. Deicher, M. B. Barbosa, R. D. Mansano, K. Johnston, I. S. Ribeiro, and I. collaboration, "In and Cd as Defect Traps in Titanium Dioxide," *Hyperfine Interact.*, vol. 238, p. 2, Nov 2016.
- [125] G. N. Darriba, L. A. Errico, P. D. Eversheim, G. Fabricius, and M. Rentería, "First-principles and Time-differential γ - γ Perturbed-Angular-Correlation Spectroscopy Study of Structural and Electronic Properties of Ta-Doped TiO₂ Semiconductor," *Phys. Rev. B*, vol. 79, p. 115213, Mar 2009.
- [126] L. A. Errico, G. Fabricius, M. Rentería, P. de la Presa, and M. Forker, "Anisotropic Relaxations Introduced by Cd Impurities in Rutile TiO₂: First-Principles Calculations and Experimental Support," *Phys. Rev. Lett.*, vol. 89, p. 055503, Jul 2002.
- [127] H. Mehrer, *Diffusion in Solids*. Springer, Berlin, 2007.

- [128] F. Hergemöller, M. Wegner, M. Deicher, H. Wolf, F. Brenner, H. Hutter, R. Abart, and N. A. Stolwijk, "Potassium Self-Diffusion in a K-rich Single-crystal Alkali Feldspar," *Phys. Chem. Miner.*, vol. 44, no. 5, pp. 345–351, 2017.
- [129] D. Gaertner, J. Kottke, Y. Chumlyakov, G. Wilde, and S. V. Divinski, "Tracer Diffusion in Single Crystalline CoCrFeNi and CoCrFeMnNi High Entropy Alloys," *J. Mater. Res.*, vol. 33, no. 19, pp. 3184–3191, 2018.
- [130] A. Strohm, T. Voss, W. Frank, P. Laitinen, and J. Räisänen, "Self-diffusion of ^{71}Ge and ^{31}Si in Si-Ge Alloys," *Z. Metallkd.*, vol. 93, no. 7, pp. 737–744, 2002.
- [131] J. Sasaki, N. L. Peterson, and K. Hoshino, "Tracer Impurity Diffusion in Single-crystal Rutile (TiO_{2-x})," *J. Phys. Chem. Solids*, vol. 46, no. 11, pp. 1264–1283, 1985.
- [132] L. Zhu, G. Ackland, Q.-M. Hu, J. Zhou, and Z. Sun, "Origin of the Abnormal Diffusion of Transition Metal Atoms in Rutile," *Phys. Rev. B*, vol. 95, p. 245201, Jun 2017.
- [133] J. K. Burdett, T. Hughbanks, G. J. Miller, J. W. Richardson, and J. V. Smith, "Structural-Electronic Relationships in Inorganic Solids: Powder Neutron Diffraction Studies of the Rutile and Anatase Polymorphs of Titanium Dioxide at 15 and 295 K," *J. Am. Chem. Soc.*, vol. 109, no. 12, pp. 3639–3646, 1987.
- [134] L. A. Errico, G. Fabricius, and M. Rentería, "Metal Impurities in an Oxide: Ab Initio Study of Electronic and Structural Properties of Cd in Rutile TiO_2 ," *Phys. Rev. B*, vol. 67, p. 144104, Apr 2003.
- [135] S.-b. Ryu, S. K. Das, T. Butz, W. Schmitz, C. Spiel, P. Blaha, and K. Schwarz, "Nuclear Quadrupole Interaction at ^{44}Sc in the Anatase and Rutile Modifications of TiO_2 : Time-differential Perturbed-Angular-Correlation Measurements and ab initio Calculations," *Phys. Rev. B*, vol. 77, p. 094124, Mar 2008.
- [136] G. Kresse and D. Joubert, "From Ultrasoft Pseudopotentials to the Projector Augmented-Wave Method," *Phys. Rev. B*, vol. 59, pp. 1758–1775, Jan 1999.
- [137] J. P. Perdew, K. Burke, and M. Ernzerhof, "Generalized Gradient Approximation Made Simple," *Phys. Rev. Lett.*, vol. 77, pp. 3865–3868, Oct 1996.
- [138] H. Li, Y. Guo, and J. Robertson, "Calculation of TiO_2 Surface and Subsurface Oxygen Vacancy by the Screened Exchange Functional," *J. Phys. Chem. C*, vol. 119, no. 32, pp. 18160–18166, 2015.
- [139] A. Stevanovic and J. T. Yates, "Electron Hopping through TiO_2 Powder: A Study by Photoluminescence Spectroscopy," *J. Phys. Chem. C*, vol. 117, pp. 24189–24195, Nov. 2013.
- [140] A. Stevanovic, M. Büttner, Z. Zhang, and J. T. Yates, "Photoluminescence of TiO_2 : Effect of UV Light and Adsorbed Molecules on Surface Band Structure," *J. Am. Chem. Soc.*, vol. 134, pp. 324–332, Jan. 2012.

- [141] S. Kurian, H. Seo, and H. Jeon, "Significant Enhancement in Visible Light Absorption of TiO₂ Nanotube Arrays by Surface Band Gap Tuning," *J. Phys. Chem. C*, vol. 117, no. 33, pp. 16811–16819, 2013.
- [142] J. Lu, Y. Dai, H. Jin, and B. Huang, "Effective Increasing of Optical Absorption and Energy Conversion Efficiency of Anatase TiO₂ Nanocrystals by Hydrogenation," *Phys. Chem. Chem. Phys.*, vol. 13, pp. 18063–18068, 2011.
- [143] M. R. Hoffmann, S. T. Martin, W. Choi, and D. W. Bahnemann, "Environmental Applications of Semiconductor Photocatalysis," *Chem. Rev.*, vol. 95, no. 1, pp. 69–96, 1995.
- [144] T. Xia and X. Chen, "Revealing the Structural Properties of Hydrogenated Black TiO₂ Nanocrystals," *J. Mater. Chem. A*, vol. 1, no. 9, pp. 2983–2989, 2013.
- [145] H. Wang, J. Xiong, X. Cheng, G. Chen, T. Kups, D. Wang, and P. Schaaf, "N-Doped TiO₂ with a Disordered Surface Layer Fabricated via Plasma Treatment as an Anode with Clearly Enhanced Performance for Rechargeable Sodium Ion Batteries," *Sustainable Energy Fuels*, pp. –, 2019.
- [146] X. Chen, L. Liu, and F. Huang, "Black Titanium Dioxide (TiO₂) Nanomaterials," *Chem. Soc. Rev.*, vol. 44, no. 7, pp. 1861–1885, 2015.
- [147] H. Li and J. Robertson, "Behaviour of Hydrogen in Wide Band Gap Oxides," *J. Appl. Phys.*, vol. 115, no. 20, p. 203708, 2014.
- [148] A. T. Brant, S. Yang, N. C. Giles, and L. E. Halliburton, "Hydrogen Donors and Ti³⁺ Ions in Reduced TiO₂ Crystals," *J. Appl. Phys.*, vol. 110, no. 5, p. 053714, 2011.
- [149] H. Sezen, M. Buchholz, A. Nefedov, S. Heissler, C. Di Valentin, and C. Wöll, "Probing Electrons in TiO₂ Polaronic Trap States by IR-absorption: Evidence for the Existence of Hydrogenic States," *Sci. Rep.*, vol. 4, no. 3808, 2014.
- [150] V. Lavrov E., "Infrared Absorption on Hydrogen in Anatase TiO₂," *Phys. Status Solidi A*, vol. 212, no. 7, pp. 1494–1498, 2015.
- [151] E. V. Lavrov, "Hydrogen Donor in Anatase TiO₂," *Phys. Rev. B*, vol. 93, p. 045204, Jan 2016.
- [152] X. Yu, B. Kim, and Y. K. Kim, "Highly Enhanced Photoactivity of Anatase TiO₂ Nanocrystals by Controlled Hydrogenation-Induced Surface Defects," *ACS Catal.*, vol. 3, no. 11, pp. 2479–2486, 2013.
- [153] C. A. Vlaic, S. Ivanov, R. Peipmann, A. Eisenhardt, M. Himmerlich, S. Krischok, and A. Bund, "Electrochemical Lithiation of Thin Silicon based Layers Potentiostatically Deposited from Ionic Liquid," *Electrochim. Acta*, vol. 168, pp. 403 – 413, 2015.
- [154] M. J. G. Borge and B. Jonson, "ISOLDE Past, Present and Future," *J. Phys. G*, vol. 44, no. 4, p. 044011, 2017.

- [155] V. Fedoseyev, G. Huber, U. Köster, J. Lettry, V. Mishin, H. Ravn, and V. Sebastian, "The ISOLDE Laser Ion Source for Exotic Nuclei," *Hyperfine Interact.*, vol. 127, pp. 409–416, Aug 2000.
- [156] C. Sun, Y. Jia, X.-H. Yang, H.-G. Yang, X. Yao, G. Q. M. Lu, A. Selloni, and S. C. Smith, "Hydrogen Incorporation and Storage in Well-Defined Nanocrystals of Anatase Titanium Dioxide," *J. Phys. Chem. C*, vol. 115, no. 51, pp. 25590–25594, 2011.
- [157] U. Diebold, "The Surface Science of Titanium Dioxide," *Surf. Sci. Rep.*, vol. 48, no. 5, pp. 53–229, 2003.
- [158] A. Naldoni, M. Allieta, S. Santangelo, M. Marelli, F. Fabbri, S. Cappelli, C. L. Bianchi, R. Psaro, and V. Dal Santo, "Effect of Nature and Location of Defects on Bandgap Narrowing in Black TiO₂ Nanoparticles," *J. Am. Chem. Soc.*, vol. 134, no. 18, pp. 7600–7603, 2012.
- [159] J. Tauc, R. Grigorovici, and A. Vancu, "Optical Properties and Electronic Structure of Amorphous Germanium," *Phys. Status Solidi B*, vol. 15, no. 2, pp. 627–637, 2006.
- [160] H. He, K. Yang, N. Wang, F. Luo, and H. Chen, "Hydrogenated TiO₂ Film for Enhancing Photovoltaic Properties of Solar Cells and Self-Sensitized Effect," *J. Appl. Phys.*, vol. 114, no. 21, p. 213505, 2013.
- [161] M. R. Mohammadizadeh, M. Bagheri, S. Aghabagheri, and Y. Abdi, "Photocatalytic Activity of TiO₂ Thin Films by Hydrogen DC Plasma," *Appl. Surf. Sci.*, vol. 350, pp. 43–49, 2015.
- [162] D. C. Cronmeyer, "Infrared Absorption of Reduced Rutile TiO₂ Single Crystals," *Phys. Rev.*, vol. 113, pp. 1222–1226, Mar. 1959.
- [163] S. Ivanov, A. Barylyak, K. Besaha, A. Dimitrova, S. Krischok, A. Bund, and J. Bobitski, "Enhanced Lithium Ion Storage in TiO₂ Nanoparticles, induced by Sulphur and Carbon Co-Doping," *J. Power Sources*, vol. 326, pp. 270–278, 2016.
- [164] G. Wang, H. Wang, Y. Ling, Y. Tang, X. Yang, R. C. Fitzmorris, C. Wang, J. Z. Zhang, and Y. Li, "Hydrogen-Treated TiO₂ Nanowire Arrays for Photoelectrochemical Water Splitting," *Nano Lett.*, vol. 11, pp. 3026–3033, July 2011.
- [165] Y. Yan, M. Han, A. Konkin, T. Koppe, D. Wang, T. Andreu, G. Chen, U. Vetter, J. R. Morante, and P. Schaaf, "Slightly Hydrogenated TiO₂ with Enhanced Photocatalytic Performance," *J. Mater. Chem. A*, vol. 2, no. 32, pp. 12708–12716, 2014.
- [166] G. Panomsuwan, A. Watthanaphanit, T. Ishizaki, and N. Saito, "Water-Plasma-Assisted Synthesis of Black Titania Spheres with Efficient Visible-Light Photocatalytic Activity," *Phys. Chem. Chem. Phys.*, vol. 17, no. 21, pp. 13794–13799, 2015.

- [167] C. Fan, C. Chen, J. Wang, X. Fu, Z. Ren, G. Qian, and Z. Wang, "Black Hydroxylated Titanium Dioxide Prepared via Ultrasonication with Enhanced Photocatalytic Activity," *Sci. Rep.*, vol. 5, p. 11712, 2015.
- [168] E. McCafferty and P. Wightman J., "Determination of the Concentration of Surface Hydroxyl Groups on Metal Oxide Films by a Quantitative XPS Method," *Surf. Interface Anal.*, vol. 26, no. 8, pp. 549–564, 1998.
- [169] F. Amano, M. Nakata, A. Yamamoto, and T. Tanaka, "Effect of Ti^{3+} Ions and Conduction Band Electrons on Photocatalytic and Photoelectrochemical Activity of Rutile Titania for Water Oxidation," *J. Phys. Chem. C*, vol. 120, no. 12, pp. 6467–6474, 2016.
- [170] J.-Y. Eom, S.-J. Lim, S.-M. Lee, W.-H. Ryu, and H.-S. Kwon, "Black Titanium Oxide Nanoarray Electrodes for High Rate Li-ion Microbatteries," *J. Mater. Chem. A*, vol. 3, no. 21, pp. 11183–11188, 2015.
- [171] H. P. Gunnlaugsson, "A Simple Model to Extract Hyperfine Interaction Distributions from Mössbauer Spectra," *Hyperfine Interact.*, vol. 167, pp. 851–854, Jan 2006.
- [172] P. Umek, C. Bittencourt, P. Guttman, A. Gloter, S. D. Škapin, and D. Arčon, " Mn^{2+} Substitutional Doping of TiO_2 Nanoribbons: A Three-Step Approach," *J. Phys. Chem. C*, vol. 118, no. 36, pp. 21250–21257, 2014.
- [173] T. E. Mølholt, R. Mantovan, H. P. Gunnlaugsson, D. Naidoo, S. Ólafsson, K. Bharuth-Ram, M. Fanciulli, K. Johnston, Y. Kobayashi, G. Langouche, H. Masenda, R. Sielemann, G. Weyer, and H. P. Gíslason, "Observation of Spin-Lattice Relaxations of Dilute Fe^{3+} in MgO by Mössbauer Spectroscopy," *Hyperfine Interact.*, vol. 197, pp. 89–94, Apr 2010.
- [174] B. J. Morgan and G. W. Watson, "Intrinsic n-type Defect Formation in TiO_2 : A Comparison of Rutile and Anatase from GGA+U Calculations," *J. Phys. Chem. C*, vol. 114, no. 5, pp. 2321–2328, 2010.
- [175] X. Pan, M.-Q. Yang, X. Fu, N. Zhang, and Y.-J. Xu, "Defective TiO_2 with Oxygen Vacancies: Synthesis, Properties and Photocatalytic Applications," *Nanoscale*, vol. 5, pp. 3601–3614, 2013.
- [176] M. Robinson, N. A. Marks, and G. R. Lumpkin, "Structural Dependence of Threshold Displacement Energies in Rutile, Anatase and Brookite TiO_2 ," *Mater. Chem. Phys.*, vol. 147, no. 1, pp. 311–318, 2014.
- [177] A. Ghicov, J. M. Macak, H. Tsuchiya, J. Kunze, V. Haeublein, L. Frey, and P. Schmuki, "Ion Implantation and Annealing for an Efficient N-Doping of TiO_2 Nanotubes," *Nano Lett.*, vol. 6, no. 5, pp. 1080–1082, 2006.
- [178] F. Dolci, M. D. Chio, M. Baricco, and E. Giamello, "Niobium Pentoxide as Promoter in the Mixed MgH_2/Nb_2O_5 System for Hydrogen Storage: a Multitechnique Investigation of the H_2 Uptake," *J. Mater. Sci.*, vol. 42, pp. 7180–7185, Sep 2007.

- [179] Y. Kobayashi, O. J. Hernandez, T. Sakaguchi, T. Yajima, T. Roisnel, Y. Tsujimoto, M. Morita, Y. Noda, Y. Mogami, A. Kitada, M. Ohkura, S. Hosokawa, Z. Li, K. Hayashi, Y. Kusano, J. e. Kim, N. Tsuji, A. Fujiwara, Y. Matsushita, K. Yoshimura, K. Takegoshi, M. Inoue, M. Takano, and H. Kageyama, "An Oxyhydride of BaTiO₃ Exhibiting Hydride Exchange and Electronic Conductivity," *Nat. Mater.*, vol. 11, pp. 507 EP –, Apr 2012.
- [180] A. J. Hupfer, E. V. Monakhov, B. G. Svensson, I. Chaplygin, and E. V. Lavrov, "Hydrogen Motion in Rutile TiO₂," *Sci. Rep.*, vol. 7, no. 1, p. 17065, 2017.
- [181] S. A. Sheikholeslam, H. Manzano, C. Grecu, and A. Ivanov, "Reduced Hydrogen Diffusion in Strained Amorphous SiO₂: Understanding Ageing in MOSFET Devices," *J. Mater. Chem. C*, vol. 4, pp. 8104–8110, 2016.
- [182] M. I. Nandasiri, V. Shutthanandan, S. Manandhar, A. M. Schwarz, L. Oxenford, J. V. Kennedy, S. Thevuthasan, and M. A. Henderson, "Instability of Hydrogenated TiO₂," *J. Phys. Chem. Lett.*, vol. 6, no. 22, pp. 4627–4632, 2015.
- [183] S. G. Koch, E. V. Lavrov, and J. Weber, "Towards Understanding the Hydrogen Molecule in ZnO," *Phys. Rev. B*, vol. 90, p. 205212, Nov 2014.
- [184] M. A. Henderson, "Mechanism for the Bulk-Assisted Reoxidation of Ion Sputtered TiO₂ Surfaces: Diffusion of Oxygen to the Surface or Titanium to the Bulk?," *Surf. Sci.*, vol. 343, no. 1, pp. L1156 – L1160, 1995.
- [185] C. E. Rodríguez-Torres, A. F. Cabrera, L. A. Errico, C. Adán, F. G. Requejo, M. Weissmann, and S. J. Stewart, "Local Structure and Magnetic Behaviour of Fe-Doped TiO₂ Anatase Nanoparticles: Experiments and Calculations," *J. Phys. Condens. Matter*, vol. 20, no. 13, p. 135210, 2008.
- [186] A. Kordatos, N. Kelaidis, and A. Chroneos, "Migration of Sodium and Lithium Interstitials in Anatase TiO₂," *Solid State Ionics*, vol. 315, pp. 40 – 43, 2018.
- [187] Y. Chen and D. Yang, *Hyperfine Interactions*. Wiley-Blackwell, 2007.
- [188] S. Zhu, W. Liu, S. Wei, C. Fan, and Y. Li, "Local Structure around Iron Ions in Anatase TiO₂," *AIP Conf. Proc.*, vol. 882, no. 1, pp. 253–255, 2007.
- [189] C. G. Van de Walle and J. Neugebauer, "Universal Alignment of Hydrogen Levels in Semiconductors, Insulators and Solutions," *Nature*, vol. 423, no. 6940, pp. 626–628, 2003.
- [190] P. G. Moses, A. Janotti, C. Franchini, G. Kresse, and C. G. Van de Walle, "Donor Defects and Small Polarons on the TiO₂(110) Surface," *J. Appl. Phys.*, vol. 119, no. 18, p. 181503, 2016.
- [191] P. F. Chester and D. H. Bradhurst, "Electrolytically Induced Conductivity in Rutile," *Nature*, vol. 199, no. 4898, pp. 1056–1057, 1963.
- [192] F. Herklotz, E. V. Lavrov, and J. Weber, "Infrared Absorption of the Hydrogen Donor in Rutile TiO₂," *Phys. Rev. B*, vol. 83, p. 235202, Jun 2011.

- [193] S. G. Koch, E. V. Lavrov, and J. Weber, "Photoconductive Detection of Tetrahedrally Coordinated Hydrogen in ZnO," *Phys. Rev. Lett.*, vol. 108, p. 165501, Apr 2012.
- [194] Y. Chen, R. Gonzalez, and K. L. Tsang, "Diffusion of Deuterium and Hydrogen in Rutile TiO₂ Crystals at Low Temperatures," *Phys. Rev. Lett.*, vol. 53, pp. 1077–1079, Sep 1984.
- [195] E. J. Spahr, L. Wen, M. Stavola, L. A. Boatner, L. C. Feldman, N. H. Tolk, and G. Lüpke, "Giant Enhancement of Hydrogen Transport in Rutile TiO₂ at Low Temperatures," *Phys. Rev. Lett.*, vol. 104, p. 205901, May 2010.
- [196] D. Forkel-Wirth, N. Achtziger, A. Burchard, J. Correia, M. Deicher, T. Licht, R. Magerle, J. Marques, J. Meier, W. Pfeiffer, U. Reislöhner, M. Rüb, M. Toulemonde, and W. Witthuhn, "Hydrogen Passivation of Cd Acceptors in III-V Semiconductors Studied by PAC Spectroscopy," *Solid State Commun.*, vol. 93, no. 5, pp. 425 – 430, 1995.
- [197] R. Fromknecht, I. Khubeis, S. Massing, and O. Meyer, "Ion Implantation in TiO₂: Damage Production and Recovery, Lattice Site Location and Electrical Conductivity," *Nucl. Instrum. Methods Phys. Res., Sect. B*, vol. 147, no. 1, pp. 191 – 201, 1999.
- [198] D. V. Zyabkin, J. Schell, D. Gaertner, T. T. Dang, J. N. Gonçalves, G. Marschick, and P. Schaaf, "Hyperfine Interactions and Diffusion of Cd in TiO₂ (Rutile)," *J. Appl. Phys.*, vol. 126, no. 1, p. 015102, 2019.
- [199] J. Schell, D. Zyabkin, D. C. Lupascu, H.-C. Hofsäss, M. O. Karabasov, A. Welker, and P. Schaaf, "A Hyperfine Look at Titanium Dioxide," *AIP Adv.*, vol. 9, no. 8, p. 085208, 2019.
- [200] D. G. Thomas and J. J. Lander, "Hydrogen as a Donor in Zinc Oxide," *J. Chem. Phys.*, vol. 25, no. 6, pp. 1136–1142, 1956.
- [201] A. Baurichter, M. Deicher, S. Deubler, D. Forkel, J. Meier, H. Wolf, and W. Witthuhn, "Microscopical Studies at Cadmium Impurities in Compound Semiconductors," *Appl. Surf. Sci.*, vol. 50, no. 1, pp. 165 – 168, 1991.
- [202] D. Gaspar, L. Pereira, K. Gehrke, B. Galler, E. Fortunato, and R. Martins, "High Mobility Hydrogenated Zinc Oxide thin Films," *Sol. Energy Mater. Sol. Cells*, vol. 163, pp. 255 – 262, 2017.
- [203] T. R. Mattsson, S. Root, A. E. Mattsson, L. Shulenburger, R. J. Magyar, and D. G. Flicker, "Validating Density-Functional Theory Simulations at High Energy-Density Conditions with Liquid Krypton Shock Experiments to 850 GPa on Sandia's Z Machine," *Phys. Rev. B*, vol. 90, p. 184105, Nov 2014.
- [204] R. Mantovan, H. P. Gunnlaugsson, K. Johnston, H. Masenda, T. E. Mølholt, D. Naidoo, M. Ncube, S. Shayestehaminzadeh, K. Bharuth-Ram, M. Fanciulli, H. P. Gislason, G. Langouche, S. Ólafsson, L. M. C. Pereira, U. Wahl, P. Torelli, and G. Weyer, "Atomic-Scale Magnetic Properties of Truly 3d-Diluted ZnO," *Adv. Electron. Mater.*, vol. 1, no. 1-2, p. 1400039, 2015.

- [205] H. Skudlik, M. Deicher, R. Keller, R. Magerle, W. Pfeiffer, D. Steiner, E. Recknagel, and T. Wichert, "Influence of Electronic Parameters on the Electric-field Gradients Induced by H at the Probe Atom $^{111}\text{In}/^{111}\text{Cd}$ in Si," *Phys. Rev. B*, vol. 46, pp. 2159–2171, Jul 1992.
- [206] R. Palmer, T. Doan, P. Lloyd, B. Jarvis, and N. Ahmed, "Reduction of TiO_2 with Hydrogen Plasma," *Plasma Chem. Plasma Process.*, vol. 22, pp. 335–350, Sep 2002.
- [207] P. P. Stampel, J. C. Travis, and M. J. Bielefeld, "Mössbauer Spectroscopic Studies of Iron-Doped Rutile," *Phys. Status Solidi A*, vol. 15, no. 1, pp. 181–189, 1973.
- [208] K. Liu, A. I. Rykov, J. Wang, and T. Zhang, "Chapter One - Recent Advances in the Application of Mössbauer Spectroscopy in Heterogeneous Catalysis," vol. 58 of *Advances in Catalysis*, pp. 1 – 142, Academic Press, 2015.
- [209] J. M. D. Coey, P. Stamenov, R. D. Gunning, M. Venkatesan, and K. Paul, "Ferromagnetism in Defect-ridden Oxides and Related Materials," *New J. Phys.*, vol. 12, p. 053025, may 2010.
- [210] U. D. Wdowik and K. Ruebenbauer, "Emission Mössbauer Spectroscopy in TiO_2 Single Crystal," *Phys. Rev. B*, vol. 63, p. 125101, Mar 2001.
- [211] H. M. Lee and C. S. Kim, "Effects of Oxygen Vacancies on the Ferromagnetism in Fe-Doped Anatase TiO_2 ," *J. Magn. Magn. Mater.*, vol. 310, no. 2, Part 3, pp. 2099 – 2101, 2007.
Proceedings of the 17th International Conference on Magnetism.
- [212] Y. R. Uhm, S. Woo, M. K. Lee, and C. K. Rhee, "The Magnetic and Photo-Catalytic Properties of Fe Doped TiO_2 Nanocrystalline Powder Synthesized by Mechanical Alloying," in *Progress in Powder Metallurgy*, vol. 534 of *Materials Science Forum*, pp. 229–232, Trans Tech Publications Ltd, 1 2007.
- [213] R. Petrucci, F. Herring, J. Madura, and C. Bissonnette, *General Chemistry: Principles and Modern Applications*.
Pearson Education, 2017.
- [214] D. L. Nagy, "Trends in Mössbauer Emission Spectroscopy of $^{57}\text{Co}/^{57}\text{Fe}$," *Hyperfine Interact.*, vol. 83, pp. 1–19, Dec 1994.
- [215] G. Weyer, "Mössbauer Spectroscopy at ISOLDE," *Hyperfine Interact.*, vol. 129, pp. 371–390, Dec 2000.
- [216] R. Mantovan, R. Fallica, A. Mokhles Gerami, T. E. Mølholt, C. Wiemer, M. Longo, H. P. Gunnlaugsson, K. Johnston, H. Masenda, D. Naidoo, M. Ncube, K. Bharuth-Ram, M. Fanciulli, H. P. Gislason, G. Langouche, S. Ólafsson, and G. Weyer, "Atomic-Scale Study of the Amorphous-to-Crystalline Phase Transition Mechanism in GeTe Thin Films," *Sci. Rep.*, vol. 7, no. 1, p. 8234, 2017.

- [217] B. Qi, H. Gunnlaugsson, A. M. Gerami, H. Gislason, S. Ólafsson, F. Magnus, T. Mølholt, H. Masenda, A. T. Martín-Lueugo, A. Bonanni, P. Krastev, V. Masondo, I. Unzueta, K. Bharuth-Ram, K. Johnston, D. Naidoo, J. Schell, and P. Schaaf, “ ^{57}Fe Mössbauer Study of Epitaxial TiN thin Film Grown on MgO(100) by Magnetron Sputtering,” *Appl. Surf. Sci.*, vol. 464, pp. 682 – 691, 2019.
- [218] S. Prussin, D. I. Margolese, and R. N. Tauber, “Formation of Amorphous Layers by Ion Implantation,” *J. Appl. Phys.*, vol. 57, no. 2, pp. 180–185, 1985.
- [219] G. Weyer, H. Gunnlaugsson, M. Dietrich, M. Fanciulli, K. Bharuth-Ram, and R. Sielemann, “Creation and Annealing of Defect Structures in Silicon-based Semiconductors during and after Implantations at 77–500 K,” *Nucl. Instrum. Methods Phys. Res., Sect. B*, vol. 206, pp. 90 – 94, 2003.
- [220] J. Pechousek, R. Prochazka, J. D., and M. M., “Fully LabVIEW-Powered Mössbauer Spectrometer,” *iJOE*, vol. 5, pp. 61–64, Aug 2009.
- [221] T. Mitsui, “Synchrotron mössbauer Spectroscopy Measurement,” in *Magnets Under Pressure* (Y. Kono and C. Sanloup, eds.), ch. 7, pp. 179 – 210, Elsevier, 2018.
- [222] G. Weyer, *Applications of Parallel-Plate Avalanche Counters in Mössbauer Spectroscopy*, ch. 3, pp. 301–319.
Boston, MA: Springer US, 1976.
- [223] A. H. Mkrtchyan, R. P. Vardapetyan, E. M. Harutyunyan, and A. V. Khachatryan, “Influence of Laser Radiation on the Mössbauer Absorption Spectra of CdS (Fe^{57}) Single Crystal,” *J. Contemp. Phys.*, vol. 44, pp. 191–193, Aug 2009.
- [224] J. Pechousek, M. Mashlan, J. Frydrych, D. Jancik, and R. Prochazka, “Improving Detector Signal Processing with Pulse Height Analysis in Mössbauer Spectrometers,” *Hyperfine Interact.*, vol. 175, pp. 1–8, Feb 2007.